CARDIFF UNIVERSITY
PRIFYSGOL CAERDYDD

Hydrogenation of ketones over platinum group metals: a DFT study

Edward Jeffery

PhD Thesis, July 2007

ProQuest LLC
789 East Eisenhower Parkway
P.O. Box 1346
Ann Arbor, MI 48106-1346

The most exciting phrase to hear in science, the one that heralds new discoveries, is not 'Eureka!' but 'That's funny ....'

Isaac Asimov

Acknowledgments

Firstly, I would like to thank my supervisor, Dr. David J. Willock for the help and support he has given me over the course of my PhD. He has helped me immensely both in terms of the research culminating in this thesis and during my development as a scientist. I would also like to thank Prof. Graham J. Hutchings and his research group for their input into the experimental side of this project.

I must, of course, thank all the past and present members of the Theoretical Chemistry group at Cardiff University; Prof Peter J. Knowles, Dr. Jamie A. Platts and Dr. Massimo Mella and everybody from Lab 1.95. This includes the present team (Dr. J. Grant Hill, James, Steve, Mike and Kara) and everyone who has passed through during my time here (Gareth, Rudy, Arturo, Bob, Farah, Rajinder, Olivier, Jon, Efi and Jo).

I must also thank all the great people I have met in Cardiff during my time there; Peter, Mike, Huw, Alison, Sarah and Matt as well as my friends from 'back home'; I hope we can keep in touch in the future.

It would be remiss of me not to thank my parents for all they have given me over the past years; it is true to say I would not be writing this without them. The same must be said of my brother, Robert, and my grandparents.

Finally, on a technical note, I would like to thank the EPSRC for the funding to complete this project, the Materials Chemistry Consortium for access to the HPCx supercomputer and the Helix committee at Cardiff University for supplying local computer resources.

DECLARATION

This work has not previously been accepted in substance for any degree and is not being concurrently submitted in candidature for any degree.

Signed 

Date 15/12/2007

STATEMENT 1

This thesis is the result of my own investigations, except where otherwise stated. Other sources are acknowledged by footnotes giving explicit references. A bibliography is appended.

Signed 

Date 15/12/2007

STATEMENT 2

I hereby give consent for my thesis, if accepted, to be made available for photocopying and for inter-library loan, and for the title and summary to be made available to outside organisations.

Signed 

Date 15/12/2007

Contents

List of papers

Publications arising from this work:

1. "A density functional theory study of the adsorption of acetone to the (111) surface of Pt: implications for hydrogenation catalysis"
   E.L. Jeffery, R.K. Mann, G.J. Hutchings, S.H. Taylor, D.J. Willock
   Catalysis Today, 105, 85-92 (2005)

2. "Enantioselective hydrogenation of N-acetyl dehydrophenylalanine methyl ester using cinchonine-modified Pd/Al_2O_3 catalysts"
   N.J. Coulston, E.L. Jeffery, R.P.K. Wells, P. McMorn, P.B. Wells, D.J. Willock, G.J. Hutchings
   J. Catal., 243, 360-367 (2006)

Summary

The enantioselective hydrogenation of α-ketoesters over a platinum surface modified by cinchona alkaloids has been studied using accurate computational modelling.

A series of small prototype compounds were used to interact with the metal surface, leading to the study of acetone adsorption on a platinum surface. It was found that the enol and enolate isomers of acetone may play a crucial role in the surface chemistry. The enol form of acetone was significantly more stable than the keto-form, and the enolate form was also more stable. Vibrational frequency analysis suggests that the enolate form may prove to be a better fit to some of the experimental data than the commonly-accepted ketone form.

The interaction of an α-ketoester, methyl pyruvate, with a platinum surface was then studied using the same techniques. The enol form was again the most stable surface species compared to the enolate and ketone forms. Additionally, the *cis* form of methyl pyruvate was generally more stable than the *trans* form. A full vibrational analysis was performed, allowing comparison with future experimental work.

In order to investigate the conversion between the different types of isomer, an eigenvector following scheme is under development to find reaction barriers and transition states. To date, this has been applied to simpler systems with success and is in the process of being extended to more complicated applications.

Concurrently, a technique to study the whole enantioselective reaction system was also being developed. This involves a modified simple QM/MM scheme containing a model for the surface, the substrate and modifier. This was successfully applied to a simple system (methyl pyruvate interacting with the surface and modifier) and yielded predicted ees in agreement with experimental observation. This was extended to a more complex system under study at Cardiff University and reproduced the experimental enantioselectivity; this was then used to suggest possible improvements to enhance the ee of this system.

1. Introduction

The work presented in this thesis is focused on the theoretical investigation of the hydrogenation of ketones and their related derivatives in an enantioselective manner. In section 1.1 some general background will be provided, which will be followed by a description of the aims of this thesis and a summary of the layout of the work within it.

1.1 Enantioselective hydrogenation catalysis

The enantioselective hydrogenation of an α-ketoester was first widely reported in 1979 by the Orito group, who used a platinum metal surface modified with a cinchona-alkaloid catalyst. The choice of cinchona catalyst, a family of related compounds which are isolated from tree bark and hence available plentifully and cheaply, proved crucial. In the original reaction, methyl pyruvate (a common α-ketoester) was hydrogenated to methyl lactate to produce an *R*-isomer using the alkaloid cinchonidine and the *S*-isomer when using cinchonine (which is an enantiomer of cinchonidine). A generic reaction scheme for this type of process is given in Scheme 1.1.

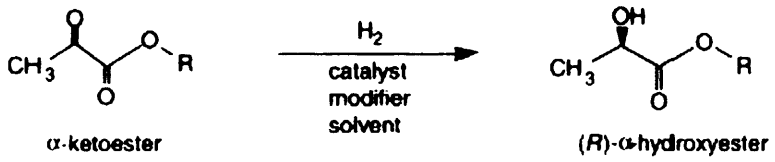

Scheme 1.1: The enantioselective hydrogenation of an α-ketoester using a modified metal surface.

Since this early work, a great deal of research has been focussed on the development and refining of this reaction, and selectivities in excess of 97% ee have been achieved. The high enantioselectivities which are obtainable, combined with the heterogeneous nature of this reaction, have made it a prime target for research groups worldwide.

Platinum catalysts have consistently proved the most reliable, with supports such as SiO_2, TiO_2 and Al_2O_3 commonly used. Acetic acid is a common choice of solvent, but alcohols and non-polar solvents (e.g. toluene) can also be used [1,2]. The di-hydro derivates of the cinchona-alkaloids described above have also been used successfully. The reaction rate of hydrogenation is promoted by between approximately 10-100 times compared to the uncatalysed reaction, allowing high substrate:modifier ratios to be used [3,4].

The mechanism by which this superb stereoselectivity can be achieved is not yet fully understood. Several models have been developed over the years, which are summarised below:

i) First proposed by Wells, the modifier adsorbs onto the surface, and the substrate forms a 1:1 complex with it (typically through a hydrogen bond involving either a protonated modifier nitrogen atom and the keto-moiety of the substrate or half-hydrogenation of the keto-moiety). Stereoselectivity is achieved depending on the stability of these complexes [5,6].

ii) The modifier quinuclidene nitrogen atom attacks the substrate ketone moiety to produce a zwitterion on the surface [7].

iii) Developed by Margitfalvi, the substrate and modifier form a complex in solution, which adsorbs on the surface to undergo hydrogenation [8,9].

The precise nature of the mechanism is not yet understood, although mechanism i) is the most widely accepted model at the moment and is supported by experimental evidence. Further detail is provided in Chapter 2.

1.2 Aim and scope of this thesis

It is the goal of this thesis to be able to shed some light on the mechanism of hydrogenation described in section 1.1. Although this system is widely studied experimentally, only comparatively recently has theoretical chemistry been applied to this field. This may be partially due to the complex nature of the problem at hand. There has yet to be a method developed which can reliably handle the whole reaction system, as it contains a large organic molecule (modifier), a smaller reactant molecule (substrate) and a metal surface/support. Considering the reaction system as a whole, three key interactions can be identified:

i) Interaction between modifier and metal surface

ii) Interaction between modifier and substrate

iii) Interaction between substrate and metal surface

Further details for each of these problems are expanded on in Chapter 2, but to summarise: i) has been deduced experimentally, ii) has yet to be confirmed but a good understanding has been obtained experimentally and iii) has only a small amount of information inferred from surface science. Therefore, the bulk of this thesis will be focused on the substrate-metal interaction.

The interaction of a relatively large α-ketoester such as methyl pyruvate is at the larger boundary of what can be reliably handled using the techniques applied here (periodic planewave DFT). Therefore, a series of smaller model compounds will be studied initially; acetone is perfectly suited to this purpose. The study of acetone also raises the issue of keto-enol-enolate isomerisation. This is also present in the larger ketoester, so must be fully considered. Therefore, the question of the identity of the species on the surface which is hydrogenated is ambiguous: is

it in keto-, enol- or enolate ion-form? A mixture of C=C and C=O bonds may be present in the surface species, leading to several possible adsorption modes. It is therefore also necessary to look at simple systems containing C=O and C=C bonds and assess their surface stability, geometry and potential effect on the reaction system; carbon monoxide, ethene and formaldehyde will be studied for this purpose. The adsorption of hydrogen will also be studied, both as an initial test-case for the methodology to be used and as a part of the hydrogenation reaction scheme.

Once this has been completed, the study of the α-ketoester is addressed. Additionally, some research has been undertaken regarding the study of simple reaction processes. Given the potential presence of different isomers on the surface, and the potential for interconversion between them, a methodology to be able to assess the transition state and reaction barriers within these systems has been developed. This is applied to several simple cases. To finish up the project, some thought has been given to developing a methodology to be able to study the entire reaction scheme quickly and with a high degree of reliability using a QM/MM approach.

1.3 Outline of this thesis

This section will briefly summarise the layout of this thesis.

The next chapter, Chapter 2, will discuss the current state of the literature regarding the topics under investigation in this thesis. This will begin with the past work undertaken in the investigation of the adsorption of the various prototypical molecules to be studied (i.e. hydrogen adsorption, CO, ethene, formaldehyde and acetone). Discussion of the enantioselective hydrogenation reaction will then be given in more detail, including the interaction of the α-ketoester with the metal surface.

Chapter 3 will summarise the necessary theoretical background to the project. The theory behind the differing types of calculation will be presented. This is only intended to be a brief summary of the theory as applied to the work in hand.

Chapter 4 will present the methodology of the work contained in this thesis. This will describe how the theory in Chapter 3 will be applied, with particular attention to how the parameters used in the calculations were arrived at.

Chapter 5 will contain the first of the results sections. This will contain details of calculations carried out on the prototypical molecules which are used here. This includes: hydrogen atom adsorption (both onto and within a metal surface); the adsorption of CO, the adsorption of ethene (both onto flat metal surfaces and the difference observed at step edges); the adsorption of formaldehyde and the adsorption of ethene. The implications of each of these sections for the overall reaction scheme is discussed. Where necessary, additional calculations have been carried out, including vibrational frequency and density of states (DOS) analysis.

Chapter 6 will draw on the lessons learnt in Chapter 5 to study the adsorption of methyl pyruvate on a platinum metal surface. This includes discussion on gas-phase stability and keto-

enol-enolate isomerisation, as well as *cis-trans* isomerisation. The results are supported by vibrational frequency analysis.

Chapter 7 presents the methodology used to find transition states and reaction barriers. This is applied to simple systems, such as hydrogen atoms on a metal surface and formaldehyde interconversion. Some applications for acetone isomerisation are briefly discussed.

Chapter 8 contains the methodology developed for the study of the whole reaction scheme at once. This is fundamentally different to the methodology used up to this point, and involves the use of a modified QM/MM scheme. To this end, a test-case with a known result (the hydrogenation of methyl pyruvate) is extensively discussed. The methodology is then applied to an unknown system, studied only experimentally, and the results interpreted to explain the experimental findings.

Chapter 9 contains the general conclusions for this thesis, and will attempt to link together the work contained in Chapters 5 to 8 and discuss it in terms of the enantioselective hydrogenation scheme.

1.4 References

(1) Ferri, D.; Bürgi, T.; Baiker, A. *J. Chem. Soc. Perkin Trans.* **2000**, *2*, 221.
(2) Baiker, A. *J. Mol. Cat. A* **2000**, *163*, 205.
(3) Schürch, M.; Künzle, N.; Mallat, T.; Baiker, A. *J. Catal.* **1998**, *176*, 569.
(4) Garland, M.; Blaser, H.-U. *J. Am. Chem. Soc.* **1990**, *112*, 7048.
(5) Webb, G.; Wells, P. B. *Catal. Today* **1992**, *12*, 319.
(6) Sutherland, I. M.; Ibbotson, A.; Moyes, R. B.; Wells, P. B. *J. Catal.* **1990**, *125*, 77.
(7) Augustine, R. L.; Tanielyan, S. K.; Doyle, L. K. *Tetrahedron: Asymm.* **1993**, *4*, 1803.
(8) Margitfalvi, J. L.; Hegedus, M.; Tfirst, E. *Stud. Surf. Sci. Catal.* **1996**, *101*, 241.
(9) Margitfalvi, J. L.; Tfirst, E. *J. Mol. Cat. A* **1999**, *139*, 81.

2. Literature Review

As discussed in the previous chapter, the main direction of this work will be split into two parts: the adsorption of small molecules onto Group 10 metal surfaces and their use as a model for larger systems, and the direct simulation of these larger systems. Therefore, this review will also be divided along the same lines. Due to the expensive nature of modelling whole catalytic systems (such as those used for enantioselective hydrogenation catalysis), they are often broken down into smaller, more manageable, processes. The experimental and theoretical work to date will be scrutinised, starting at the smallest part of the catalytic system (hydrogen) and building up to the first acceptable prototype reactant (acetone). The second part of this review will focus on the reaction as a whole, including experimental and theoretical work on the overall reaction process, as well as the role and structure of the reactant itself and the catalytic modifier.

2.1 Adsorption of small molecules to Group 10 metal surfaces

2.1.1 Adsorption of hydrogen onto Group 10 metal surfaces

The adsorption of hydrogen onto metal surfaces has been a cornerstone of the implementation and testing of many experimental and theoretical systems for many years. Hydrogen will adsorb dissociatively on almost all transition metal surfaces, with an adsorption energy of approximately 25-60 kJ mol^{-1} (for $\frac{1}{2}H_2$). Although adsorption of hydrogen below the surface of the metal has been observed, first we shall consider the adsorption of the hydrogen atom on top of the metal surface. Possible adsorption sites for a hydrogen atom on a (111) metal surface are depicted in Figure 2.1.

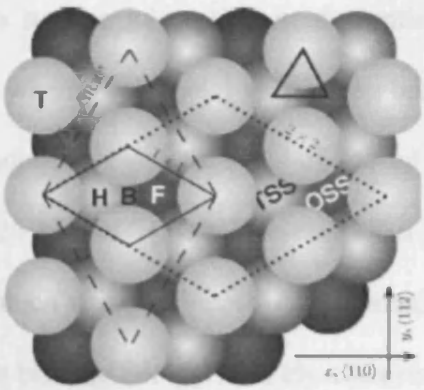

Figure 2.1: Possible adsorption sites for hydrogen above and within a metal (111) surface (2x2 surface cell represented by dotted line). Sites depicted are T (top site), B (bridge), F (fcc hollow), H (hcp hollow), TSS (tetrahedral subsurface hole) and OSS (octahedral subsurface hole). From reference [1]

The adsorption site, energetic preference and band structure of hydrogen adsorbed onto Group 10 metal surfaces has been well characterised both experimentally and theoretically. Early experimental evidence for the adsorption of H on Ni (111), using low temperature (173 K) Low Energy Electron Diffraction (LEED) analysis matching observed patterns with theoretical LEED patterns, suggested a slight preference for a hollow site, with the bridge and top positions disfavoured [2]. Angle resolved photoemission spectroscopy (PES) concluded that this bonding was primarily *via* s and p orbitals of the metal surface, with no localised H-induced state observed [3]. This system has also been extensively studied using theoretical methods and was often used in the development and testing of such methods. For example, the Ni/H system was studied using the effective medium method [4], in which an atom is embedded in an inhomogeneous host which is then replaced with an effective homogeneous medium. The threefold-hollow adsorption site was found to be the most stable, with a binding energy of 260 kJ mol^{-1} (5 kJ mol^{-1} more than the bridge site and 15 kJ mol^{-1} more than the top site), and subsurface adsorption was found to be possible with

a binding energy of 240 kJ mol^{-1}. It was suggested that at low temperatures subsurface adsorption can occur, which can transfer to surface adsorption or desorption as the system is heated. The embedded atom method (EAM), where each metal atom is embedded into the electron gas of the other atoms, was used to find binding energies for Ni/H of 247 kJ mol^{-1} (hollow) and 213 kJ mol^{-1} (top), with an estimated error of 24 kJ mol^{-1} [5]. More recently, a 3-layer 41-atom embedded metal cluster was used with a CI approach using effective core potentials [6] to study the dissociative adsorption of H_2 on Ni (111). The binding energy of H chemisorbed at a threefold site was found to be 260 kJ mol^{-1}, with the bridge and top sites 11 kJ mol^{-1} and 34 kJ mol^{-1} lower (the H-Ni distance was found to be 1.86 Å, with a vibrational frequency of 1176 cm^{-1}).

The adsorption site preference, bond lengths and band structure have therefore been determined, and more recent work has concentrated on refinement of these results, often using pDFT methods. For example, the adsorption energies and DOS for Ni(111)/H was calculated using the full-potential linearised augmented planewave method (FP-LAPW) (within the GGA) [7]. At 1ML coverage the binding energies were found to be: fcc hollow (279 kJ mol^{-1}), hcp hollow (277 kJ mol^{-1}), bridge (252 kJ mol^{-1}), top (198 kJ mol^{-1}) and subsurface (233 kJ mol^{-1}), with the bond lengths varying between 1.49 and 1.84 Å. The calculated DOS is depicted in Figure 2.2, showing the band formed on hydrogen chemisorption approximately 4.5-9.0 eV below the Fermi level. The conclusion therefore is that the 4(s+p) orbitals (dotted line) are more important than the 3d (solid line), and that the orbital contribution mostly comes from the surface layer.

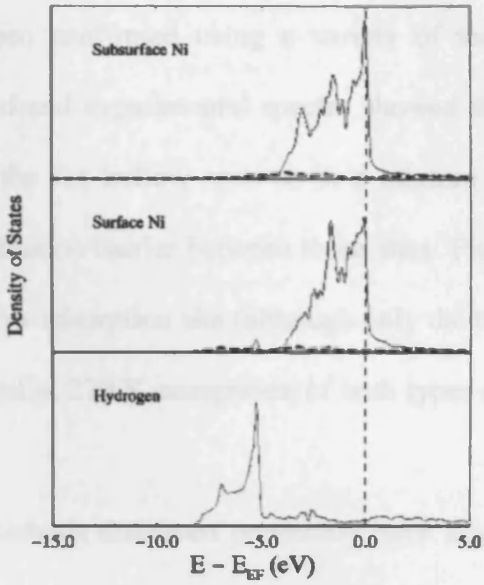

Figure 2.2: Calculated DOS for 0.5ML hydrogen adsorbed on the Ni (111) surface at the threefold hollow site. From reference [7].

A comprehensive study, using the VASP code with a 4-layer metal slab and PAW pseudopotentials, compared the adsorption energies when the system was treated using both spin-polarised and non-spin-polarised methods [8]. The conclusion was that, in order to obtain highly accurate energies, spin-polarisation is in fact necessary. However, if a non-spin-polarised calculation is used, the calculated geometries and ordering of adsorption energies are reasonably accurate (less than 10 kJ mol^{-1} difference between the polarized and non-spin polarized case; however relative energies are typically less than 1 kJ mol^{-1} different). The conclusion from all these studies is that the adsorption of hydrogen onto a Ni(111) surface will preferentially occur in a hollow site, with the bridge site less favourable and the top site substantially less stable. Although the accuracy of these calculations has improved as the methodology has developed, the relative ordering of these energies has changed little from early theoretical calculations.

Adsorption of hydrogen onto the Pd(111) surface is known to follow the same pattern that is observed for Ni. This has been confirmed using a variety of techniques, such as LEED [9]. Comparison between calculated and experimental spectra showed that at low temperature (82 K) hydrogen is located either in the fcc hollow sites or in a mixture of fcc hollow and octahedral subsurface sites, with a low diffusion barrier between these sites. Fitting of helium-diffraction data [10] suggested a threefold hollow adsorption site (although only the top layer of atoms was studied) at low temperatures (140 K) and at 270 K occupation of both types of hollow sites is suggested to occur.

The early theoretical methods discussed previously have also been applied to this system. The experimental results were reproduced using both the EAM [5] (adsorption energy of hollow 281 kJ mol^{-1}, top 157 kJ mol^{-1}, bridge unstable) and embedded clusters [11] (which specifically suggested a preference for fcc over hcp by 9 kJ mol^{-1}). Subsurface adsorption was considered using the EAM [12], which suggested that at low coverages subsurface occupation of the octahedral interstitial site was favoured, with surface hollow adsorption being observed as coverage approached 1 ML. Interestingly, hydrogen atoms located in adjacent sites (e.g. surface and corresponding subsurface sites) repel each other by up to 20 kJ mol^{-1}.

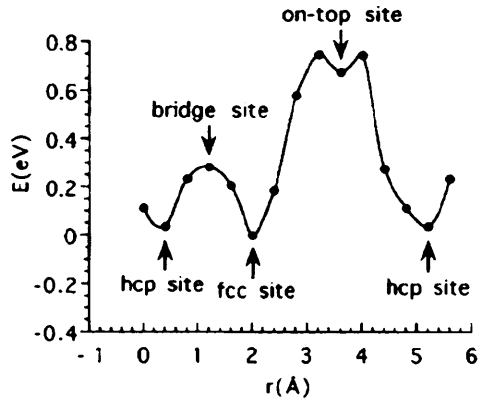

Figure 2.3: Potential energy profile for H on Pd (111) (1/4 ML coverage). From reference [13].

The VAMP program (periodic DFT with ultrasoft pseudopotentials) was used for a comprehensive study of H on Pd (111) using the LDA and the Ceperley and Alder exchange-correlation functional [13]. The calculated adsorption energies were: 66 kJ mol^{-1} (fcc); 63 kJ mol^{-1} (hcp); 39 kJ mol^{-1} (bridge); 1 kJ mol^{-1} (top) at ¼ ML coverage (Fig. 2.3). The DOS of H adsorbed in different sites and band structure were also calculated. This pattern of adsorption energies has been verified in further studies using the VASP [14] and ADF [1] codes.

The adsorption of hydrogen onto the (111) surface of platinum is perhaps the least studied of the systems discussed here. Experimentally, the preferential adsorption site was found to be a fcc hollow site, as determined by Low-Energy Recoil Scattering [15] (H-Pt distance 1.78Å). This was confirmed more recently by the use of Low-Energy Ion Channelling [16]. Theoretically, reliable results regarding this system were not reported until relatively recently. For example, use of the DACAPO code with ultrasoft pseudopotentials on a 3-layer surface slab [17] predicted adsorption energies of 74 kJ mol^{-1} (atop), 69 kJ mol^{-1} (bridge), 72 kJ mol^{-1} (hcp) and 82 kJ mol^{-1} (fcc). This was confirmed used the VASP code [14,18]; the role of subsurface hydrogen was considered recently [19], with the conclusion that this will occur above 1ML coverage, with combined fcc/tetrahedral systems showing a stabilization.

2.1.2 The role of subsurface hydrogen

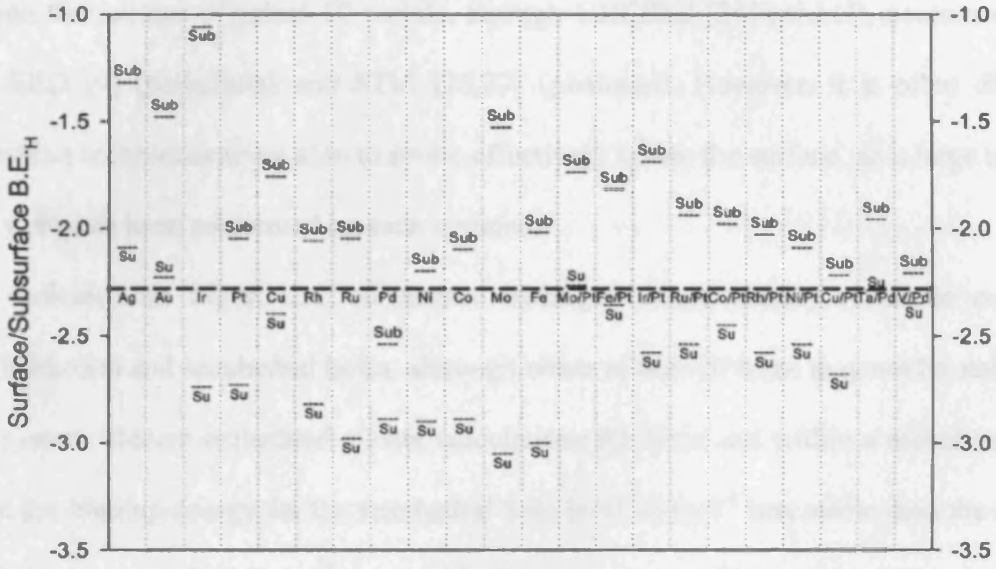

Figure 2.4: Surface and subsurface binding energies for hydrogen on metal surfaces, calculated using periodic DFT. Dotted line is thermoneutral dissociative adsorption/desorption of H_2. From reference [20].

The adsorption of hydrogen below the surface of a metal has been widely known for a considerable length of time, and the presence of such hydrogen atoms has been implicated in a number of catalytic reactions, particularly for palladium metal systems [21]; the anomaly of Pd having a more stable subsurface site than other metals is evinced in Figure 2.4. Subsurface hydrogen atoms are known to be more reactive, and possess significantly higher potential energy, than their surface-bound counterparts. The comparison between subsurface and surface binding energies, calculated using periodic DFT, is shown in Figure 2.4 for a variety of transition metals and transition metal alloys. As well as a possible source of hydrogen, these facts may open up new pathways to reaction for H atoms. The use of subsurface hydrogen has been suggested for a number of catalytic hydrogenation processes, including ethylene hydrogenation [22] (surface H atoms are

unreactive) and acetylene hydrogenation [23] (different products are formed by surface and subsurface-sourced H atoms). Experimentally, there is evidence for the existence of hydrogen adsorbed into the surface of group 10 metals, through HREELS [24] (nickel), neutron diffraction [25] and LEED [9] (palladium) and STM [26,27] (platinum). However, it is often difficult for surface-sensitive techniques to be able to probe effectively below the surface, so a large quantity of theoretical work has been performed on such systems.

As indicated on Figure 2.1, subsurface hydrogen atoms usually reside in one of two positions; octahedral and tetrahedral holes, although either or both of these may not be stable for any given MH system. Recent embedded cluster calculations for H on and within a nickel surface [28] suggest that the binding energy for the tetrahedral hole is 41 kJ mol^{-1} less stable than the octahedral hole, which in turn was 39 kJ mol^{-1} less stable than the most stable surface adsorption site. The barrier for a H atom moving from a surface hollow to subsurface hole adsorption site was approximately 21 kJ mol^{-1} and diffusion between different subsurface hole types had a barrier of about 46 kJ mol^{-1}. More recent accurate VASP periodic DFT calculations (using the nudged elastic band method) [29] obtained an adsorption energy of -5 kJ mol^{-1} for the octahedral site. Despite this, it was hypothesized that this is a viable source of hydrogen for hydrogenation catalysis; first hydrogen must cross an energy barrier to emerge onto the surface, and this extra potential energy makes it behave as a 'hot reactant.' A recent comprehensive study using the DACAPO code [30] calculated binding energies of 210 kJ mol^{-1} (octahedral) and 198 kJ mol^{-1} (tetrahedral), compared to the best surface adsorption site of 280 kJ mol^{-1} (fcc hollow). Subsurface adsorption resulted in an expansion of spacing between the first two rows of metal atoms by 0.05Å. The barrier to diffusion between surface fcc site and the octahedral site was estimated at 85 kJ mol^{-1}.

Similar results are obtained for subsurface adsorption into palladium metal surfaces. For example, using the EAM [12], adsorption into a subsurface octahedral site has an energy of 257 kJ mol^{-1}, compared to 254 kJ mol^{-1} for the subsurface tetrahedral site. It was suggested that at low coverage (e.g. about 1/3 ML) subsurface octahedral occupation was preferred, with surface hollow and subsurface octahedral both occupied as coverage approaches 1 ML. The preference for octahedral rather than tetrahedral adsorption was also noted using the effective medium method [31]. More recently, using the CPMD code for a four Pd-atom cubic supercell [32], tetrahedral occupation is preferred over octahedral unless zero point energies (ZPE) are included, at which point octahedral occupation becomes predominant. The conclusion for all of these studies is that, in particular for palladium, subsurface occupation is both theoretically viable and noted through experiment; octahedral adsorption is always also preferred over tetrahedral, which is logical given the greater space available to the adsorbate in the octahedral site.

2.1.3 Adsorption of CO onto Group 10 metal surfaces

Unlike the example of hydrogen adsorption on group 10 metal surfaces, the fate of CO adsorbed onto metal surfaces is a lot less clear-cut and is still the subject of much research. The same potential surface adsorption sites are possible for CO as depicted for hydrogen in Fig. 2.1. Considering the case of CO on Ni (111), early spectroscopic studies predicted a bridging site to be the most favourable [33-35]. However, more recent work has suggested that adsorption occurs into hollow sites, for example using photoelectron diffraction [36] and LEED [37]. A more recent photoelectron diffraction study suggested a slight preference for adsorption into the hcp over the fcc hollow site, although the difference was not significant [38]. The variation in binding site with

surface coverage has also been studied using photoelectron spectroscopy [39]. At up to 0.5 ML surface coverage, 3-fold hollow sites are preferred; between 0.50-0.61 ML a mixture of atop and bridge sites (about 1:3 ratio) are observed; above 0.62 ML a complicated mixture of all binding sites is observed. The correct binding site for low coverage has also been predicted theoretically using a RPBE GGA formulation [40].

The Pd (111)/CO system is the least studied of the group 10 metal systems. Experimentally, inverse photoemission spectroscopy [41], infrared spectroscopy [42] and LEED studies [43] have provided little conclusive evidence for preferred binding sites or energies. A combined STM and total energy (extended Hückel theory) study suggested either top-hollow or hcp-fcc pairs of adsorption sites for CO [44]. The theoretical calculations confirmed this, and indicated that the hollow sites are the most favourable, with a minimal energy difference between them.

The Pt (111)/CO system has been extensively studied both experimentally and theoretically due to the potential relevance to, amongst other uses, automotive catalytic converters. A large volume of experimental work using techniques such as LEED [45], HREELS [46] and STM [47,48] all suggest adsorption should preferentially occur into an atop adsorption site. However, prior to 2001, most DFT calculations predicted a hollow-site should be the most favourable adsorption site (for example, a pDFT study using a 3-layer Pt slab [49] although the difference between adsorption sites was typically less than 10 kJ mol^{-1}). Some calculations, for example DFT using the B3LYP functional with ECPs for a small cluster (10 atoms), did suggest a small preference for the correct binding site (an adsorption energy of 209 kJ mol^{-1} for the top site) [50]. However, in a comprehensive review paper, Feibelman [51] suggested that DFT overestimates the stability of high-coordination binding sites.

Building on this, a number of studies have attempted to determine why this occurs and how to correct it. Grinberg [52] suggested that the discrepancy was caused by the GGA underestimating the loss in C=O bond energy moved from a top to hollow site. Gil [53] investigated the system using both periodic and cluster calculations with a variety of functionals. Using the B3LYP hybrid functional, the top and fcc hollow sites have the same energy; using the PW91 functional, hollow site adsorption is favoured by 30 kJ mol^{-1}. They suggested using a hybrid B3LYP functional which would favour atop adsorption by the correct 20 kJ mol^{-1}. The reasoning was that the PW91 functional places occupied adsorbate energy levels too close to the metal Fermi level when compared with B3LYP.

It is not certain, however, that the DFT/GGA approach cannot work for this system. For example, Olsen [54], used a LCAO methodology and obtained the correct binding site preference. The error for relative adsorption sites was suggested to be within 10 kJ mol^{-1} of experimental results. If the error was within 10 kJ mol^{-1}, other parameters such as geometries and vibrational frequencies agreed with experiment. Orita [55] used all electron relativistic (AER) calculations with different functionals and found that it gave a deeper Fermi level leading to a correct prediction of binding site. However, this is still an ongoing field of research and there is not yet a definitive solution to be able to consistently predict the correct binding site of CO on Pt (111).

2.1.4 Adsorption of ethene onto Group 10 metal surfaces

The adsorption of ethene onto the surface of Group 10 transition metals, such as platinum, has been widely studied in terms of both structure and as part of its role in hydrogenation reaction processes. Since the earliest studies, it has been known that, irrespective of adsorption site, two types of interaction with the surface are possible (Fig. 2.5). The two modes both involve adsorption

with the C=C bond parallel to the surface plane, but with interaction *via* either one metal atom (a π-bonding mode) or two (known as a di-σ mode). In the di-σ mode, more distortion will occur which results in a more sp^3-like structure for the ethene molecule [56].

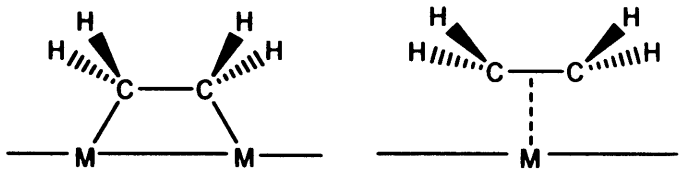

Figure 2.5: Types of interaction for ethene on a (111) metal surface: di-σ (left) and π (right)

The relative populations of these adsorption modes will be present is a function of the temperature of the system. At low temperatures (below 50 K), UPS measurements have indicated that the π-bound mode is present on the surface [57] but not di-σ. Above this temperature, EELS and TDS measurements have confirmed that the di-σ bound mode is present [58,59]. As the temperature is raised above 300 K, part of the adsorbate layer desorbs and part is converted to an ethylidene (CCH_3) species [60].

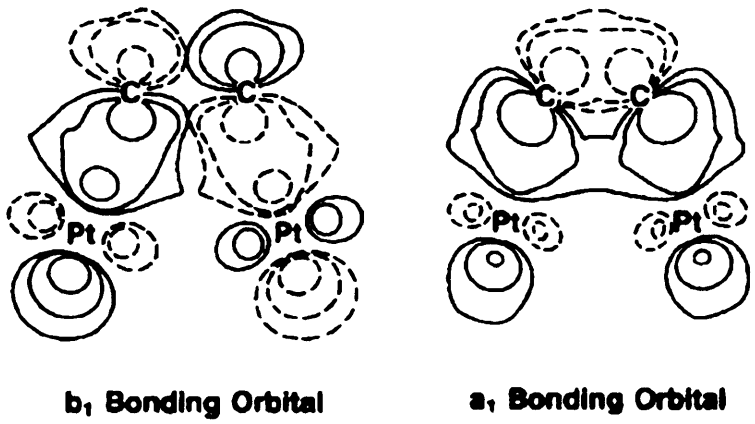

Figure 2.6: Primary bonding orbitals formed between ethene and a platinum surface. From reference [61]

The bonding of ethene to a Pt surface has been studied using Near Edge X-ray Adsorption Fine Structure (NEXAFS) [61]. At about 90 K, the di-σ sp^3-like adsorbate was found, and ethylidene was produced above 300 K. Fig. 2.6 shows the two primary bonding orbitals formed from ethene and the platinum surface. It can be seen that the b_1 orbital is a combination of the ethene π^* orbital and the metal d-orbitals, whereas the a_1 orbital is a mixture of the π-orbital and σ orbitals from the metal.

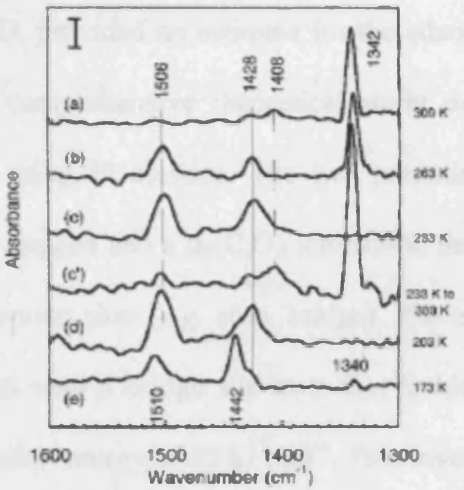

Figure 2.7: IR spectra for ethene on a Pt/SiO_2 catalyst as a function of temperature. From reference [62].

Microcalorimetry and IR spectroscopy was used to study the effect of temperature on the type of species adsorbed for ethene on a Pt/SiO_2 catalyst (Fig. 2.7) [62]. At 173 K, contributions are seen from ethene adsorption on both the metal and the silica support (bands at 1442 and 1340 cm^{-1} are from silica adsorption). At 203 K and 233 K adsorption is only seen on the metal itself, no silica adsorption is present. A change in the heat of adsorption at 263 K indicated that as well as the bound ethene, ethylidene is being formed on the surface. The main species at 300K (band at 1342 cm^{-1}) is shown to be ethylidene. The heat of adsorption at 173, 203 and 233 K is estimated to be 125 kJ mol^{-1}.

The binding energy as a function of adsorption site has also been studied using theoretical techniques. Using periodic DFT to study different binding sites [63] suggested that adsorption into a

di-σ bridge site is most favourable (107 kJ mol^{-1}), concurring with the experimental evidence presented above. Adsorption into fcc (67 kJ mol^{-1}) and hcp (64 kJ mol^{-1}) hollow sites and the atop site (53 kJ mol^{-1}) is less favourable. This was confirmed in a further study with the VASP code [64] which yielded values of 127 kJ mol^{-1} (bridge), 71-75 kJ mol^{-1} (hollow) and 85-86 kJ mol^{-1} (atop).

2.1.5 Adsorption of formaldehyde and acetone onto Group 10 metal surfaces

The adsorption of formaldehyde onto the Pt (111) surface has attracted less interest than ethene, although research has been carried out into formaldehyde dimerisation. Early experimental studies, using HREELS and TPD, provided an estimate for the adsorption energy of approximately 52 kJ mol^{-1} [65,66]. The first comprehensive theoretical study of adsorption geometry was an Extended Hückel investigation using Pt clusters. The two potential adsorption modes, an η^1(O) interaction through the terminal oxygen and a μ_2(C,O) interaction through the C and O atoms, were tested for several different adsorption sites (*e.g.* atop, bridge). The most favourable interaction was found to be a μ_2 mode adsorbed onto a bridge site in a di-σ fashion similar to that observed for ethene, with an estimated adsorption energy of 95 kJ mol^{-1}. This involved interaction of the π and π* orbitals of the formaldehyde with the metal. The only other possible adsorption mode found was a η^1 interaction on an atop site (46 kJ mol^{-1}) which mostly involved the p_z orbital of the adsorbate interacting with the surface. Although the μ_2 mode was more stable, the energy difference was sufficiently small that the η^1 species is a viable surface adsorption species.

These findings have been confirmed by more recent periodic DFT investigations. Desai, for example, found the μ_2 di-σ mode to have an adsorption energy of 49 kJ mol^{-1}, in agreement with experiment [67]. Hirschl found the same geometry to have an adsorption energy of 44 kJ mol^{-1} [68]; the equivalent π-interaction only had an adsorption energy of 2 kJ mol^{-1}.

Early studies of the adsorption of acetone onto Pt surfaces (using EELS and TDS) suggested two distinct adsorption modes [69]. The most prevalent mode was a weakly-bound form which reversibly desorbed at 185 K (suggesting an estimated 49 kJ mol^{-1} adsorption energy) (Figure 2.8); the carbonyl stretching frequencies suggested an end-on (η^1) adsorption mode, with the Pt-O-C angle bent in the molecular plane. A secondary mode, which partially desorbs and decomposes at about 230 K, was tentatively assigned to a μ_2 (C,O) mode and it was suggested that this adsorption mode may occur primarily at step sites. Further RAIRS and HREELS studies [70] also found two adsorption modes. The primary mode was again assigned to an end-on (η^1 (O)) adsorption mode with a characteristic C-O stretch at 1638 cm^{-1}. The secondary TDS peak can be seen in Fig. 2.8 on the desorption trace of acetone (line C). This was more difficult to locate, but was assigned to a μ_2 (C,O) mode.

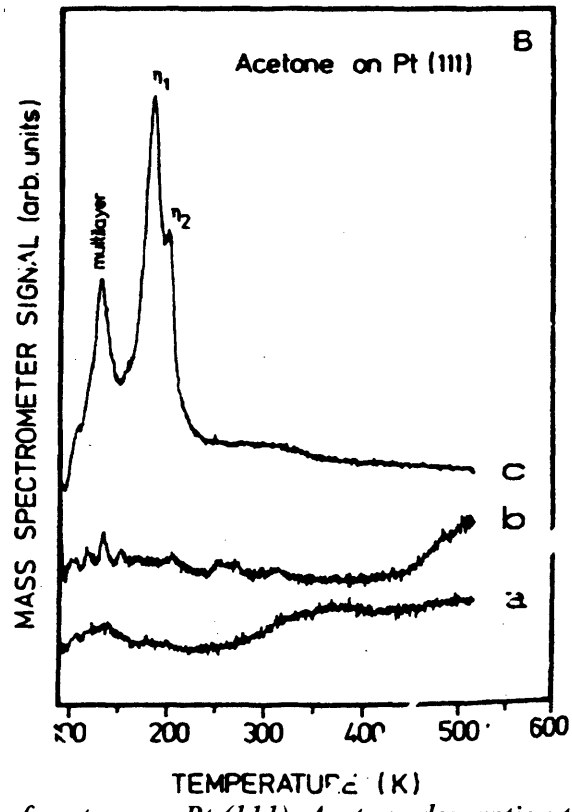

Figure 2.8: TDS spectrum of acetone on Pt (111). Acetone desorption trace shown as line C. From reference [70].

These two adsorption modes were further investigated using theoretical calculations. Hückel theory calculations [71], for example, considered three μ^2 and three η^1-type adsorption modes. The most stable adsorption site was a η^1 (O) mode where the oxygen interacts with an atop site on the platinum surface. The μ^2 (C,O) mode was also stable, preferring a di-σ bridge-type site. Calculations using a 19-atom Pt cluster [72] but with a fixed Pt interatomic distance, found the η^1 (O) mode to be the most stable with an adsorption energy of between 29 and 50 kJ mol^{-1} depending on the basis set used and the exact adsorption geometry. The μ^2 (C,O) had an adsorption energy of between 4 and 29 kJ mol^{-1} depending on the basis set used and exhibited an elongated C=O bond of a length closer to a C-O single bond.

Acetone and related ketones can also exist in the enol or enolate ion form. These two forms offer distinct possibilities for differing chemistry on the surface, but to date there has been relatively little study in this field. Enolate species are known as being important surface intermediates for acetone condensation [73,74] and deuteration experiments have positively identified the enol form of methyl pyruvate during its hydrogenation over a Pd surface [75]. Deuteration occurred across the C=C bond present in the enol form, whereas the C=O bond should have been deuterated if the acetone was in the ketone form. However there have been few direct studies regarding the structure and stability of these species. One of the exceptions is a RAIRS study of acetone in the enolate form on a Ni (111) surface [76]. The spectrum is shown in Fig. 2.9 and shows a C-O stretch of the enolate at 1545 cm^{-1}. It is suggested that enolate formation occurs by the removal of a proton from the hydroxyl oxygen of the enol form of acetone either by the Ni itself or by basic oxygen atoms.

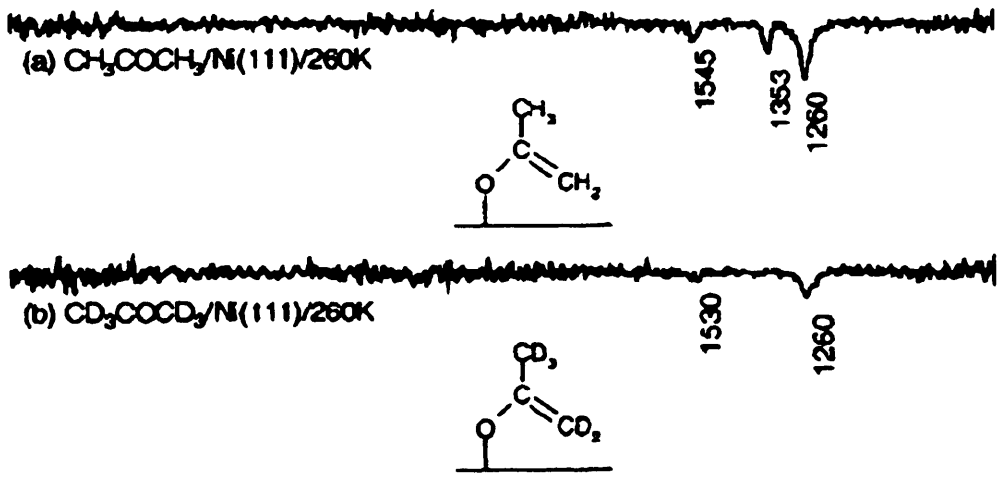

Figure 2.9: RAIRS spectrum of the enolate form of acetone and deuterated acetone. From reference [76].

2.2 Enantioselective hydrogenation reactions

The ultimate aim of this study is to begin to simulate metal-catalysed enantioselective hydrogenation reactions. A simple metal catalyst-system will produce a racemic mix of enatiomers; a 'chiral environment' is needed in order for enantiodifferentiation to occur. There are two principal methods by which this can be achieved; i) the metal is loaded onto a chiral support or ii) a chiral 'modifier' is adsorbed onto the metal catalyst. The first technique was pioneered in the 1930s [77] using metal supported on a quartz surface. However, it is the second technique which has attracted more recent study. The nature of the chiral modifier is of paramount importance as not all potential modifiers will work in a real heterogeneous catalytic environment. Common choices include optically active acids such as tartaric acid (*e.g.* methyl acetoacetate on Ni [78] or reference [79] for a review) or alkaloids (*e.g.* α-phenylcinnamic acid with cinchonidine-modified Pd [80]). It is this latter type of reaction, using cinchona alkaloid-modified Pd and Pt metal catalysts, which is the subject of much of the work in this thesis.

2.2.1 Enantioselective hydrogenation of α-ketoesters over alkaloid-modified catalysts

The second methodology described above, the use of a chiral modifier, came to prominence in the late 1970s when a Japanese research group used a Pt/C catalyst modified by cinchonidine for the enantioselective hydrogenation of methyl pyruvate [81]. They found that the enantiomeric nature of the product that was formed was dependent upon the chiral modifier that was used. When cinchonidine or quinine was used the *R* methyl lactate was produced, whereas the *S* product was favoured when the modifier was replaced by cinchonine or quinidine. Other factors affecting the

purity of the product formed were found to be the type of support, solvent and type of alkaloid used. A summary of this class of reaction is shown below in Fig. 2.10.

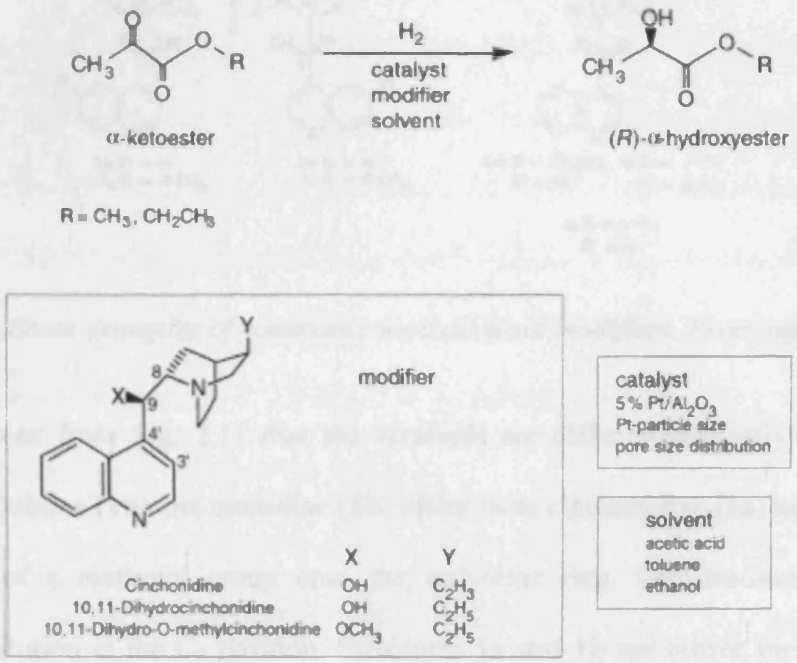

Figure 2.10: Generic reaction scheme for the enantioselective hydrogenation of α-ketoesters to α-hydroxyesters using a cinchonidine-modifier Pt surface. From reference [82].

2.2.2 Proposed reaction mechanisms and the structure of the modifier

The structure of some of the more commonly used alkaloid modifiers is defined below in Fig. 2.11.

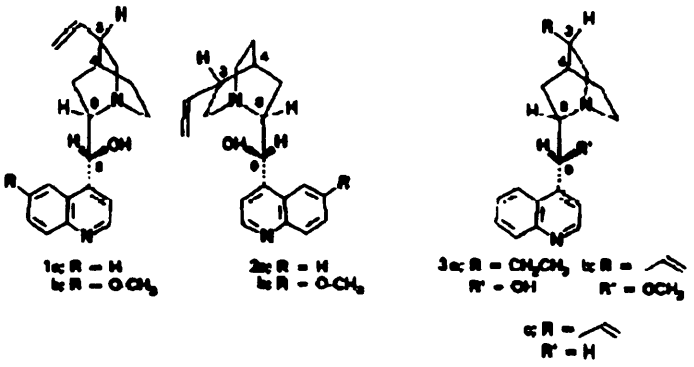

Figure 2.11: Some examples of commonly used alkaloid modifiers. From reference[83].

It can be seen from Fig. 2.11 that the alkaloids are differentiated only by substitution at certain positions. Quinine (**1b**) and quinidine (**2b**) differ from cinchonidine (**1a**) and cinchonine (**2a**) only substitution of a methoxy group onto the quinoline ring. Dihydrocinchonindine (**3a**) is produced by substitution at the C_9 position. Structures **1a** and **1b** are mirror images of **2a** and **2b** apart from the chiral centre at position C_3; this chiral centre (and also that at C_4) is not thought to affect the enantioselectivity of the product. The configurations at C_8 (*S* for **1a** and **1b**, *R* for **2a** and **2b**) and C_9 (*R* for **1a** and **1b**, *S* for **2a** and **2b**) are thought to determine the enantioselectivity of the product [84]. For example, with Pt-based catalysts, quinine and cinchonidine (**1a**, **1b**) produce an *R* product, whereas quinidine and cinchonine (**2a**, **2b**) produce an *S* product [85]. However, when Pd is used as the metal in the system, this is reversed; cinchonine produces an *R* product and cinchonidine produces an *S* product [75]. Dihydrocinchonidine (**3a**) also produced an *R* product on Pt, but with an enhanced *ee* compared to the other derivatives [86]. Substitution at the C_9 position with H (**3c**) showed a large decrease in *ee* [87]; this was not observed when the substitution was made with a

methoxy group (**3b**) leading to the conclusion that the oxygen at position C_9 is of importance to the catalytic process.

A large volume of work has been performed in order to attempt to maximise the performance of the catalytic system and to gain an insight into the mechanism by which the hydrogenation occurs. Studies have suggested a link between catalysts which have a low dispersion or large metal particle size and an increased *ee* [88]. Examples of the type of catalysts successfully used include Pt/Al_2O_3 [89], Pt/SiO_2 [90] and even zeolites [91]. The modifier:catalyst ratio is also relatively unimportant; the ideal ratio was found to be a small amount of modifier per unit catalyst, and increasing the amount of modifier had negligible effects [89,92].

The exact mechanism of reaction has yet to be fully elucidated. However, several schemes have been proposed which will be discussed below.

One of the most commonly used models is the template mechanistic model, originally proposed by Wells [93,94]. This model originally suggested that the modifier adsorbs onto the surface and produces an array of chiral templates (an L-shaped adsorption mode) with areas between the modifier where the adsorbate could adsorb to undergo hydrogenation. The nature of the surface-modifier interaction was never fully described, and attempts to locate the array of templates were unsuccessful [95]. This led to modification of the model, in which a 1:1 complex between modifier and reactant was proposed. The rate enhancement was suggested to be due to hydrogen bonding between the half-hydrogenated reactant and the quinuclidene nitrogen atom of the modifier. An alternative model along similar lines was proposed by Augustine, involving a bidentate interaction between modifier and reactant whereby a six-membered ring was formed involving the quinuclidene nitrogen atom and the oxygen atom located at C_9. [83,96]. Interaction between modifier and surface was thought to be in an end-on fashion, although this was later revised to favour a parallel

adsorption mode with hydrogenation occurring at the corner sites and atoms on the surface. Today, this model is generally discounted as it does not explain the continued stereoselectivity upon further substitution at C_9 as discussed previously (which should sterically hinder this interaction) and the fact that enantioselectivity can be observed even when there is a low proportion of corner sites on the surface [97].

The main opponent of the Wells template model proposed an alternative model whereby the reactant:modifier interaction occurs in the liquid phase before adsorption onto the surface [98,99]. A 1:1 complex is formed between the aromatic ring of the modifier and the π-orbitals of the reactant; adsorption occurs *via* the opposite site of the complex leading to one preferential enantiomer (hence the term 'shielding model' was coined for this proposal). This model falls down, however, as it cannot explain certain experimental behaviour; *e.g.* enhancement of *ee* upon protonation of the quinuclidene nitrogen, the low modifier:reactant ratio needed to achieve enantiodifferentiation, continued enantioselectivity even when an open conformer for the modifier is used [100] (this model will only work with a closed conformer) and various kinetic observations [101].

The model which is most used to describe this system at present was developed by the Baiker group, and is an extension of the Wells model. Under suitably acidic conditions (e.g. acetic acid as a solvent) the quinuclidene nitrogen atom is known to be protonated [102]. This proton can interact with the adsorbate (e.g. through a hydrogen bond to the carbonyl oxygen atom) to form a surface reactant complex [103]. Under other solvents, such as ethanol, the hydrogen bond can be formed by half-hydrogenation of the carbonyl bond to interact with the quinuclidene in a hydrogen bond in which the nitrogen acts as an acceptor [82]. This model has been backed up by theoretical calculations using the Gaussian package [104]. When *s-trans* methyl pyruvate was interacted with cinchonidine, the pro-*R* complex was favoured by 7.5 kJ mol^{-1}, which was calculated to lead to an *ee*

of approximately 92% (in agreement with experiment). With *s-cis* methyl pyruvate, the pro-*R* complex was only favoured by 0.8 kJ mol^{-1}, leading to an *ee* of just 17%. However, the *s-cis* complexes were found to be more stable due to the larger dipole moment, which is in contradiction to the higher experimental *ee*. However, this discrepancy was reduced when the calculations were repeated applying a continuum solvent model.

The structure of modifiers such as cinchonidine allows a good deal of conformational flexibility. The bridged bond between the quinuclidene and quinidine rings (C_8 to C_9) allows rotation of the two ring systems relative to each other. The terminology "open" and "closed" is used to differentiate between the quinuclidene nitrogen atom pointing away or towards the quinidine ring. The conformation of the alkaloid will affect the interaction with the reactant, and certain conformations are required in order to be able to obtain the correct product [105]. Experimental investigations using NOESY spectroscopy suggested that 90% of cinchonidine will exist in the conformation known as Open(3) [106] (Fig. 2.12). This was confirmed by theoretical calculations using both force field and *ab initio* calculations; Closed(1) was the most stable closed structure but was 4-12 kJ mol^{-1} less stable than Open(3) [105]. The structures of these two conformers are shown in Fig. 2.12. These findings have been confirmed independently using different semi-empirical or low-level models (for examples see [107,108]).

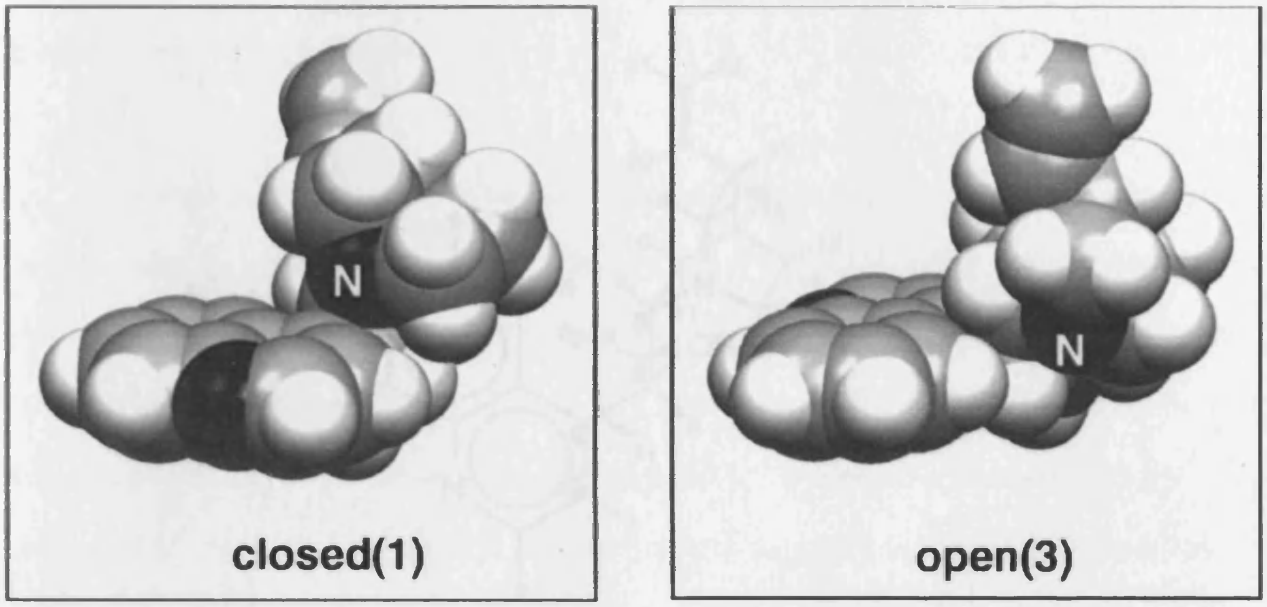

Figure 2.12: The two most stable conformations of cinchonidine. Nitrogen atoms colored black. From reference [105].

More rigorous calculations employing HF/6-31G** or greater found that the Open(3) conformer was again the most stable, and Closed(1) was the most stable closed conformer (about 4 kJ mol^{-1} less stable than Open (3)) [109] when non-polar solvents are used. The conformers can defined using several key torsion angles; τ_1 (C_3-C_4-C_9-C_8), τ_2 (C_4-C_9-C_8-N) and τ_3 (H_9-C_8-C_9-H_8) which are defined on Fig. 2.13.

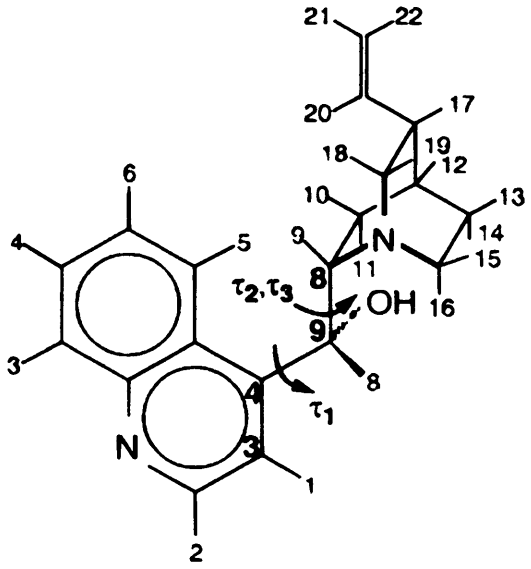

Figure 2.13: The structure of cinchonidine, highlighting the three key torsion angles used to distinguish between conformers. From reference [109].

The values obtained for Open(3) and Closed(1) were: τ_1 101, -107; τ_2 154, 58 and τ3 -78, -177 respectively. However, when a solvent model is applied the closed conformers are stabilised due to their larger dipole moments compared to the open conformers in a polar solvent. Up to 50% of cinchonidine is expected to be in the closed form in a strong polar solvent.

The final aspect of the modifier which must be taken into account is the way it will interact with the surface. As suggested previously when discussing possible models for the reaction, two adsorption modes can be envisaged: 'end-on' via the quinoline N lone pair or parallel via the aromatic π-system of the quinoline. NEXAFS studies have concluded that the latter adsorption more is the most likely [110]; this was confirmed by H/D exchange experiments [94].

2.2.3 Structure of the α-ketoester reactant

α-Ketoesters such as methyl pyruvate (MP) exist in both *s-cis* and *s-trans* conformations. In the gas-phase, the *s-trans* conformation is preferred by approximately 4.4 kJ mol^{-1}, leading to a 6:1 *s-trans* : *s-cis* ratio; the barrier to rotation was found to be only 7.3 kJ mol^{-1} [111]. A combined IR/theoretical study echoed these conclusions; however, under a strong polar solvent, the *s-cis* structure is stabilised due to the larger dipole moment [102]. When methyl pyruvate interacts with a metal surface, there are two principle adsorption modes suggested. XPS and UPS measurements [112] show a large amount of lone pair bonding between ethyl pyruvate (EP) and the surface, implying adsorption perpendicular to the surface via the two carboxyl oxygen atoms. Work function measurements from this study, however, suggest that adsorption perpendicular to the surface plane is unlikely, and a tilted adsorption geometry is more likely. XANES studies [113] have revealed a mixture of adsorption geometries depending on the hydrogen coverage of the surface. In the absence of hydrogen, perpendicular adsorption is seen; with hydrogen, the EP is tilted towards to the surface (angle between C=O bond and the surface 72-58°) and bonding is primarily via the π-system. The suggestion may be, therefore, that a mixed system containing both types of ketoester may exist.

The sole rigorous theoretical study [72] using a cluster model of the platinum surface and MP as the adsorbate, with the ADF code, suggests that the primary adsorption mode is the tilted adsorption mode described above. Adsorption in the *cis* form of methyl pyruvate tilted towards the surface, with the primary interaction with the surface through the keto-carbonyl moiety, is found to be the most favourable. Clearly there is a degree of ambiguity regarding the adsorption of the

ketoester onto the surface and this is complicated by hydrogenation of the surface. In order to match the suggested models for the hydrogenation system, however, the adsorption mode needs to be as flat as possible.

2.3 Conclusions

To date, there is a wealth of experimental evidence regarding the enantioselective hydrogenation of ketoesters over a metal surface modifier with a cinchona alkaloid. Several different models have been suggested and are supported by relevant experimental data. However, it is clear that the application of theoretical techniques to this field has fallen behind compared to experimental progress. It has been proven, as discussed in this chapter, that theory can produce reliable data regarding the adsorption of molecules on metal surfaces and that this data corresponds well with experimental methods and can be used to help and interpret experiment.

Therefore, what is necessary is the application of more theoretical methods to the hydrogenation system. The techniques applied so far have been mostly lacking in method (*e.g.* a limited size metal-cluster model of the surface) or application (*e.g.* the freezing of modifier atomic positions to preserve planarity). Therefore, it is hoped that this study will provide an opportunity to expand on the work already completed in this area of study and develop new methodology to study the hydrogenation system as a whole.

2.4 References

(1) Lovvik, O. M.; Olsen, R. A. *Phys. Rev. B.* **1998**, *58*, 10890.
(2) Casalone, G.; Cattania, M. G.; Simonetta, M.; Tescari, M. *Chem. Phys. Lett.* **1979**, *61*, 36.
(3) Himpsel, F. J.; Knapp, J. A.; Eastman, D. E. *Phys. Rev. B.* **1979**, *19*, 2872.
(4) Norskov, J. K. *Phys. Rev. Lett.* **1982**, *48*, 1620.
(5) Daw, M. S.; Baskes, M. I. *Phys. Rev. B.* **1984**, *29*, 6443.
(6) Yang, H.; Whitten, J. L. *J. Chem. Phys.* **1993**, *98*, 5039.
(7) Klinke, D. J.; Broadbelt, L. J. *Surf. Sci.* **1999**, *429*, 169.
(8) Kresse, G.; Hafner, J. *Surf. Sci.* **2000**, *459*, 287.
(9) Felter, T. E.; van Hove, M. A. *Phys. Rev. B.* **1989**, *40*, 891.
(10) Hsu, C.-H.; Larson, B. E.; El-Batanouny, M.; Willis, C. R. *Phys. Rev. Lett.* **1991**, *66*, 3164.
(11) Muscat, J. P. *Phys. Rev. B.* **1986**, *33*, 8136.
(12) Daw, M. S.; Foiles, S. M. *Phys. Rev. B.* **1987**, *35*, 2128.
(13) Dong, W.; Kresse, G.; Furthmüller, J.; Hafner, J. *Phys. Rev. B.* **1996**, *54*, 2157.
(14) Watson, G. W.; Wells, R. P. K.; Willock, D. J.; Hutchings, G. J. *J. Phys. Chem. B.* **2001**, *105*, 4889.
(15) Koeleman, B. J. J.; de Zwart, S. T.; Boers, A. K.; Poelsema, B.; Verheij, L. K. *Phys. Rev. Lett.* **1986**, *56*, 1152.
(16) Lui, K. M.; Kim, Y.; Lau, W. M.; Rabalais, J. W. *J. App. Phys.* **1999**, *86*, 5256.
(17) Papoian, G.; Norskov, J. K.; Hoffmann, R. *J. Am. Chem. Soc.* **2000**, *122*, 4129.
(18) Fearon, J.; Watson, G. W. *J. Mater. Chem.* **2006**, *16*, 1989.
(19) Légaré, P. *Surf. Sci.* **2004**, *559*, 169.
(20) Greeley, J.; Mavrikakis, M. *J. Phys. Chem. B.* **2005**, *109*, 3460.
(21) Ceyer, S. T. *Acc. Chem. Res.* **2001**, *34*, 737.
(22) Daley, S. P.; Utz, A. L.; Trautman, T. R.; Ceyer, S. T. *J. Am. Chem. Soc.* **1994**, *116*, 6001.
(23) Haug, K. L.; Burgi, T.; Trautman, T. R.; Ceyer, S. T. *J. Am. Chem. Soc.* **1998**, *120*, 8885.
(24) Johnson, A. D.; Maynard, K. J.; Daley, S. P.; Yang, Q. Y.; Ceyer, S. T. *Phys. Rev. Lett.* **1991**, *67*, 927.
(25) Ferguson, G. A. J.; Schindler, A. I.; Tanaka, T.; Morita, T. *Phys. Rev.* **1965**, *137*, 483.
(26) Martins, M. E.; Zinola, C. F.; Andreason, G.; Salvarezza, R. C.; Arvia, A. J. *J. Electronanal. Chem.* **1998**, *445*, 135.
(27) Lagos, M.; Ramirez, R.; Schuller, I. K. *Phys. Rev. B.* **1988**, *38*, 10042.
(28) Wonchoba, S. E.; Truhlar, D. G. *Phys. Rev. B.* **1996**, *53*, 11222.
(29) Ledentu, V.; Dong, W.; Sautet, P. *J. Am. Chem. Soc.* **2000**, *122*, 1796.
(30) Greeley, J.; Mavrikakis, M. *Surf. Sci.* **2003**, *540*, 215.
(31) Christensen, O. B.; Stoltze, P.; Jacobsen, K. W.; Norskov, J. K. *Phys. Rev. B.* **1990**, *41*, 12413.
(32) Caputo, R.; Alavi, A. *Mol. Phys.* **2003**, *101*, 1781.
(33) Bertolini, J. C.; Dalmai-Imelik, G.; Rousseau, J. *Surf. Sci.* **1977**, *68*, 539.
(34) Kevan, S. D.; Davis, R. F.; Rosenblatt, D. H.; Tobin, J. G.; Mason, M. G.; Shirley, D. A.; Li, C. H.; Tong, S. Y. *Phys. Rev. Lett.* **1981**, *46*, 1629.
(35) Persson, B. N. J.; Ryberg, R. *Phys. Rev. Lett.* **1985**, *54*, 2119.

(36) Davila, M. E.; Asensio, M. C.; Woodruff, D. P.; Schindler, K.-M.; Hofmann, P.; Weiß, K.-U.; Dippel, R.; Gardner, P.; Fritzsche, V.; Bradshaw, A. M.; Conesa, J. C.; González-Elipe, A. R. *Surf. Sci.* **1994**, *311*, 337.
(37) Mapledoram, L. D.; Bessent, M. P.; Wander, A.; King, D. A. *Chem. Phys. Lett.* **1994**, *228*, 527.
(38) Davis, R.; Woodruff, D. P.; Hofmann, P.; Schaff, O.; Fernandez, V.; Schindler, K.-M.; Fritzsche, V.; Bradshaw, A. M. *J. Phys.: Condens. Matter* **1996**, *8*, 1367.
(39) Held, G.; Schuler, J.; Sklarek, W.; Steinrück, H.-P. *Surf. Sci.* **1998**, *398*, 154.
(40) Hammer, B.; Hansen, L. B.; Nørskov, J. K. *Phys. Rev. B* **1999**, *59*, 7413.
(41) Johnson, P. D.; Hulbert, S. L. *Phys. Rev. B* **1987**, *35*, 9427.
(42) Bradshaw, A. M.; Hoffmann, F. M. *Surf. Sci.* **1978**, *72*, 513.
(43) Conrad, H.; Ertl, G.; Koch, J.; Latte, E. E. *Surf. Sci.* **1974**, *43*, 462.
(44) Sautet, P.; Rose, M. K.; Dunphy, J. C.; Behler, S.; Salmeron, M. *Surf. Sci.* **2000**, *453*, 25.
(45) Blackman, G. S.; Xu, M.-L.; Ogletree, D. F.; Van Hove, M. A.; Somorjai, G. *Phys. Rev. Lett.* **1988**, *61*, 2352.
(46) Hopster, H.; Ibach, H. *Surf. Sci.* **1978**, *77*, 109.
(47) Bocquet, M. L. *Surf. Sci.* **1996**, *360*, 128.
(48) Pederson, M. O.; Bocquet, M. L.; Sautet, P.; Laegsgaard, E.; Stensgaard, I.; Besenbacher, F. *Chem. Phys. Lett.* **1999**, *299*, 403.
(49) Lynch, M.; Hu, P. *Surf. Sci.* **2000**, *458*, 1.
(50) Watwe, R.; Spiewak, B. E.; Cortright, R. D.; Dumesic, J. *Catal. Lett.* **1998**, *51*, 139.
(51) Feibelman, P. J.; Hammer, B.; Nørskov, J. K.; Wagner, F.; Scheffler, M.; Stumpf, R.; Watwe, R.; Dumesic, J. *J. Phys. Chem. B* **2001**, *105*, 4018.
(52) Grinberg, I.; Yourdshahyan, Y.; Rappe, A. M. *J. Chem. Phys.* **2002**, *117*, 2264.
(53) Gil, A.; Clotet, A.; Ricart, J. M.; Kresse, G.; García-Hernández, M.; Rösch, N.; Sautet, P. *Surf. Sci.* **2003**, *530*, 71.
(54) Olsen, R. A.; Philipsen, P. H. T.; Baerends, E. J. *J. Chem. Phys.* **2003**, *119*, 4522.
(55) Orita, H.; Itoh, N.; Inada, Y. *Chem. Phys. Lett.* **2004**, *384*, 271.
(56) Cremer, P. S.; Stanners, C.; Niemantsverdriet, J. W.; Shen, Y. R.; Somorjai, G. A. *Surf. Sci.* **1995**, *328*, 111.
(57) Cassuto, A.; Kiss, J.; White, J. M. *Surf. Sci.* **1991**, *255*, 289.
(58) Demuth, J. E. *Surf. Sci.* **1979**, *80*, 367.
(59) Ibach, H. *J. Vac. Sci. Tech* **1978**, *15*, 407.
(60) Steininger, H.; Ibach, H.; Lehwald, S. *Surf. Sci.* **1982**, *117*, 685.
(61) Horsley, J. A.; Stohr, J.; Koestner, R. J. *J. Chem. Phys.* **1985**, *83*, 3146.
(62) Shen, J.; Hill, J. M.; Watwe, R. M.; Spiewak, B. E.; Dumesic, J. A. *J. Phys. Chem. B* **1999**, *103*, 3923.
(63) Ge, Q.; King, D. A. *J. Chem. Phys.* **1999**, *110*, 4699.
(64) Watson, G. W.; Wells, R. P. K.; Willock, D. J.; Hutchings, G. J. *J. Phys. Chem. B* **2000**, *104*, 6439.
(65) Abbas, N. M.; Madix, R. J. *Appl. Surf. Sci.* **1981**, *7*, 241.
(66) Henderson, M. A.; Mitchell, G. E.; White, J. M. *Surf. Sci.* **1987**, *188*, 206.
(67) Desai, S. K.; Neurock, M.; Kourtakis, K. *J. Phys. Chem. B* **2002**, *106*, 2559.
(68) Hirschl, R.; Eichler, A.; Hafner, J. *J. Catal.* **2004**, *226*, 273.
(69) Avery, N. R. *Surf. Sci. Lett.* **1983**, *125*, 70.
(70) Vannice, M. A.; Erley, W.; Ibach, H. *Surf. Sci.* **1991**, *254*, 1.

(71) Delbecq, F.; Sautet, P. *Surf. Sci.* **1993**, *295*, 353.
(72) Vargas, A.; Bürgi, T.; Baiker, A. *J. Catal.* **2004**, *222*, 439.
(73) Busca, G.; Lorenzelli, V. *J. Chem. Soc. Faraday Trans. 1* **1982**, *78*, 2911.
(74) Zaki, M. I.; Hasan, M. A.; Al-Sagheer, F. A.; Pasupulety, L. *Langmuir* **2000**, *16*, 430.
(75) Hall, T. J.; Johnston, P.; Vermeer, W. A. H.; Watson, S. R.; Wells, P. B. *Stud. Surf. Sci. Catal.* **1996**, *101*, 221.
(76) Sim, W.-S.; Li, T.-C.; Yang, P.-X.; Yeo, B.-S. *J. Am. Chem. Soc.* **2002**, *124*, 4970.
(77) Schwab, G.-M.; Rudolph, L. *Naturwiss* **1932**, *20*, 362.
(78) Osawa, T.; Hayashi, Y.; Ozawa, A.; Harada, T.; Takayasu, O. *J. Mol. Cat. A* **2001**, *169*, 289.
(79) Osawa, T.; Harada, T.; Takayasu, O. *Top. Catal.* **2000**, *13*, 155.
(80) Nitta, Y. *Top. Catal.* **2000**, *13*, 179.
(81) Orito, Y.; Imai, S.; Niwa, S.; Hung, N. G. *J. Synth. Org. Chem. Jpn.* **1979**, *37*, 173.
(82) Baiker, A. *J. Mol. Cat. A* **2000**, *163*, 205.
(83) Augustine, R. L.; Tanielyan, S. K.; Doyle, L. K. *Tetrahedron Asymm.* **1993**, *4*, 1803.
(84) Verpoorte, R.; Schripsema, J.; van der Laap, T. In *The Alkaloids, Vol. 34*; Brossi, A., Ed.; Academic Press: New York, 1998, p 331.
(85) Orito, Y.; Imai, S.; Niwa, S. *Nippon Kagaku Kaishi* **1980**, 670.
(86) Meheux, P. A.; Ibbotson, A.; Wells, P. B. *J. Catal.* **1991**, *128*, 387.
(87) Blaser, H. U.; Muller, M. *Stud. Surf. Sci. Catal.* **1991**, *59*, 73.
(88) Wehrli, J. T.; Baiker, A.; Monti, D. M.; Blaser, H. U. *J. Mol. Cat.* **1990**, *61*, 207.
(89) Blaser, H. U.; Jalett, H. P.; Monti, D. M.; Reber, J. F.; Wehrli, J. T. *Stud. Surf. Sci. Catal.* **1988**, *41*, 153.
(90) Bond, G.; Wells, P. B. *App. Catal.* **1985**, *18*, 221.
(91) Reschetilowski, W.; Bohmer, U.; Wiehl, J. *Stud. Surf. Sci. Catal.* **1994**, *84*, 2021.
(92) Bond, G.; Simons, K. E.; Ibbotson, A.; Wells, P. B.; Whan, D. A. *Catal. Today* **1992**, *12*, 421.
(93) Webb, G.; Wells, P. B. *Catal. Today* **1992**, *12*, 319.
(94) Sutherland, I. M.; Ibbotson, A.; Moyes, R. B.; Wells, P. B. *J. Catal.* **1990**, *125*, 77.
(95) Simons, K. E.; Meheux, P. A.; Griffiths, S. P.; Sutherland, I. M.; Johnston, P.; Wells, P. B.; Carley, A. F.; Rajumon, M. K.; Roberts, M. W.; Ibbotson, A. *Recl. Trav. Chim. Pays-Bas* **1994**, *113*, 465.
(96) Augustine, R. L.; Tanielyan, S. K. *J. Mol. Cat. A* **1996**, *112*, 93.
(97) Mallat, T.; Frauchiger, S.; Kooyman, P. J.; Schurch, M.; Baiker, A. *Catal. Lett.* **1999**, *663*, 121.
(98) Margitfalvi, J. L.; Hegedus, M.; Tfirst, E. *Stud. Surf. Sci. Catal.* **1996**, *101*, 241.
(99) Margitfalvi, J. L.; Tfirst, E. *J. Mol. Cat. A* **1999**, *139*, 81.
(100) Bartok, M.; Felföldi, K.; Szöllösi, G.; Bartok, T. *Catal. Lett.* **1999**, *61*, 1.
(101) Blaser, H. U.; Jalett, H. P.; Garland, M.; Studer, M.; Thies, H.; Wirth-Tijani, A. *J. Catal.* **1998**, *173*, 282.
(102) Ferri, D.; Bürgi, T.; Baiker, A. *J. Chem. Soc. Perkin Trans. 2* **2000**, *2*, 221.
(103) Schwalm, O.; Weber, J.; Minder, B.; Baiker, A. *Int. J. Quant. Chem.* **1994**, *52*, 191.
(104) Bürgi, T.; Baiker, A. *J. Catal.* **2000**, *194*, 445.
(105) Schürch, M.; Schwalm, O.; Mallat, T.; Weber, J.; Baiker, A. *J. Catal.* **1997**, *169*, 275.
(106) Dijkstra, G. D. H.; Kellogg, R. M.; Wynberg, H.; Svendsen, J. S.; Marko, I.; Sharpless, K. B. *J. Am. Chem. Soc.* **1989**, *111*, 8069.
(107) Dijkstra, G. D. H.; Kellogg, R. M.; Wynberg, H. *J. Org. Chem.* **1990**, *55*, 6121.

(108) Berg, U.; Aune, M.; Matsson, O. *Tetrahedron Lett.* **1995**, *36*, 2137.
(109) Bürgi, T.; Baiker, A. *J. Am. Chem. Soc.* **1998**, *120*, 12920.
(110) Evans, T.; Woodhead, A. P.; Gutierrez-Soza, A.; Thornton, G.; Hall, T. J.; Davis, A. A.; Young, N. A.; Wells, P. B.; Oldman, R. J.; Plashkevych, O.; Vahtras, O.; Agren, H.; Carravetta, V. *Surf. Sci.* **1999**, *436*, L691.
(111) Hutchings, G. J.; Willock, D. J. *Top. Catal.* **1998**, *5*.
(112) Bürgi, T.; Atamny, F.; Schlögl, R.; Baiker, A. *J. Phys. Chem. B* **2000**, *104*, 5953.
(113) Bürgi, T.; Atamny, F.; Knop-Gericke, A.; Hävecker, M.; Schedel-Niedrig, T.; Schlögl, R.; Baiker, A. *Catal. Lett.* **2000**, *66*, 109.

3. Theoretical Background

In this chapter, a brief overview of the theoretical techniques used in this thesis will be given. The emphasis will be on the application of these techniques to the problem at hand. Readers who require a more detailed explanation of the techniques involved are directed to one of the standard texts on the subject [1-3]. The chapter starts with an overview of the goal of these types of calculations, followed by a more detailed explanation of the techniques used and how they are applied to molecular and surface systems. Finally, methodology for identification of transition states and reaction pathways will be detailed, before brief discussion regarding other techniques used in the project.

3.1 Potential energy surfaces

When considering a reaction process, it is desirable to be able to determine accurately both the energy and the structure of the various reactants, transition states and products involved in the reaction. The overall 'picture' of the reaction is given by the Potential Energy Surface (PES). The Born-Oppenheimer approximation states that the nuclear and electronic motion can be separated because of the large difference in mass between a nucleus and an electron. The nuclei move very slowly with respect to the electrons, and hence the electrons respond immediately to the motion of the nuclei. Therefore, the potential energy of a system varies as a function of the nuclear coordinates only. If N atoms are present, the PES depends on the $3N$-6 internal or $3N$ Cartesian coordinates present. The variance of the energy as a function of these nuclear coordinates is described by the PES. A typical PES is given in Fig. 3.1.

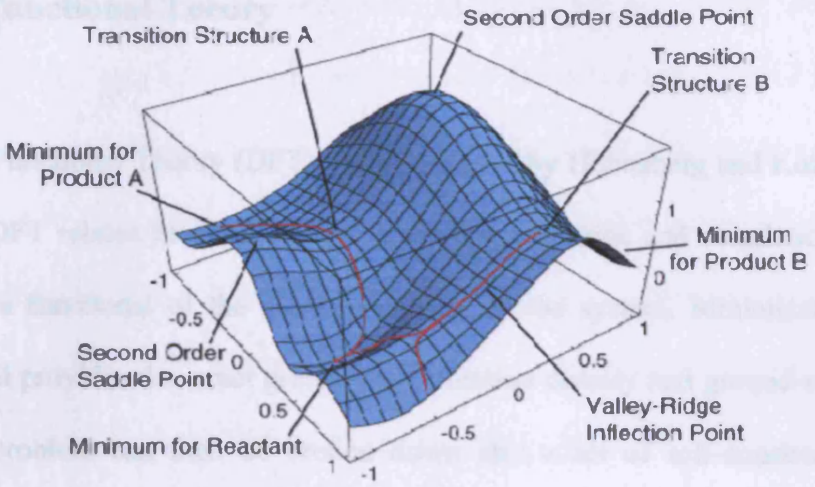

Figure 3.1: Features of a typical PES. Figure obtained from [4]

Fig 3.1 shows a simple reaction process of type R -> P_A + P_B. The reactant and products are both energy minima on the PES; the reactant is a global minimum and the products are local minima in this case. The reaction paths between product and reactants pass through a saddle point, or transition state. The maxima and minima are stationary points on the PES, and can be determined through the 1st and 2nd derivatives of the PES function. The optimisation of the stationary points is performed by calculating the derivatives of the energy with respect to the nuclear coordinates. The forces acting on the atoms are equal to the negative of the gradient; therefore, moving atoms to reduce the forces will lower the energy. The 2nd derivatives can be used to indicate the curvature of the PES and hence to find stationary points and distinguish minima from maxima. Different iterative schemes can be used for the minimisation steps, such as a quasi-Newton (2nd order) method which is more accurate but requires second derivatives, or a conjugate gradients method which is more reliable and only requires gradients. Discussion of the exact difference between these schemes, however, is beyond the scope of this work and further information is available in one of the recommended texts. The next important stage is to be able to accurately describe the energy of the system.

3.2 Density Functional Theory

Density Functional Theory (DFT) was developed by Hohenberg and Kohn [5] and Kohn and Sham [6]. DFT relates the total energy (including exchange and correlation effects) of an electron gas to a functional of the electron density of the system. Minimisation of the total energy functional provides the exact ground-state electron density and ground-state energy. The many electron problem can then be broken down into a set of self-consistent one-electron calculations. The total energy functional is often given the form:

$$E[\rho(r)] = T[\rho(r)] + E_{es}[\rho(r)] + E_{xc}[\rho(r)] + E_{ext}[\rho(r)] \qquad \text{Eqn. 3.1}$$

where $T[\rho(r)]$ is the kinetic energy functional of the non-interacting electrons, $E_{es}[\rho(r)]$ is the electrostatic energy, $E_{xc}[\rho(r)]$ is the exchange-correlation energy and $E_{ext}[\rho(r)]$ is the potential energy in an external field (for example, nuclei of a molecule). A set of wavefunctions ψ_i are needed to represent the density and allow minimisation of the Kohn-Sham energy functional. These are provided by the self-consistent solutions to the Kohn-Sham equations:

$$\left[\frac{-\hbar^2}{2m}\nabla^2 + V_{ion}(r) + V_H(r) + V_{XC}(r)\right]\psi_i(r) = \varepsilon_i\psi_i(r) \qquad \text{Eqn. 3.2}$$

where ψ_i is the wavefunction of electronic state i, ε_i is the Kohn-Sham eigenvalue and V_H is the Hartree potential of the electrons. The interacting many-electron system is mapped onto a system of non-interacting electrons in which each moves in an effective potential due to the other electrons. The exchange-correlation functional is not known exactly so an accurate

representation cannot be made. The Kohn-Sham equations are then solved self-consistently in order for the occupied electron states to generate the charge density to produce an electronic potential that was used to construct the equations. Therefore, a set of eigenequations are obtained which must be solved once an expression for the exchange-correlation can be found.

One common method to describe the exchange and correlation energy is the Local Density Approximation (LDA). The exchange-correlation energy is described using the assumption that the exchange-correlation energy at a point **r** in the electron gas ($E_{XC}(r)$) is equal to the exchange-correlation energy in a homogeneous electron gas having the same density at point **r**, (Eqn. 3.3).

$$E_{XC}[\rho(r)] = \int E_{XC}(r)\rho(r)dr^3 \qquad \text{Eqn. 3.3}$$

Several different parameterisations are commonly used for the exchange-correlation energy of the homogeneous electron gas. The major drawback to this method is the omission of local corrections to the exchange-correlation energy due to inhomogeneities in the electron density.

An extension of the LDA is the generalised gradient approximation (GGA). Gradient corrections are applied to make the exchange-correlation energy a functional of the density. This will not greatly affect local properties (e.g. bond lengths, vibrational frequencies), but will affect global changes in energy. One of the most commonly used GGA exchange-correlation functionals is that developed by Perdew and Wang (PW91), which will be used for the periodic calculations in this work. The exact derivation can be found in reference [7].

Two distinct types of system are discussed in this project: molecular-based systems and solid state systems with a metal surface. The types of methods which have been developed to

deal with these systems are discussed below.

3.2.1 Molecular calculations

A set of basis functions is commonly used to represent the atomic orbitals in a quantum chemistry calculation. The basis functions are not an exact representation of atomic orbitals but approximations. The first representation was made using Slater-type orbitals; these have a cusp at the nucleus and decay exponentially away from it. However, it is difficult to calculate integrals and overlap, so a technique was developed where the Slater-type orbitals can be represented by a linear combination of Gaussian-type orbitals.

The accuracy of a basis set can be increased by adding extra functions, however this will increase the computational expense. One common method is to add polarisation functions; for example, a p-function may be added to the basis set of a hydrogen atom (which would otherwise contain only an s-function). This introduces a degree of asymmetry about the nucleus which is useful for molecular bonding representations. Diffuse functions can also be added, which are slowly decaying Gaussian functions which more accurately represent the tail of the atomic orbital. A commonly used basis set is 6-31G**. This indicates that 6 Gaussians comprise each atomic basis function, and the valence orbitals are represented by two basis functions, one a linear combination of three primitive Gaussians and one just one Gaussian function (a split-valence basis set). Additionally, d and p polarisation functions have been added.

3.2.2. Solid state methods

When considering metal-based surface calculations, it is more convenient to use a planewave rather than a localised, atomic basis set. Planewave basis sets are part of an array of

tools used for surface-based calculations: in effect each basis element is similar to a wave of a set frequency, and the waves are added together to give the electron density in a Fourier series.

Periodic boundary conditions and supercells

A metal surface of a catalyst particle can be considered of vastly larger size when compared to an adsorbate on the surface. The question arises as to how this should be modelled. One common approach is the supercell model. A primitive unit cell of the metal is replicated in three-dimensions until a unit cell of the correct size is obtained: this is a 'supercell'. Periodic Boundary Conditions (PBC) are applied, which inflict a periodicity upon the system; this basic supercell is repeated throughout space. Although only a small number of atoms are within the simulation supercell, the forces they experience are they same is if they were in a bulk metal. A particle exiting through one side of the supercell is replaced by another entering from the opposite side of the supercell. The only major disadvantage to this method is that the system is limited to fluctuations which are smaller than the wavelength of the supercell.

Bloch's theorem

Bloch's theorem states that, for a periodic system, the electronic wavefunction can be split into a cell-periodic part $f_i(r)$ and a wave-like part $\exp[ik \cdot r]$ with a wavevector k.

$$\psi_i(r) = \exp[ik \cdot r] f_i(r) \qquad \text{Eqn. 3.4}$$

The cell-periodic part can be expanded using a basis set, usually a discrete set of planewaves. The planewaves have vectors which are the reciprocal lattice vectors of the

supercell.

$$f_i(r) = \sum_G c_{i,G} \exp[iG \cdot r] \qquad \text{Eqn. 3.5}$$

The reciprocal lattice vectors are given the symbol G, and a Bloch wave coefficient is known as c_i. Each electronic wavefunction is expressed as a sum of planewaves.

$$\psi_i(r) = \sum_G c_{i,k+G} \exp[i(k+G) \cdot r] \qquad \text{Eqn. 3.6}$$

Planewave basis sets

The electronic wavefunction at each k-point, using Bloch's theorem, can be expanded using a discrete set of planewaves as a basis set. The kinetic energy of the planewaves can be described using $\frac{\hbar^2}{2m}|k+G|^2$. The wavevector is proportional to the reciprocal of the wavelength, therefore using $\frac{\hbar^2}{2m}$ [illegible]. The wavevector is proportional to the reciprocal of the wavelength, therefore short-range features require high energy planewaves. Therefore, the planewave basis set can be truncated using a cutoff energy; only planewaves having kinetic energies smaller than this cutoff energy will be included. E_{cut} is decreased until convergence is reached.

k-point sampling

The infinite number of electrons in the solid is represented by an infinite number of special points, called k-points. The k-point density is related to the volume of the supercell. Each k-point is occupied by a finite number of electronic states. Applying Bloch's theorem, a finite number of

electronic wavefunctions at a finite number of k-points (instead of an infinite number of wavefunctions) need to be calculated. k-points which are close together have wavefunctions which are almost identical. Thus, the electronic potential need only be calculated at a finite number of k-points. The k-points are said to be 'sampled'; a sufficient density of k-points must be used to obtain the Fermi surface; total-energy will converge with increasing k-point density.

The most common scheme to sample k-points is the Monkhorst-Pack method [8]. A uniform grid of k-points is generated in reciprocal space. The grid can be symmetrised and weights assigned according to the number of symmetrical images.

3.3 The Pseudopotential Approximation

The pseudopotential approximation is a technique commonly applied to systems containing atoms with a large number of electrons. Even if a planewave basis set is used, a large number of planewaves are needed to adequately describe a rapidly oscillating wavefunction in the core region. It is known that the majority of physical properties and physical behaviour is determined by the valence electrons; therefore, the core electrons are removed and the interaction between core and valence electrons is described by a pseudopotential. This is shown in Fig. 3.2. Outside a set radius, r_c, the pseudoelectron and all electron wavefunctions and potentials are identical; variation only occurs within the core radius. This results in fewer wavefunctions to be calculated, a reduced number of planewaves and smoother valence wavefunctions in the core region.

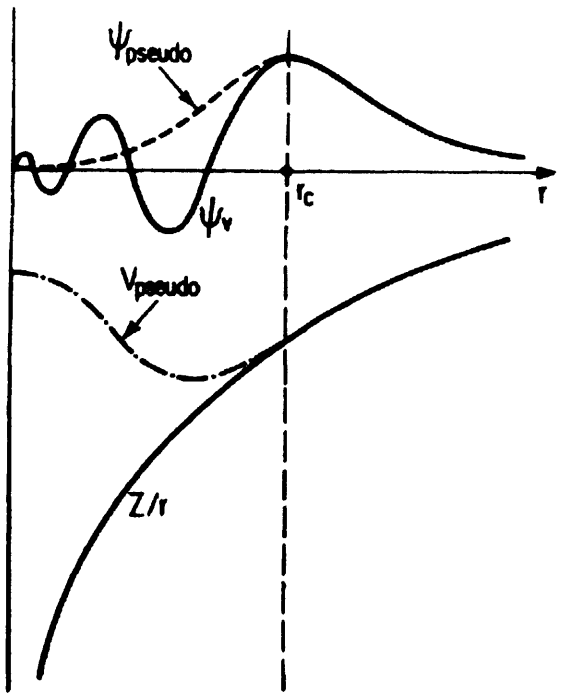

Fig 3.2. All-electron (solid) and pseudoelectron (dashed lines) potentials and wave functions Figure obtained from reference [9].

One special class of pseudopotential are the Projector Augmented Wave (PAW) pseudopotentials [10,11], which are generally more accurate than other types of pseudopotential. PAW potentials typically have smaller cut-off radii and use an exact valence wavefunction in the core region.

3.4 Surface calculations

3.4.1 Definition of surface planes

The majority of calculations to be performed in this thesis are concerned with chemisorption of molecules onto Group 10 metal surfaces. The surfaces used are cut from a crystalline bulk unit cell to form a well-defined crystal plane. The Group 10 metals adopt a *fcc* structure in which each bulk atom has 12 nearest neighbours. The crystal planes are defined using a convention known as the Miller indices. A plane is defined by determining the interception of the plane on each of the x,y,z axes of the system (in terms of the unit cell dimension, a). In the example given in Fig 3.3, the intercept is given as (1, 1, 1). The Miller indices are then simply expressed as the reciprocal values of the intercepts.

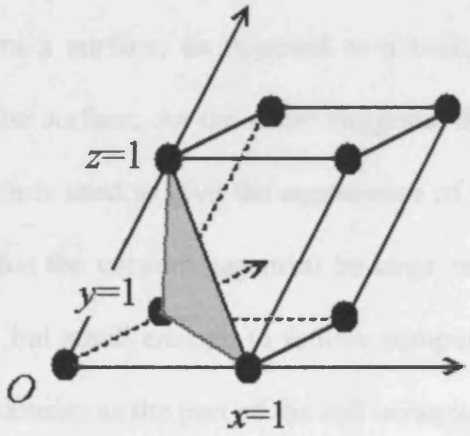

Fig 3.3: Definition of Miller indices for a (111) plane

The most commonly used surface planes in this study are the (100) and (111) planes. Examples of these are given in Fig 3.4. The primitive unit cells shown are the smallest possible repeat unit to generate the surface lattice. For (100) surfaces the surface vectors define a square,

whereas they give a diamond for a (111) surface with angles of 60 ° and 120 °.

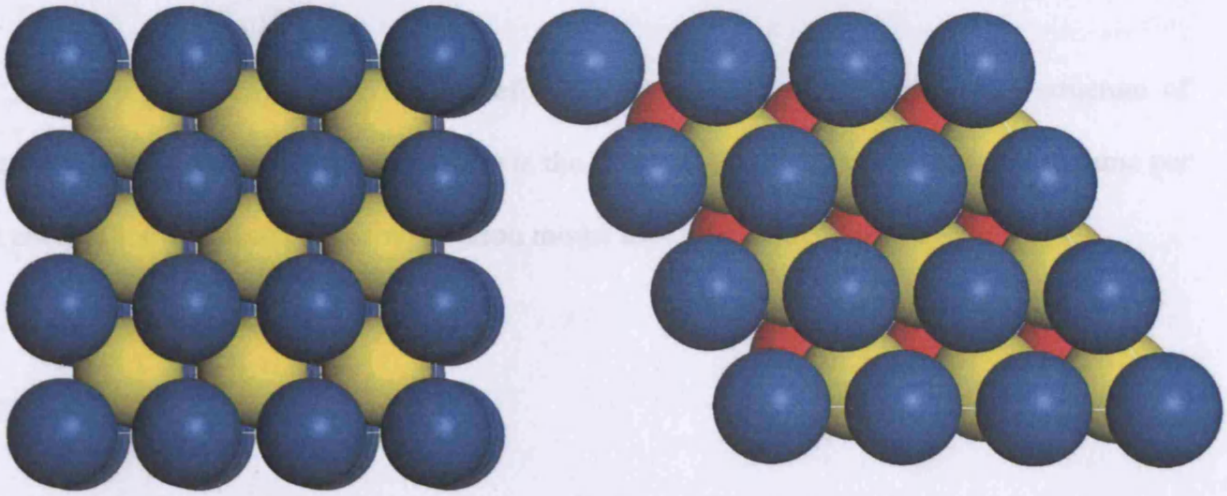

Fig 3.4: (100) (left) and (111 (right) type surfaces. Top layer atoms coloured blue, second layer yellow and third layer red.

The construction of a surface simulation is described in section 3.2.2. Once the bulk unit cell has been cut to expose the desired plane as described above, this is then replicated in the supercell. In order to perform a surface, as opposed to a bulk, calculation a vacuum gap is introduced perpendicular to the surface. As the name suggests, this is simply a vacuum (i.e. an empty area of supercell) which is used to give the appearance of a surface and allow adsorption to occur. It should be noted that the vacuum gap must be large enough to avoid interaction with the base of the image above, but small enough to reduce computational costs (the vacuum gap requires the same planewave density as the part of the cell occupied by the atoms).

The adsorption energy of a system such as this can be defined as:

$$E_{ads} = -(E_{MS} - E_M - E_S) \qquad \text{Eqn. 3.7}$$

where E_{MS} is the calculated energy of the adsorbate adsorbed on the surface, E_M is the energy of the isolated molecule and E_S the energy of the surface with no adsorbate present.

3.4.2 Density of states calculations

The density of states (DOS) is a useful property to compare the electronic structure of related systems. The density of states, g(E) is the number of available states per unit volume per unit energy, and is defined for a free electron model as:

$$g(E) = \frac{1}{2\pi^2}\left(\frac{2m}{\hbar^2}\right)^{3/2} E^{1/2} dE \qquad \text{Eqn. 3.8}$$

It can be seen that g(E) is proportional to $E^{1/2}$ and is independent of the of the system dimension. When the available states are filled with electrons at 0 K, the top of the filled states is the Fermi energy (set as E = 0). An example DOS is given in Fig 3.5.

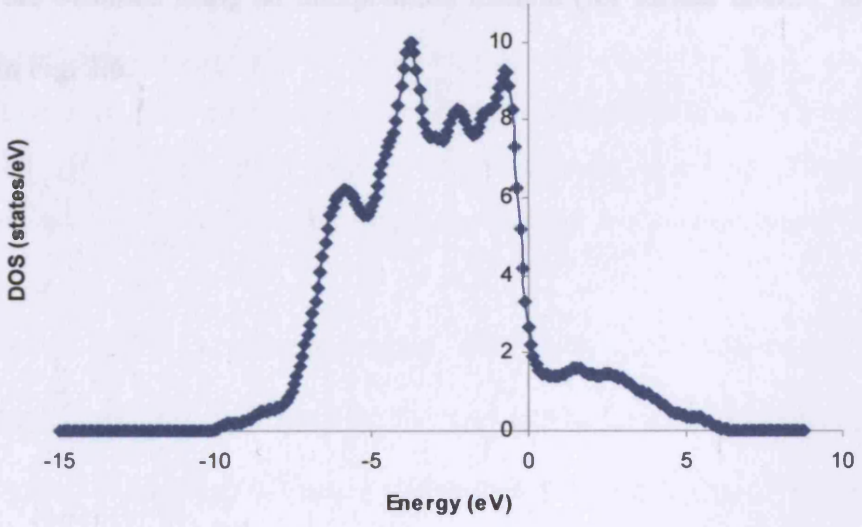

Figure 3.5: DOS plot for a clean Pt (111) surface

3.5 Transition state searching

The goal of this type of study is to be able to find the minimum energy pathway (MEP) between reactants and products and hence the transition state and reaction barrier present; this is often one of the most challenging aspects of a set of calculations. It is difficult to perform a direct transition state search for periodic systems for various reasons, including difficulty in accurately evaluating the Hessian. The most commonly used method for determining MEP, as implemented in the VASP code, is the Nudged Elastic Band (NEB) method.

3.5.1 The Nudged Elastic Band Method

In the Nudged Elastic Band (NEB) method [12], reactant and product geometries obtained from relaxed calculations are used as start and end configurations. A series of images between them are obtained using an interpolation method (for further details, see section 7.2). This is shown in Fig. 3.6.

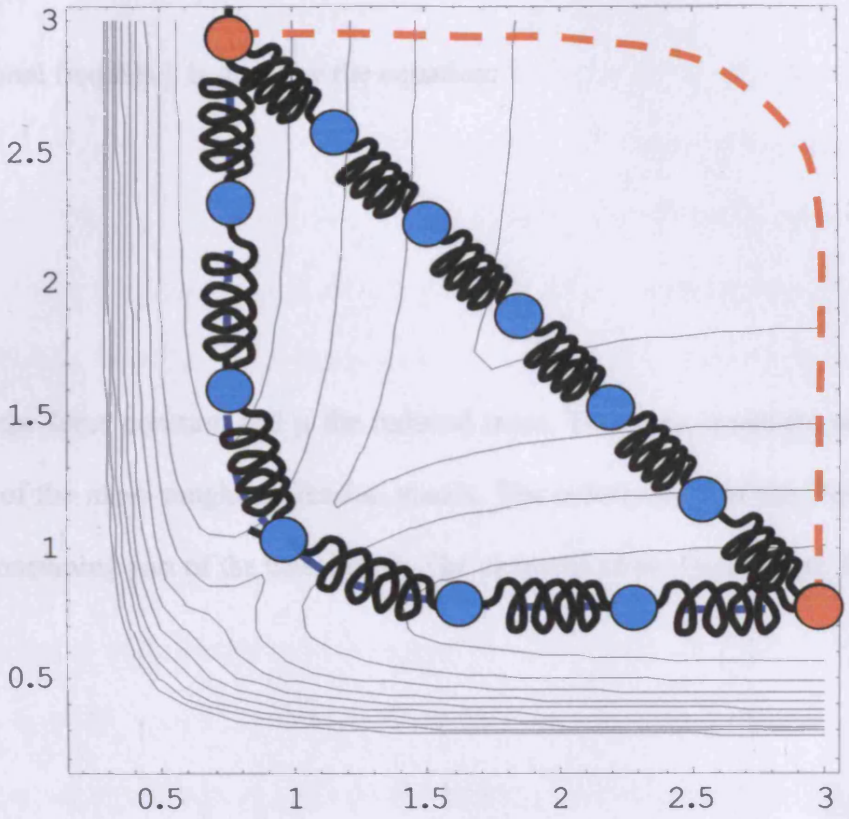

Fig 3.6. The NEB method, applied to a simple system ($H+H_2 \rightarrow H_2+H$). Track in red is via *a 3-membered transition state, central track is a linearly-interpolated elastic band setup and left-most track is the relaxed elastic band outcome (minimum energy pathway). The images are still evenly spaced, and are relaxed only perpendicular to the reaction pathway.*

A constrained minimization is performed, with spring forces applied between images in order to stop them collapsing back to either the start or end image. In the normal elastic band method, this can lead to problems of images sliding towards the minima, or 'corner-cutting' near the transition state. In the NEB method, the perpendicular component of the spring force and parallel component of the true force acting on the image is projected out. The spring constants between images are set to the same value, leading to evenly-spaced images.

3.5.2. Vibrational frequency calculations

The vibrational frequency is given by the equation:

$$\bar{v} = \frac{1}{2\pi c}\sqrt{\frac{k}{\mu}} \qquad \text{Eqn. 3.9}$$

where k is the force constant and μ the reduced mass. The force constants are obtained by diagonalisation of the mass-weighted Hessian matrix. The construction of the Hessian matrix is the most time-consuming part of the calculation. The elements of the Hessian are defined in Eqn. 3.9.

$$H_{i,j} = \frac{\delta^2 E}{\delta x_i \delta x_j} \qquad \text{Eqn. 3.10}$$

For each atomic coordinate, x_i, the coordinate is incremented a small amount, gradients recalculated, then the coordinate is decremented and the gradients recalculated. The second derivative is obtained from the difference of the two derivatives and the step size. The Hessian matrix is then mass-weighted and diagonalisation yields a set of eigenvalues which represent $\sqrt{\frac{k}{\mu}}$, and the vibrational frequencies can hence be calculated.

3.5.3. Eigenvector-following techniques

Using the NEB technique, a good approximation of the transition state and hence reaction barrier can often be found. However, it is possible to refine this further using a technique known as eigenvector following; a full description of the exact methodology used is given in section 7.2. Briefly, a vibrational frequency calculation performed upon the maximum energy structure obtained using the NEB method is performed. The most negative (largest) eigenvector is then taken, and a series of images produced by stepping along the eigenvector in small increments. A transition state should only have one negative frequency, although other low magnitude frequencies may be present due to rotational and translational degrees of freedom. A single-point energy calculation (no optimization performed) is then undertaken at each point. A graph of energy against reaction coordinate along this eigenvector should yield a coincident force minimum and energy maximum. A vibrational frequency calculation is then performed on this point to check that there is only one negative eigenvalue and that the forces are converged to zero within the defined tolerance.

3.6. Other techniques; ONIOM models

The final series of calculations will be performed using a QM/MM approach. In a QM/MM methodology, the system being studied is divided into separate parts. The core part of the system is treated using a high-level quantum mechanical (QM) description, using similar methodology described in the preceding sections on molecular QM. The outer part of the system is treated using molecular mechanics (MM). A force field is used which uses a functional form and set of parameters for each atom type to describe the potential energy of the system and the interaction of the atoms. The functional form and parameters are derived from experimental data and quantum mechanical calculations. The QM/MM scheme used in this study is the ONIOM model; further information can be obtained in references [13-16]. The force field used is the AMBER force field [17].

The QM/MM system used here is simplified compared to those commonly used in other applications. Because of the nature of the system studied, a molecule adsorbed on a surface, there is no need for linker atoms which link the QM and MM system; similarly, there is no need to consider termination of edge of the regions (this is shown in Fig. 3.7). Further details regarding the QM/MM system used here are given in Section 8.4.

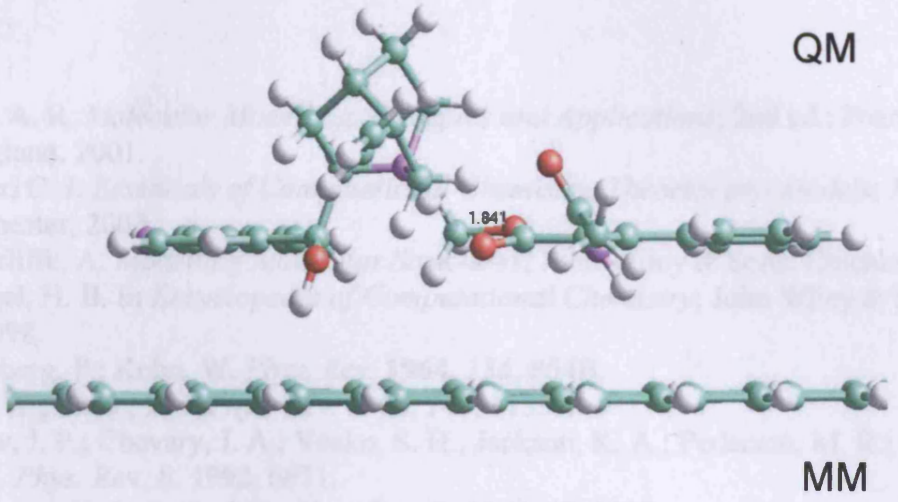

Figure 3.7: Typical QM/MM system setup for an adsorbate and surface

3.7. References

(1) Leach, A. R. *Molecular Modelling, Princples and Applications*; 2nd ed.; Pearson Eduction: England, 2001.
(2) Cramer, C. J. *Essentials of Computational Chemistry, Theories and Models*; John Wiley & Sons: Chichester, 2003.
(3) Hinchcliffe, A. *Modelling Molecular Structures*; John Wiley & Sons: Chichester, 2000.
(4) Schlegel, H. B. In *Encyclopedia of Computational Chemistry*; John Wiley & Sons: Chichester, 1998.
(5) Hohenberg, P.; Kohn, W. *Phys. Rev.* **1964**, *136*, 864B.
(6) Kohn, W.; Sham, L. J. *Phys. Rev.* **1965**, *140*, 1133A.
(7) Perdew, J. P.; Chevary, J. A.; Vosko, S. H.; Jackson, K. A.; Pederson, M. R.; Singh, D. J.; Fiolhais, C. *Phys. Rev. B.* **1992**, 6671.
(8) Monkhorst, H. J.; Pack, J. D. *Phys. Rev. B.* **1976**, *13*, 5188.
(9) Payne, M. C.; Teter, M. P.; Allan, D. C.; Arias, T. A.; Joannopoulos, J. D. *Rev. Mod. Phys.* **1992**, *64*, 1045.
(10) Blöchl, P. E. *Phys. Rev. B.* **1994**, *50*, 17953.
(11) Kresse, G.; Joubert, D. *Phys. Rev. B* **1999**, *59*, 1758.
(12) Mills, G.; Jonsson, H.; Schenter, G. K. *Surf. Sci.* **1995**, *324*, 305.
(13) Maseras, F.; Morokuma, K. *J. Comp. Chem.* **1995**, *16*, 1170.
(14) Matsubara, T.; Sieber, S.; Morokuma, K. *Int. J. Quantum Chem.* **1996**, *60*, 1101.
(15) Svensson, M.; Humbel, S.; Froese, R. D. J.; Matsubara, T.; Sieber, S.; Morokuma, K. *J. Phys. Chem.* **1996**, *100*, 19357.
(16) Svensson, M.; Humbel, S.; Morokuma, K. *J. Chem. Phys.* **1996**, *105*, 3654.
(17) Cornell, W. D.; Cieplak, P.; Bayly, I.; Gould, I. R.; Merz, K. M.; Ferguson, D. M.; Spellmeyer, D. C.; Fox, T.; Caldwell, J. W.; Kollman, P. A. *J. Am. Chem. Soc.* **1996**, *118*, 2309.

4. Methodology

In this chapter, the application of the techniques described in Chapter 3 to the problems at hand will be discussed. All surface-based calculations were performed using the VASP package [1,2].

4.1 Program Description

VASP applies DFT to periodic systems using plane wave basis sets and pseudopotential to replace core electrons. In this case, projector augmented wave (PAW) pseudopotentials [3,4] are used, which are more accurate than the ultrasoft pseudopotential equivalents. The Kohn-Sham equations are self-consistently solved using an iterative matrix diagonalisation method, with Broyden [5] mixing for the charge density. This leads to efficient, accurate calculations for transition metal systems with a complicated band structure. The forces on the atoms are calculated and used to relax the positions of the ions.

The PW91 exchange-correlation functional [6] is used within the Generalized Gradient Approximation (GGA). A basis set of planewaves is used, with the cut-off energy determined as described in section 4.2.2. An iterative matrix diagonalisation scheme is used, allowing direct calculation of vibrational frequencies. The Hamiltonian is determined in direct and reciprocal space, and Fast Fourier Transformations (FFTs) are used to switch between reciprocal and direct spaces, allowing a decrease in the number of planewaves required due to partial diagonalisation.

Broyden-Pulay mixing is used to mix the charge density, allowing linear mixing of previous charge densities from each step. In the calculations performed here, the Methfessel-Paxton method is used to improve the convergence with respect to the k-point sampling for partial occupancies.

The number of k-points in the irreducible part of the Brillouin zone is an important parameter to allow accurate integration in reciprocal space. The k-point sampling grid is calculated using the Monkhorst-Pack method [7] with a given mesh size (Section 4.2.1). The forces are defined as the negative of the derivative of the total energy and the ion position are updated if the forces have not converged to the accuracy required.

4.2 Determination of Calculation Parameters

A number of standard tests are available to determine the calculation parameters which affect the accuracy and efficiency of the calculation. Therefore, before any actual calculations on the systems to be studied are performed, a number of test calculations are undertaken to determine the parameters to be used for the remainder of the study.

4.2.1. k-points

As discussed in section 3.2.2, the density of the k-point grid can be varied to suit the needs of the calculation to be undertaken. The k-point mesh is optimised for the bulk case, and this is then applied to surface calculations. Surface calculations utilise one long lattice vector, and two relatively short lattice vectors in the surface plane. For the long lattice-vector, one division of the k-point mesh is sufficient due to zero band dispersion in this direction (the presence of the vacuum gap); for the two shorter directions, the convergence speed and accuracy with respect to the k-point grid will be approximately the same as in the bulk case. Therefore, the convergence of the bulk energies with respect to the fineness of the k-point grid must be checked; a series of test calculations have been performed and the results are summarised in Fig. 4.1 for Ni, Pd and Pt. These calculations use a fixed cell size but allow relaxation of the ions. The dimension of the unit cell will also affect the required number of k-points; as we are considering reciprocal space calculations, for large cell dimensions it is expected that fewer k-points will be required than for smaller cell sizes.

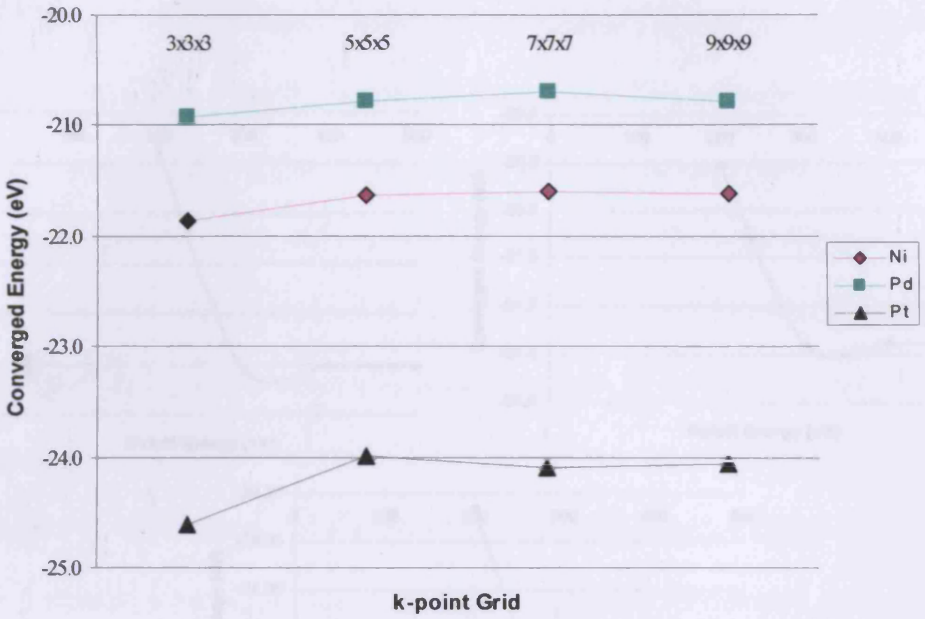

Figure 4.1. Convergence of total system energy with k-point grid for bulk metal unit cells

It can be seen from Fig. 4.1 that a minimum k-point grid density of 5x5x5 is necessary for the total bulk energy to be converged for each of three metals considered here. For a metal surface, this translates to a 5x5x1 k-point grid density.

4.2.2 Energy cut-off

As described in section 3.2.2, the planewave basis set is truncated using an energy cut-off. With the VASP program, the default cut-off energy is set to the maximum ENCUT energy found in the pseudopotential files for each of the atoms (for the PREC=ACCURATE accuracy setting). Approximate values (in eV) for atom types to be used in these calculations are: Ni 270, Pd 250, Pt 230, C 400, O 400, H 250. Therefore, by default, ENCUT will be set to 400 eV. It is necessary to test that this will produce acceptable convergence with respect to basis set size for

the bulk unit cell (Fig. 4.2).

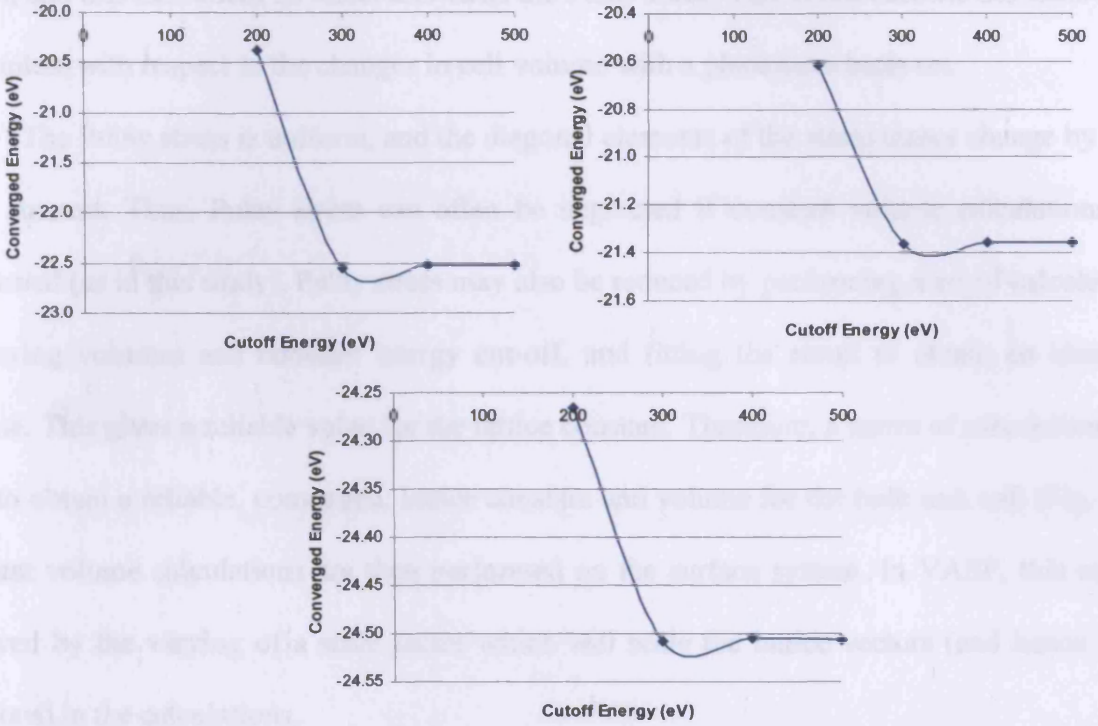

Figure 4.2: Convergence of total system energy with cut-off energy for bulk metal unit cells: Nickel (top left), Palladium (top right) and Platinum (bottom)

Fig. 4.2 shows that using the default value of ENCUT = 400 eV will produce a converged (to within 0.055 eV) result for the bulk unit cell of the metal. This value will be used in all calculations undertaken, and will be set explicitly in order to compare calculations undertaken with different atom types.

4.2.3 Scale Factor

When considering bulk and surface metal systems, the question of Pulay stress must be considered. Hellmann-Feynmann forces are the derivative of total energy with respect to atomic coordinates. Only terms containing explicit derivatives in the Hamilton contribute to this, the

implicit derivatives vanish. However, this only occurs if the ground state charge density and wavefunctions are perfectly converged, which rarely occurs. The implicit derivatives may not vanish, and this introduces an effect known as the Pulay force. This arises because the basis set is incomplete with respect to the changes in cell volume with a planewave basis set.

The Pulay stress is uniform, and the diagonal elements of the stress tensor change by only a set amount. Thus, Pulay stress can often be neglected if constant volume calculations are performed (as in this study). Pulay stress may also be reduced by performing a set of calculations at varying volumes and constant energy cut-off, and fitting the result to obtain an idealised volume. This gives a reliable value for the lattice constant. Therefore, a series of calculations are used to obtain a reliable, converged, lattice constant and volume for the bulk unit cell (Fig. 4.3); constant volume calculations are then performed on the surface system. In VASP, this can be achieved by the varying of a scale factor which will scale the lattice vectors (and hence ionic positions) in the calculations.

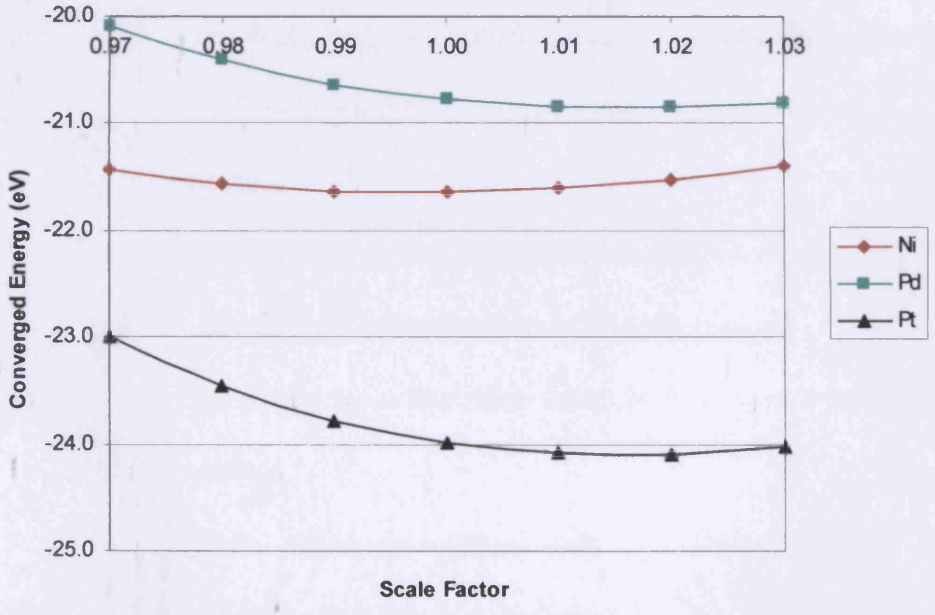

Figure 4.3: Convergence of total system energy with scale factor for bulk metal unit cells

Fitting the data in Fig. 4.3 yields optimal scale factors of Ni 0.997, Pd 1.016 and Pt 1.016. Comparison of these values with experimental data is presented in Table 4.1. It can be seen that for all three metals, good agreement is obtained (less than 2% error is acceptable for accurate calculations).

Metal	Exp. Lattice Constant (Å)	Calc. Lattice Constant (Å)	Error (%)
Ni	3.524	3.514	-0.3
Pd	3.891	3.954	1.6
Pt	3.924	3.986	1.6

Table 4.1: Calculated and experimental lattice constants for Gp 10 metals

4.3 Sample Input Parameters

Once the basic calculation parameters have been defined as described above, a standard input file can be defined. This can be further adapted for differing types of calculation and required accuracies. A brief summary and some commonly used keywords and reasonable settings is given below; more detail is given in the VASP manual [8].

Prec	*Accurate*	Sets default values for calculation parameters which are not specifically defined (e.g. FFT grids, pseudopotential parameters)
ISIF	*2*	Type of calculation to be performed. In this case, keeps cell shape and volume constant and relaxes ion positions. Forces and stresses calculated.
NSW	*100*	The maximum number of ionic optimisation steps to be performed until convergence is abandoned.
IALGO	*48*	The band optimisation algorithm to be used. In this case, a RMM-DIIS-type algorithm which offers faster convergence for large systems
ISMEAR	*2*	Method used to converge partial occupancies with respect to k-point sampling (2^{nd} order Methfessel-Paxton method)
IBRION	*2*	Ionic relaxation algorithm used; in this case, a conjugate gradient method
	5	Finite difference method used to calculate Hessian matrix (for vibrational frequency calculations)
ENCUT	*400*	The cut-off energy, as described in section 4.2.2

NELM	*80*	Maximum number of electronic iterations
NELMIN	*8*	Minimum number of electronic iterations
LORBIT	*10*	Writes DOSCAR-file and spd- and site-projected wavefunction (DOS calculations)
ICHARG	*11*	Reads the charge density from a previous run to construct initial charge density (DOS calculations)

For density of states calculations, first an accurate, static, self-consistent calculation on the system is performed. The output charge density of this is then read in and a non self-consistent calculation is performed and the DOS outputted. For large calculations, the k-points for this second run may be treated independently; runs containing a few, explicitly-defined, k-points are performed and then the results combined into one DOS file.

4.4 References

(1) Kresse, G.; Furthmüller, J. *Phys. Rev. B* **1996**, *54*, 11169.
(2) Kresse, G.; Furthmüller, J. *Comput. Mater. Sci.* **1996**, *6*, 15.
(3) Blöchl, P. E. *Phys. Rev. B.* **1994**, *50*, 17953.
(4) Kresse, G.; Joubert, D. *Phys. Rev. B* **1999**, *59*, 1758.
(5) Johnson, D. D. *Phys. Rev. B* **1988**, *38*, 12807.
(6) Perdew, J. P.; Chevary, J. A.; Vosko, S. H.; Jackson, K. A.; Pederson, M. R.; Singh, D. J.; Fiolhais, C. *Phys. Rev. B.* **1992**, 6671.
(7) Monkhorst, H. J.; Pack, J. D. *Phys. Rev. B.* **1976**, *13*, 5188.
(8) http://cms.mpi.univie.ac.at/vasp/.

5. The adsorption of small molecules onto transition metal surfaces

5.1 Introduction

The goal of this study is to investigate the hydrogenation of ketones over platinum group metals. However, before considering the complete adsorption system, it is useful to study some of the individual components. This will also afford an opportunity to refine the methodology to be used, allowing comparison to well-studied systems in order to validate the results. To begin with, the fate of a hydrogen atom on a metal surface will be considered. This will include adsorption both onto and into the surface. As mentioned previously, we shall extend the study of ketones to include their keto-form and the alternative enol and enolate forms. As these forms may include both C=O and C=C bonds, it is sensible to study simple C=C and C=O bond systems in order to determine their method of adsorption on to the surface. To accomplish this, the adsorption of CO and ethene will be considered. This will then be extended to more complex systems, such as formaldehyde before the adsorption of the simplest ketone, acetone, will be studied.

5.2 The adsorption of hydrogen onto Pt group metal surfaces

5.2.1 Surface Adsorption

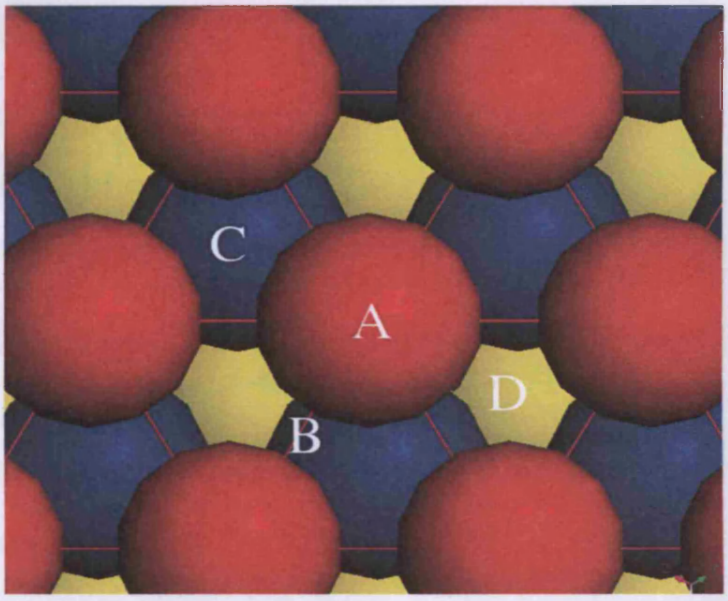

Figure 5.1: The four potential adsorption sites of hydrogen on a (111) surface. A) atop, B) bridge, C) hcp and D) fcc. Top layer atoms are red, second layer blue and third layer yellow.

The adsorption of hydrogen onto the (111) surfaces of Ni, Pd and Pt was modelled using the VASP program and the standard methodology defined earlier (Chapter 4). For each surface, four different adsorption geometries were investigated; atop, bridge, fcc and hcp, which are illustrated in Fig. 5.1. The adsorption energies and geometries of a hydrogen atom on the Ni (111) surface are presented in Table 5.1. The adsorption energies are calculated using half of the energy of the hydrogen molecule as reference data. i.e.

$$E_{ads} = - (E (M+H) - E (M) - \tfrac{1}{2} E (H_2)) \qquad \text{Equation 5.1}$$

where E (M+H) is the energy of the adsorbed system, E (M) is the energy of an isolated metal surface and E (H_2) the energy of the gas-phase hydrogen molecule. This will yield a positive adsorption energy for favourable adsorption.

		atop	bridge	fcc	hcp
E_{ads} (kJ mol^{-1})	Calc.	12.7	53.9	66.3	66.8
	Ref.	10.1	51.4	63.6	63.8
M-H (Å)	Calc.	1.46	1.62, 1.62	1.70, 1.70, 1.70	1.70, 1.70, 1.71
	Ref.	1.47	1.63	1.71	1.71

Table 5.1: Calculated adsorption energies and interatomic distances for H adsorbed on Ni(111) compared to reference data [1]

It can be seen that the calculated adsorption energies are in good agreement with the reference adsorption energies. The reference data [1,2] is from calculations using the same VASP program, but with USPP not the PAW pseudopotentials used here; therefore, they provide a good starting point for comparison of the data. The trend in adsorption energies is the same in the calculated and reference data; calculated adsorption energies were consistently 2-3 kJ mol^{-1} higher than for the reference calculations. The atop adsorption mode is the least strongly bound mode, with the bridge mode approximately 40 kJ mol^{-1} more stable. The two hollow adsorption modes, fcc and hcp, are the most stable adsorption sites, and are indistinguishable from each other within the accuracy of these calculations. Therefore, a trend in adsorption energies is noted; adsorption energy increases with increasing coordination number of the adsorption site. The same trend is seen for M-H bond length; this increases from the singly-bound atop site to the 3-fold hollow site.

		atop	bridge	fcc	hcp
E_{ads} (kJ mol^{-1})	Calc.	9.2	42.1	54.2	50.9
	Ref.	3.1	36.4	49.1	45.2
M-H (Å)	Calc.	1.55	1.72, 1.72	1.82, 1.82, 1.82	1.82, 1.82, 1.82
	Ref.	1.55	1.73	1.82	1.82

Table 5.2: Calculated adsorption energies and bond lengths for H adsorbed on Pd(111) compared to reference data [1]

The calculated adsorption modes for hydrogen on Pd are summarised in Table 5.2 and follow the same trend as seen for Ni. In this case, the calculated adsorption energies using the PAW method are 5-6 kJ mol^{-1} higher than in the USPP case from [1]. The threefold hollow sites are again the most stable, although there is a slight preference (3 kJ mol^{-1}) in favour of the fcc over hcp hollow. The bond lengths are in good agreement with the reference calculations.

		atop	bridge	fcc	hcp
E_{ads} (kJ mol^{-1})	Calc.	53.2	48.3	48.5	48.1
	Ref.	44.8	42.4	43.9	43.2
M-H (Å)	Calc.	1.55	1.76, 1.76	1.71, 1.87, 1.88	1.87, 1.87, 1.87
	Ref.	1.57	1.77	1.88	1.88

Table 5.3: Calculated adsorption energies and bond lengths for H adsorbed on Pt(111) compared to reference data [1]

The calculated adsorption energies for hydrogen on Pt (111) (Table 5.3) exhibit a different trend to those seen for Ni and Pd. The difference between the four different adsorption sites is minimal; the bridge, fcc and hcp sites are isoenergetic within the accuracy of these calculations. The atop site is approximately 5 kJ mol^{-1} more stable than the other sites. These values are in agreement with the previous USPP calculations.

5.2.2 Subsurface adsorption

	Octahedral		Tetrahedral	
	E_{ads} (kJ mol^{-1})	M-H (Å)	E_{ads} (kJ mol^{-1})	M-H (Å)
Ni	4.8	1.74, 1.74, 1.74, 1.85, 1.85, 1.85	-9.6	1.59, 1.59, 1.59, 1.66
Pd	19.1	1.83, 1.83, 1.83, 2.23, 2.24, 2.25	18.7	1.77, 1.77, 1.77, 1.83
Pt	N/A	N/A	-25.0	1.81, 1.82, 1.82, 1.89

Table 5.4: Calculated adsorption energies and bond lengths for H adsorbed between the top most and first subsurface layer of the (111) surface of Ni, Pd and Pt

There are two possible adsorption sites for a hydrogen atom in the first subsurface layer of a (111) surface. The tetrahedral hole (T_d) is formed by a 'triangle' of surface atoms of a fcc site and the metal atom directly below the fcc site (i.e. directly below site C of Fig. 5.1). The octahedral hole (O_h) is formed by a triangle of surface atoms of a hcp site and a triangle of first subsurface layer metal atoms (i.e. directly below site D of Fig. 5.1); the adsorbing atom sits directly above a second layer metal atom. This site is physically larger than the T_d site and involves coordination to six atoms instead of four for the T_d site.

The calculated adsorption energies in Table 5.4 show that for Ni the less constrained O_h site is the more stable adsorption position. For Pt, both adsorption sites are unfavourable; the O_h site is so destabilised that a stable minimum could not be found - the hydrogen atom reemerged onto the surface. The most stable subsurface adsorption sites for hydrogen are found within the Pd (111) surface. The O_h and T_d sites are isoenergetic, and are considerably more stable than any of the Pt and Ni adsorption sites. This is expected: palladium metal is well-known for being able to adsorb quantities of hydrogen. In both O_h and T_d adsorption cases, the hydrogen atom does not sit centrally within the adsorption site. For O_h sites, hydrogen sits closer to one 'triangle' of atoms

than the other; for T_d sites, hydrogen is closer to the three surface atoms than the first layer subsurface metal atom.

5.2.3 Vibrational frequency calculations

	atop	bridge	fcc	hcp
Ni	1987, 352, 336	1316, 1159, 455	1155, 856, 850	1158, 854, 824
Pd	2057, 147, 81	1211, 1137, 306	967, 835, 830	982, 799, 792
Pt	2305, 404, 316	1347, 868, 241	1049, 615, 596	1081, 538, 531

Table 5.5: Calculated vibrational frequencies for a hydrogen atom adsorbed onto Ni, Pd and Pt (111) surfaces. All frequencies in cm^{-1}.

	Octahedral	Tetrahedral
Ni	806, 802, 737	1397, 1384, 1056
Pd	692, 675, 522	1063, 1056, 885
Pt	N/A	964, 958, 793

Table 5.6: Calculated vibrational frequencies for a hydrogen atom adsorbed below the Ni, Pd and Pt (111) surfaces. All frequencies in cm^{-1}

The calculated vibrational frequencies for hydrogen adsorbed onto a (111) metal surface (Table 5.5) and within the surface (Table 5.6) are shown above. As the metal surface is kept fixed and only the adsorbate atom allowed to vibrate, three vibrational frequencies are seen per system (three degrees of freedom). There are trends visible both in terms of the strength of the interaction with the surface and the coordination number of the adsorption site. For example, the calculated vibrational frequency for the atop adsorption site decreases in the order Pt >> Pd > Ni, which is the same trend observed for adsorption energies. Similarly, the trend in coordination number can be seen: atop (1-fold) >> bridge (2-fold) > fcc (3-fold) = hcp (3-fold). However, the key use for the calculated vibrational frequencies will be to correct the adsorption energies using the zero-point correction and note the effect that this has. The zero-point energy is the energy of

the ground vibrational state, which is not normally included in the calculated energy. The correction is made by applying the formula:

$$E_{ZPE} = \frac{1}{2} hc\bar{\nu} \qquad \text{Equation 5.2}$$

Where $\bar{\nu}$ is the wavenumber of the vibration, h is the Planck constant and c the speed of light. In most cases systems will have multiple vibrational states and the corrections for each are additive. It must be noted that when the adsorption energy is corrected, a correction for the zero-point energy of the gas-phase reference hydrogen molecule must also be applied.

	atop (kJ mol^{-1})		*bridge (kJ mol^{-1})*		*fcc (kJ mol^{-1})*		*hcp (kJ mol^{-1})*	
	Unc.	*Corr.*	*Unc.*	*Corr.*	*Unc.*	*Corr.*	*Unc.*	*Corr.*
Ni	*12.7*	*7.4*	*53.9*	*45.5*	*66.3*	*58.7*	*66.8*	*59.4*
Pd	*9.2*	*8.5*	*42.1*	*37.0*	*54.2*	*49.4*	*50.9*	*46.8*
Pt	*53.2*	*43.6*	*48.3*	*45.6*	*48.5*	*48.0*	*48.1*	*49.0*

Table 5.7: Corrected (Corr.) adsorption energies (using the Zero Point Correction (see text)) compared to uncorrected (Unc.) adsorption energies for H adsorption onto Ni, Pd and Pt (111) surfaces.

	Octahedral (kJ mol^{-1})		*Tetrahedral (kJ mol^{-1})*	
	Unc.	*Corr.*	*Unc.*	*Corr.*
Ni	*4.8*	*3.4*	*-9.6*	*-28.9*
Pd	*19.1*	*23.1*	*18.7*	*9.4*
Pt	*N/A*	*N/A*	*-25.0*	*-31.0*

Table 5.8: Corrected (Corr.) adsorption energies (using the Zero Point Correction (see text)) compared to uncorrected (Unc.) adsorption energies for H adsorption below the Ni, Pd and Pt (111) surfaces.

The corrected adsorption energies are compared to the uncorrected energies for adsorption on the (111) surface of Ni, Pd and Pt in Table 5.7 and for subsurface sites in Table

5.8. Considering adsorption onto the (111) surface; although there is a lowering of energy of approximately 5-8 kJ mol^{-1} in most cases, there is no change in the relative ordering of energies or in the trends noted previously. The T_d subsurface adsorption site exhibits the largest variation in adsorption energy, with the adsorption in this site being destabilized by 5-20 kJ mol^{-1} upon correction for zero point energies. Therefore, the affect of zero-point energies on surface adsorption does not have a significant impact on the adsorption energies; although a more marked change is observed for subsurface adsorption, it does not affect the trend in energies observed.

5.3 The adsorption of CO onto Pt group metal surfaces

As discussed in section 2.1.3, the adsorption of CO onto Pt group metal surfaces has been a subject of much study and controversy over the years. For example, the adsorption of CO onto Ni (111) was originally thought to occur onto a bridging site; this was seen theoretically [3] and experimentally [4]. However, recent experimental [5] and theoretical [6] studies have disproved this and a 3-fold hollow site is now preferred (a slight preference for the hcp hollow is suggested). CO on Pd (111) is the least studied system, but a 3-fold hollow adsorption site is also believed to be preferred in this case [7]. The question of adsorption onto Pt (111) is still not settled. Whilst experimental evidence overwhelmingly suggested an atop adsorption [8,9], all reasonable DFT calculations predicted a 3-fold hollow adsorption geometry [10]. Various attempts have tried to predict the correct adsorption site with varying success [11-13].

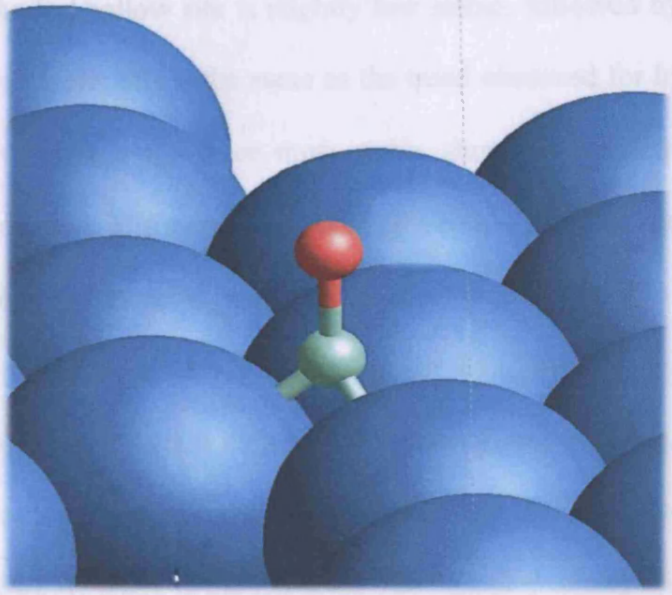

Figure 5.2: The surface adsorption geometry of CO on Pt (111) (fcc site shown).

Calculation of the adsorption site of CO on Pt group metal (111) surfaces was performed using the VASP program and standard methodology. Four adsorption geometries are considered; these are the same as used for the adsorption of hydrogen (Fig. 5.1). An example adsorption site (fcc) is shown in Fig. 5.2. All of the calculated adsorption sites involve the axis of the CO molecule being perpendicular to the plane of the surface.

	E_{ads} (kJ mol^{-1})	M-C (Å)	C-O (Å)	M-C-O (°)
Atop	171.0	1.72	1.16	180
Bridge	202.3	1.87	1.19	138
fcc hollow	210.3	1.95	1.19	133
hcp hollow	216.2	1.95	1.19	133

Table 5.9: Calculated adsorption energies and geometries for CO on Ni (111)

The adsorption energies and geometries for CO on Ni (111) are shown in Table 5.9. The slight preference for hcp adsorption observed here is in agreement with the previous work discussed before. The fcc hollow site is slightly less stable, followed by the bridge site and the atop site is much less stable; this is the same as the trend observed for hydrogen adsorption. The small differentiation between the three most stable sites may explain the early work which favoured bridge adsorption. The most favourable adsorption sites are characterised by longer M-C and C-O bond lengths. In each case, the noted C-O bond lengths were identical; i.e. the adsorption site is symmetrical. The trend in longer M-C bond lengths is the same as that observed for hydrogen; bond length increases with coordination number. The longer C-O bond can be rationalised by a change in the σ/π-electron density, for example through increased M-C back-bonding. The M-C-O angle is the expected 180° for atop adsorption, decreasing to 133° for hollow site adsorption.

	E_{ads} (kJ mol^{-1})	M-C (Å)	C-O (Å)	M-C-O (°)
Atop	132.6	1.87	1.15	180
Bridge	172.9	2.01	1.18	137
fcc hollow	186.6	2.09	1.18	131
hcp hollow	187.7	2.09	1.19	131

Table 5.10: Calculated adsorption energies and geometries for CO on Pd (111)

The adsorption energies for CO on a Pd (111) surface are presented in Table 5.10. The same trend in adsorption energies and bond lengths as seen for adsorption onto Ni is seen here. This is in agreement with the trends observed in the literature. The most favourable adsorption sites are the two hollow sites, which exhibit the longest C-O and M-C bonds.

	E_{ads} (kJ mol^{-1})	M-C (Å)	C-O (Å)	M-C-O (°)
Atop	155.8	1.84	1.16	180
Bridge	173.9	2.02	1.18	137
fcc hollow	170.4	2.12	1.19	131
hcp hollow	173.7	2.12	1.19	131

Table 5.11: Calculated adsorption energies and geometries for CO on Pt (111)

The adsorption energies of CO on Pt (111) (Table 5.11) correlate with those from previous DFT calculations; however, as explained earlier, this is at odds with the experimental evidence. The preferred binding sites here are bridge and hcp hollow, whilst the experimentally favourable atop site is here the least stable by around 15 $kJmol^{-1}$. Therefore, with the exception of the aberration observed for CO on Pt, the adsorption energies found here for the three metal surfaces are in agreement with the experimentally calculated geometries.

5.4 The adsorption of ethene onto Pt surfaces

It is generally accepted that ethene on a Pt (111) surface will adopt a bridging mode between two metal atoms [14,15], although the exact adsorption structure is dependant on temperature and surface coverage. Depending on the exact methodology used, theoretical estimates of the adsorption energy range from 120-150 kJ mol^{-1} [16-18].

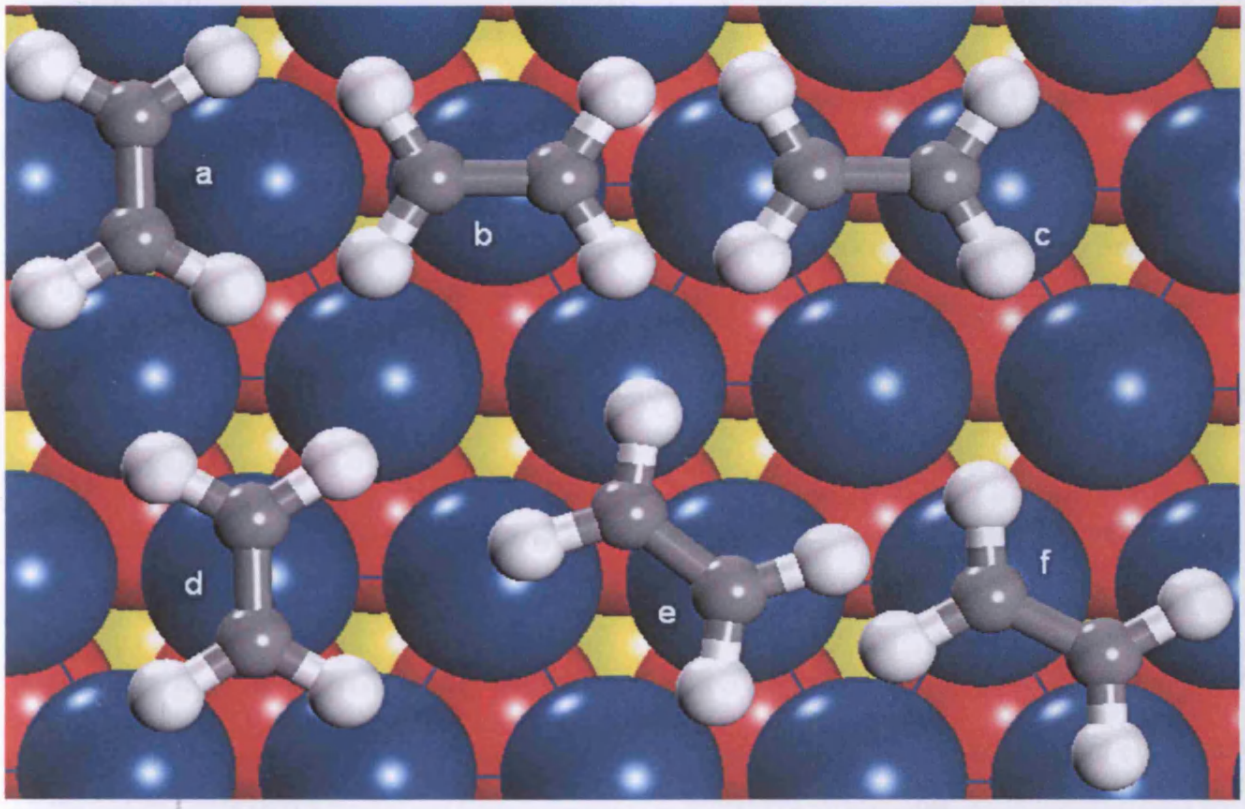

Figure 5.3: The adsorption sites of ethene on a (111) surface, as defined in [18]. a) cross bridge, b) π-bridge, c) di-σ, d) π-hollow, e) fcc hollow, f) hcp hollow

Six potential adsorption sites are usually considered, as described in [18] and shown in Fig. 5.3. These reaction sites will be used in this study for adsorption of ethene onto flat (111)

surfaces. Although slightly different in nature, similar adsorption geometries can be derived for the (100) metal surface.

One important area of research, which is currently being applied to the study of ethene hydrogenation, is the reaction being undertaken at a step-edge on the surface; potentially this may result in a lowering of the reaction barrier. This may occur due to the geometry of the step site; the more open geometry allows better physical separation of the products formed. Such effects have already been noted for other systems; for example, lowering of activation barrier for N_2 dissociation on Ru(0001) steps of 85 kJ mol^{-1} [19], lowering of transition state for CO dissociation on Rh step edges by 120 kJ mol^{-1} [20] and a 30 kJ mol^{-1} increase in adsorption energy for benzene on a Ni (221) step edge [21]. Preliminary experimental electrochemistry work undertaken in the Attard Group in Cardiff suggests that, although not yet defined quantitatively, the adsorption site is dependent on both the nature of the facet as well as the actual surface location. In particular, if a step edge and a (111) terrace are present, adsorption occurs primarily at the step edge. If a step edge and a (100) terrace are present, adsorption occurs indiscriminately.

It is hoped to be able to verify and explain this behaviour using theoretical calculations. Although the VASP program is used with the standard methodology, several changes are needed in this case. In order to perform step calculations, larger supercells are needed to accommodate both the step edge and terrace. The surfaces used here are the (211) ((111) terrace and (100) step edge) containing 60 metal atoms and the (511) ((100) terrace with (111) step edge) containing 120 metal atoms. In order to maintain sufficient cell depth, 5 atomic layers are needed below the step edge, with the bottom two layers being fixed at their bulk positions. In order to maintain

continuity, a 5-layer (2-layer frozen) cell is also used for the flat surface calculations, resulting in an 80-atom ((111), p(4x4)) and 40-atom ((100), c(2x2)) supercell respectively.

5.4.1 The adsorption of ethene onto flat Pt surfaces

Geometry	E_{ads} (kJ mol^{-1})	M-C bond (Å)	C-C bond (Å)
Di-σ	141.5	2.11, 2.11	1.48
π-bridge	124.7	2.17, 2.16	1.42
π-hollow	118.8	2.16, 2.16	1.41
Hollow	113.2	2.16, 2.19	1.41

Table 5.12: Calculated adsorption energies and geometries for ethene on Pt (100)

The adsorption energies for ethene on a flat Pt (100) surface are shown in Table 5.12. The adsorption geometries are presented in Fig. 5.4. The most stable adsorption site, di-σ, involves ethene bridging two metal atoms (a μ_2 (C_1,C_2) mode). This adsorption site shows the adsorbed carbon atoms attaining a more sp^3-like geometry. The angle between the plane of the C-C bond and the plane of two of the hydrogen atoms was found to be 139° for the di-σ mode and 160° for the π-bridge structure. The gas-phase ethene molecule will have an angle of 180° and approximately 125° would be expected for an sp^3-hybridised centre, indicating that the di-σ structure is becoming more sp^3-like than the other structures. This results in a lengthening of the C-C bond to 1.48Å (gas phase ethene is 1.33Å (calculated)); this is closer to the calculated gas-phase ethane C-C bond length (1.53Å). All other adsorption sites are at least 16 kJ mol^{-1} less stable, the next most stable involving a π-bond-type interaction with a metal atom and the C-C bond orientated towards a bridge site (a η^2 (C_1,C_2) mode). The same geometry but with the C-C bond orientated towards a hollow site is slightly less stable, followed by adsorption with the end of the ethene molecule over a hollow site; as this is a (100) surface there is only one type of

hollow site. The remaining adsorption geometry in Fig. 5.3a, cross bridge, resulted in no stable adsorption minimum; immediate desorption occurred upon optimisation.

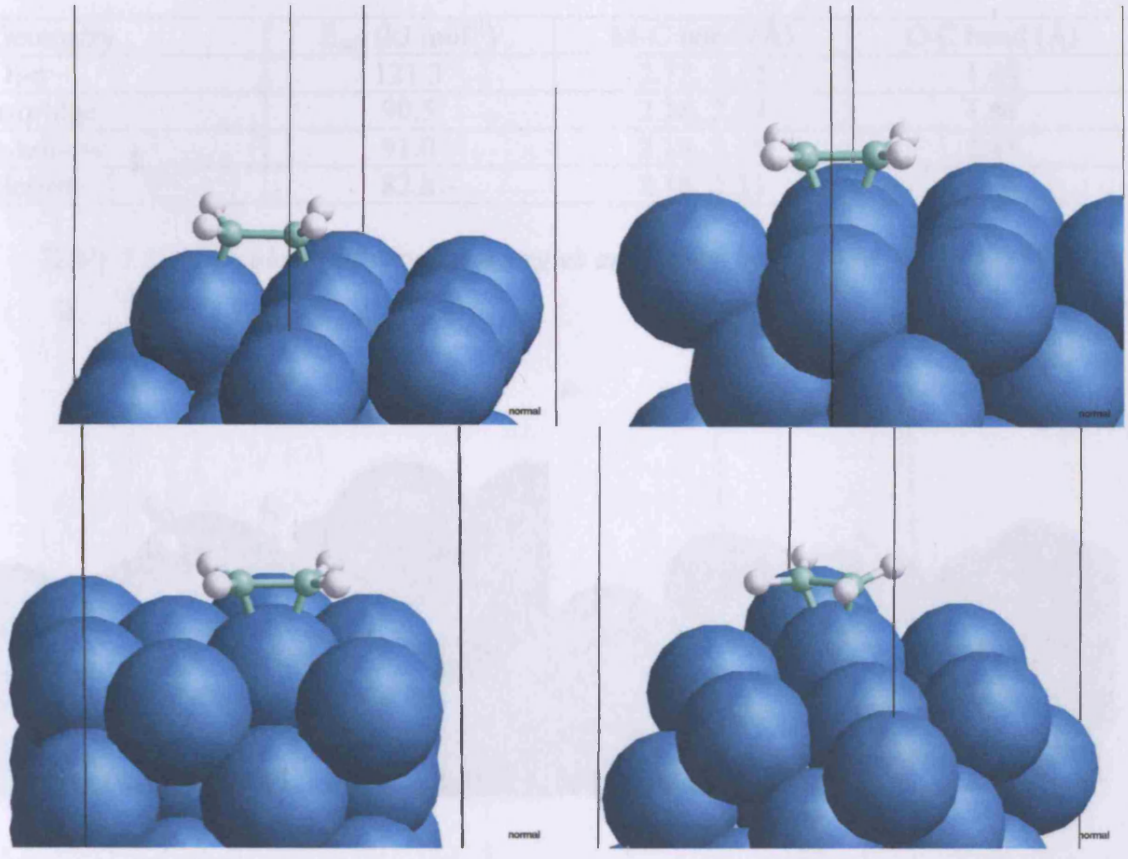

Fig. 5.4.: Adsorption geometries for ethene on Pt (100): Di-σ (top left), π-bridge (top right), π-hollow (bottom left) and hollow (bottom right).

The interaction of ethene with a Pt (111) surface (Table 5.13) shows a similar trend to that observed for the Pt (100) surface. Although the geometries are similar (figure 5.4), apart from a slight lengthening of the M-C bonds, a marked reduction in adsorption energy is observed, with all energies approximately 20-30 kJ mol^{-1} lower than the (100) counterparts. As the geometric differences are minimal, it can be supposed that these differences are mostly electronic in nature. The two hollow sites (fcc and hcp) were found to be identical upon optimisation. These calculated values are in agreement with previous DFT calculations on the

same system [18]. The values for the di-σ mode are 6 $kJmol^{-1}$ lower here than in the previous study, whereas most of the other adsorption modes are 6-8 $kJmol^{-1}$ higher.

Geometry	E_{ads} ($kJ\ mol^{-1}$)	M-C bond (Å)	C-C bond (Å)
Di-σ	121.3	2.12, 2.12	1.49
π-bridge	90.5	2.18, 2.19	1.41
π-hollow	91.0	2.19, 2.19	1.41
Hollow	82.8	2.18, 2.23	1.41

Table 5.13: Calculated adsorption energies and geometries for ethene on Pt (111)

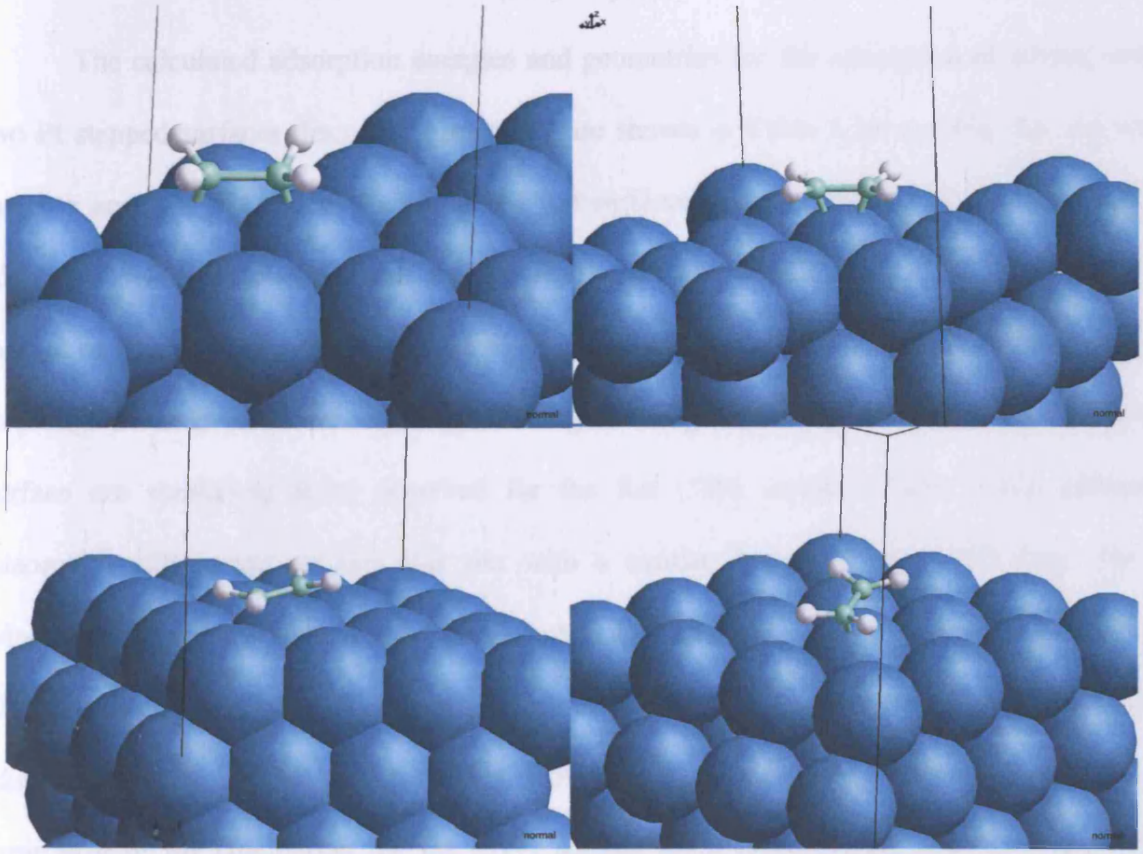

Fig. 5.5.: Adsorption geometries for ethene on Pt (111): Di-σ (top left), π-bridge (top right), π-hollow (bottom left) and hollow (bottom right).

5.4.2 The adsorption of ethene onto stepped Pt surfaces

Geometry	E_{ads} (kJ mol^{-1})	M-C bond (Å)	C-C bond (Å)
Di-σ (211)	142.6	2.11, 2.11	1.48
π-bridge (211)	123.7	2.16, 2.18	1.42
π-hollow (211)	125.2	2.16, 2.18	1.41
π-hollow (tilted) (211)	119.8	2.16, 2.17	1.41
Hollow tilted (211)	113.6	2.18, 2.19	1.41
Di-σ (511)	143.6	2.11, 2.11	1.48

Table 5.14: Calculated adsorption energies and geometries for ethene on stepped Pt (211) and (511) surfaces

The calculated adsorption energies and geometries for the adsorption of ethene onto the two Pt stepped surfaces discussed previously are shown in Table 5.14 and Fig. 5.6. As well as the di-σ and π-bridge modes found for the flat surfaces being transposed to the step edge, two additional sites are found. These are the equivalent of the π-hollow and hollow modes but, instead of being parallel to the surface plane, the C=C bond of the adsorbate is tilted down the step edge towards the lower terrace. The energies and geometries for adsorption onto the (211) surface are similar to those observed for the flat (100) surface (Table 5.12); preferential adsorption still occurs on the di-σ site with a similar energy to the (100) case. The di-σ adsorption occurs on the (511) surface with the same adsorption energies and geometries as the (211) case. For the (100), (111) and (211) case the di-σ is the most stable structure; it seems likely that this is also the case for (511). However this has not been tested directly due to the large size of the calculation for the (511) surface (120 metal atoms) and the computational expense of such calculations; only the di-σ geometry has been calculated. It is expected that this should follow the same trends as observed for the other surfaces.

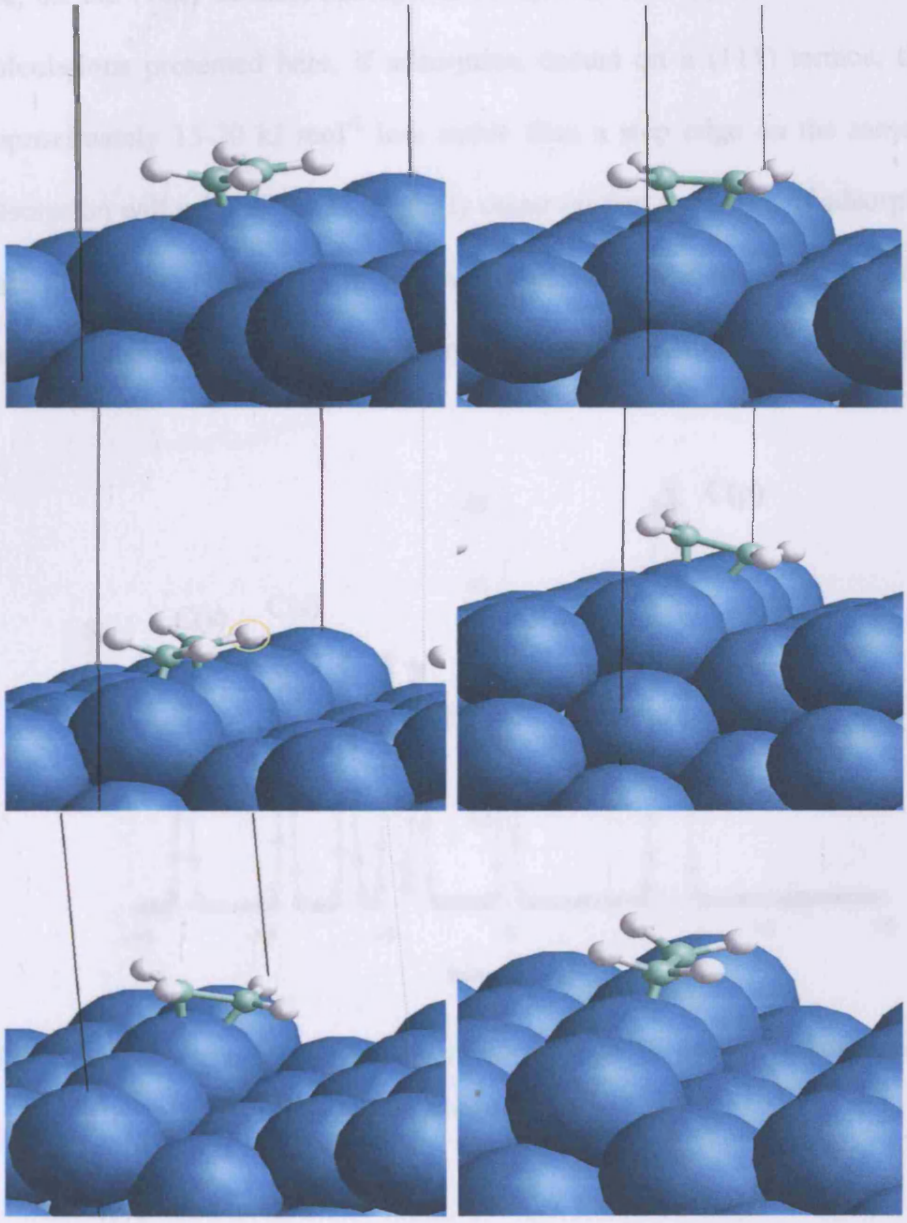

Figure 5.6: Adsorption geometries for ethene on a stepped surface. π-bridge (211) (top left), π -hollow (211) (top right), di-σ (211) (middle left) and π -hollow tilted (211) (middle right), hollow tilted 211 (bottom left) and di-σ (511) (bottom right).

The calculations presented here concur with the experimental electrochemistry evidence. Experimentally, occupation of step sites occurs before the occupation of terrace sites on the

(111) surface; on the (100) surface, adsorption occurs on both types of site at the same time. From the calculations presented here, if adsorption occurs on a (111) terrace, the adsorption energy is approximately 15-20 kJ mol^{-1} less stable than a step edge on the same surface cell; therefore, adsorption will primarily preferentially occur on that step edge. If adsorption occurs on a (100) terrace then there is little discrimination between the two types of adsorption site; terrace and edge have a similar energy and hence adsorption will be distributed over the surface.

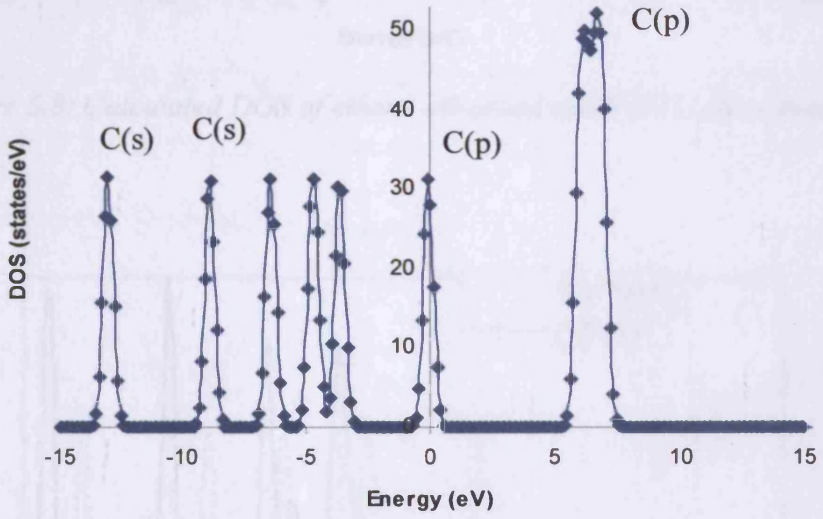

Figure 5.7: Calculated gas-phase DOS of ethene. The origin of the peaks principally due to carbon s- and p-bands are indicated.

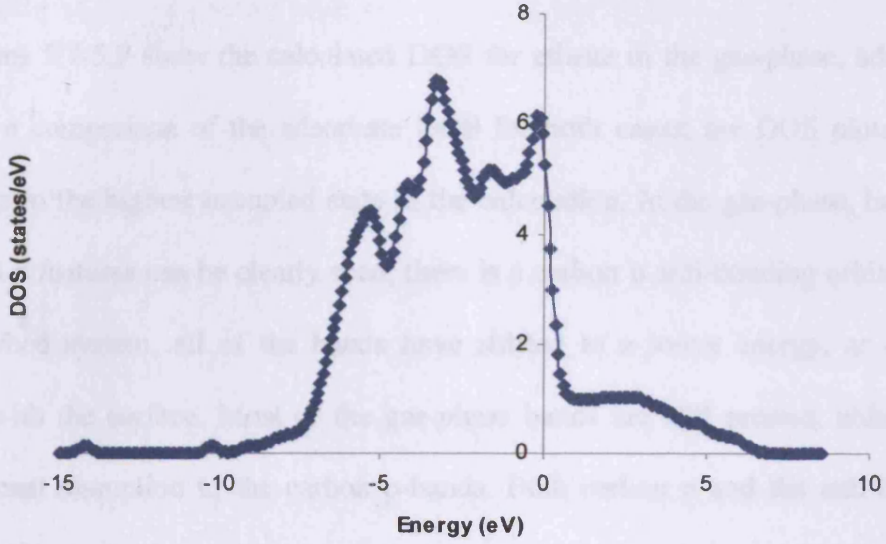

Figure 5.8: Calculated DOS of ethene adsorbed on Pt (111) (di-σ mode).

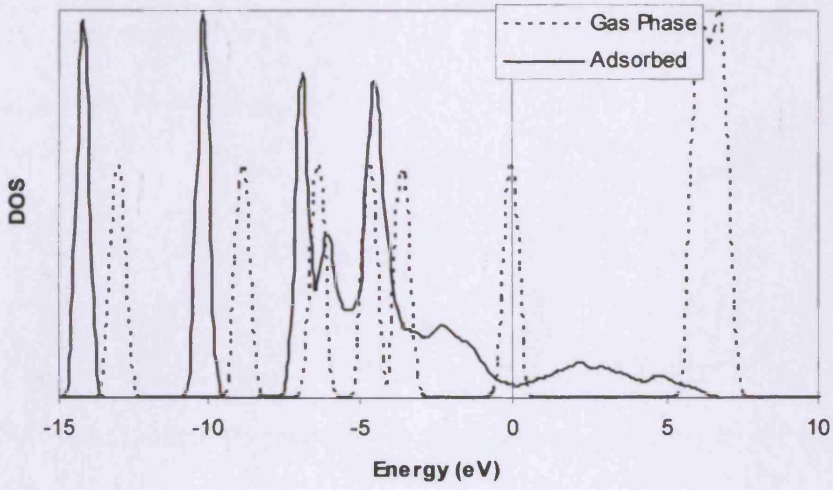

Figure 5.9: Calculated DOS of ethene adsorbed on Pt (111): only adsorbate peaks shown (solid lines) and compared to those depicted in Fig. 5.7 (dashed lines).

Figures 5.7-5.9 show the calculated DOS for ethene in the gas-phase, adsorbed on a Pt surface and a comparison of the adsorbate DOS for both cases; the DOS plots reference the energy origin to the highest occupied state in the calculation. In the gas-phase, bands due to the carbon s and p features can be clearly seen; there is a carbon p anti-bonding orbital also present. In the adsorbed system, all of the bands have shifted to a lower energy, as expected upon interaction with the surface. Most of the gas-phase bands are still present, although there has been significant disruption to the carbon p-bands. Both carbon p and the anti-bonding orbital have lost definition, and have become associated with the metal features as seen on Fig. 5.8. Therefore, there is a lowering in energy upon adsorption, and the metal-adsorbate interaction is primarily through the carbon p-bands.

5.5. The adsorption of formaldehyde onto Pt surfaces

Having considered the adsorption of ethene to Pt metal surfaces, the next logical extension is to consider the adsorption of C-O bonds onto the surface. After CO, the next simplest system which can be studied is formaldehyde, CH_2O. The adsorption of formaldehyde onto a Pt (111) is much simpler than that observed for ethene. Only two adsorption modes are found: with the C-O bond aligned parallel to the surface (*cf.* di-σ bound ethene) and with the C-O bond perpendicular to the surface plane (as observed for a CO molecule). The former mode, similar to the di-σ mode of ethene, will be termed μ_2(C,O) to indicate interaction with two metal atoms *via* the C and O atoms of formaldehyde. The latter mode shall be termed η^1(O) to indicate interaction with one metal atom *via* the formaldehyde oxygen. The μ_2(C,O)-mode is known to be the most stable experimentally (using TPD [22]) and theoretically [23-25] with an adsorption energy of approximately 50-80 kJ mol^{-1}.

	E_{ads} (kJ mol^{-1})	M-C bond (Å)	M-O bond (Å)	C-O bond (Å)	C-H average (Å)
μ_2(C,O)	70.8	2.12	2.03	1.37	1.11
η^1(O)	32.5	-	2.16	1.24	1.10

Table 5.15: Calculated adsorption energies and geometries for formaldehyde adsorbed on a Pt (111) surface

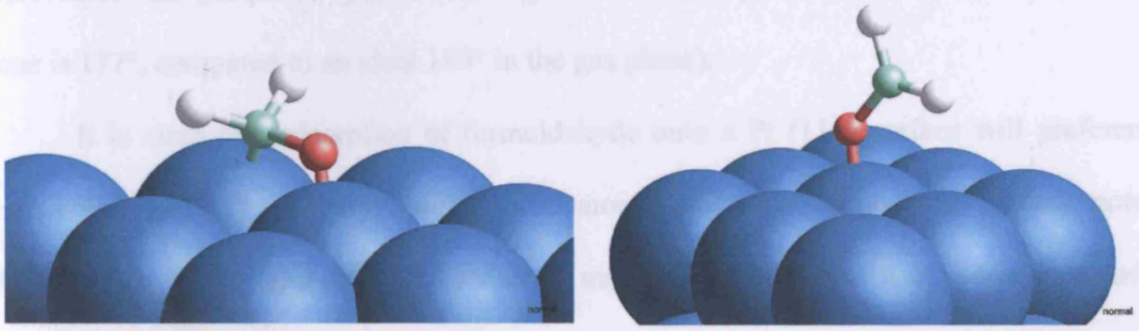

Figure 5.10: Calculated adsorption geometries for formaldehyde on a Pt (111) surface; μ_2(C,O) (left) and η^1(O) (right)

The calculated adsorption energies and geometries for formaldehyde on a Pt (111) surface are shown in Table 5.15 and Fig. 5.10. A clear preference is exhibited for the μ_2(C,O) geometry (an adsorption energy of approximately 71 kJ mol^{-1}), in accordance with previous experimental and theoretical studies. A metal-carbon bond of 2.12Å and a metal-oxygen bond of 2.03Å are seen, and similarity with the di-σ bound mode of ethene can be noted. The C-O bond of the formaldehyde lengthens from 1.21 Å in the gas-phase to 1.37 Å in the surface-bound mode (an increase of 13%); this is the same order of that seen for di-σ ethene (1.33 Å to 1.49 Å, an increase of 12%). The C-H bonds of the terminal CH_2 group bend away from the surface in a similar manner observed for ethene (the angle between the plane of the C-O bond and the CH_2 plane is 135°, compared to 139° for di-σ ethene).

The η^1(O) adsorption mode is less stable on the surface (E_{ads} = 33 kJ mol^{-1}). The optimised structure shows a Pt-O-C angle of approximately 131°. Attempts to locate a structure with a Pt-O-C angle approaching 180° resulted in an unstable structure and desorption from the surface. A single M-O bond of 2.16 Å is observed, and a C-O bond length of 1.24 Å is much closer to the optimised gas phase value. The CH_2 group exhibits planarity to the same extent as

observed for the gas phase species (the angle between the plane of the C-O bond and the CH_2 plane is 177°, compared to an ideal 180° in the gas phase).

It is clear that adsorption of formaldehyde onto a Pt (111) surface will preferentially occur with a μ_2(C,O) geometry, similar to the most favourable di-σ geometry already noted for ethene. A less stable 'end-on' η^1(O) structure may also be seen, but it is necessary to adopt a 'bent' geometry (a decrease in the M-C-O angle) in order for favourable adsorption to occur.

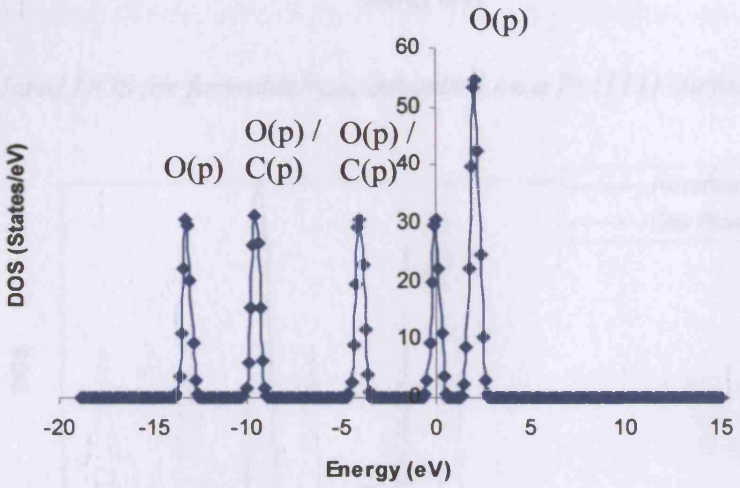

Figure 5.11: Calculated DOS for formaldehyde in the gas-phase. Principle C and O p-bands indicated.

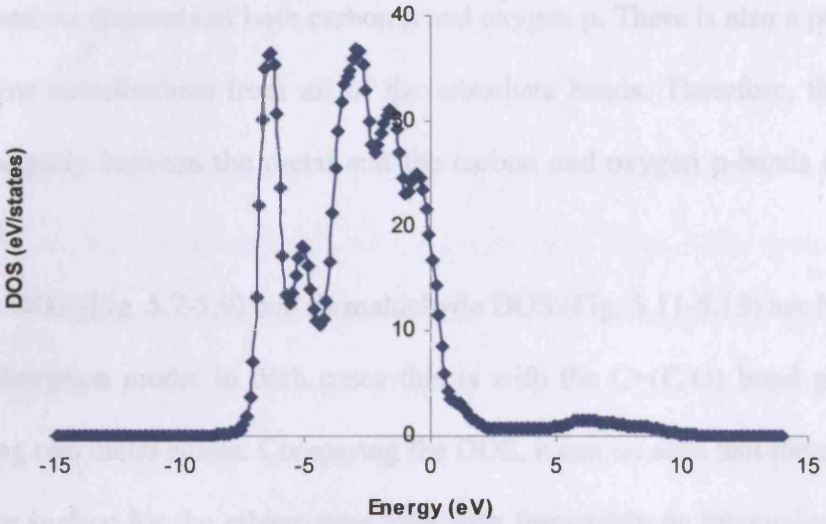

Figure 5.12: Calculated DOS for formaldehyde adsorbed on a Pt (111) surface (μ_2(C,O) mode) .

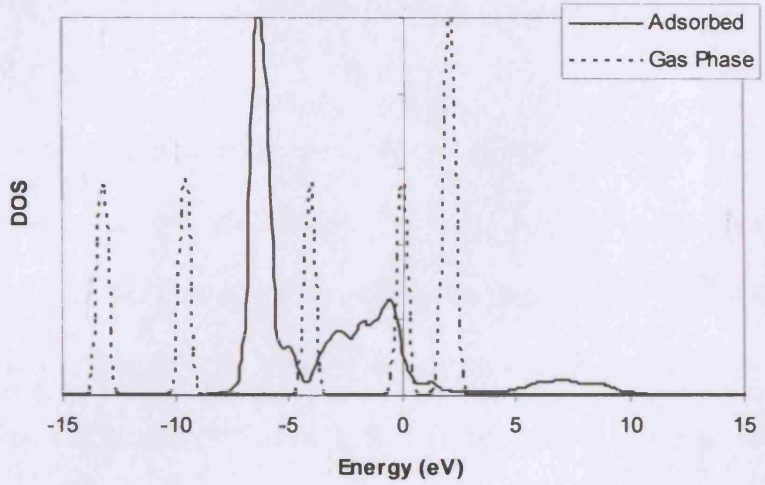

Figure 5.13: Calculated DOS of formladehyde adsorbed on Pt (111): only adsorbate peaks shown (solid lines) and compared to those depicted in Fig. 5.7 (dashed lines).

The DOS for formaldehyde in the gas-phase, adsorbed on a Pt surface and a comparison between the two is shown in Figs. 5.11-5.13. In the gas-phase, the C=O bond of formaldehyde is clearly visible due to two carbon and oxygen p shared-bands. In the adsorbed state, the picture becomes a lot less clear. A lot of the individual bands disappear, and the DOS is dominated by

one band which contains elements of both carbon p and oxygen p. There is also a poorly-defined band which contains contributions from all of the adsorbate bands. Therefore, the interaction appears to be principally between the metal and the carbon and oxygen p-bands (i.e. the C=O bond), as expected.

The ethene DOS (Fig. 5.7-5.9) and formaldehyde DOS (Fig. 5.11-5.13) are both given for the most stable adsorption mode: in both cases this is with the C=(C/O) bond parallel to the surface and bridging two metal atoms. Comparing the DOS, it can be seen that there is a stronger interaction with the surface for the ethene case than with formaldehyde interaction. The ethene bands are shifted to a lower energy upon adsorption, and the principle adsorption bands occur at a lower energy too.

5.6. The adsorption of acetone onto Pt surfaces

Having considered the adsorption of formaldehyde onto Pt surfaces in section 5.5, the next step is to increase the system size from the aldehyde (CH_2O) to the ketone (CH_3COCH_3, acetone). Acetone is perhaps the first molecule which may be considered an acceptable model for the larger systems such as methyl pyruvate since it can undergo keto-enol isomerisation. The two primary adsorption modes of acetone are the same as those noted previously for formaldehyde. Experimental data has shown that a η^1(O) is observed on the surface [26,27] with the η^2(C,O)-mode present as a secondary species at defects and step-edges. These findings have been confirmed using theoretical calculations including Hückel theory [28], cluster modelling [29] and periodic DFT [20].

One recent field of interest is the possible role of enol and enolate forms of ketones in surface catalysis. For example, for methyl pyruvate hydrogenation over Pd, deuteration experiments implied that the hydrogenation was occurring *via* the enol isomer [30]. It was suggested that C=C hydrogenation takes place at a much faster rate than C=O bond hydrogenation and so enolisation may be an important step in this catalysis. RAIRS experiments have also provided evidence for the isolation of an enolate form of acetone of a Ni (111) surface [31].

To this end, calculations will be performed using the standard methodology to investigate the surface stability of the various different ketone, enol and enolate forms on a Pt (111) surface.

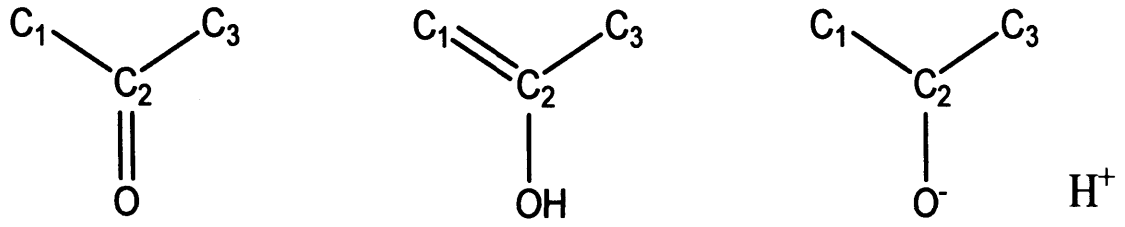

Figure 5.14: The three gas-phase isomers of acetone; ketone (left), enol (middle), enolate ion (right)

Species	Relative Energy (kJ mol^{-1})	C-O (Å)	C-C (Å)	C-C-O Angle (°)	C-C-C Angle (°)
Ketone	0	1.23	1.51	121 / 122	117
Enol	49.2	1.38	1.34	111 / 125	124
Enolate	254.7	1.28	1.39	116 / 126	118

Table 5.16: Calculated relative energies and geometries for acetone in the gas phase

The calculated gas-phase energies and geometries are shown in Table 5.16 and Fig 5.14., which also defines the atom-labelling scheme used in the following discussion. The ketone form, as expected, is considerably more stable than the enol or enolate. The C-O bond length is of the same order noted previously for formaldehyde, and the C-C bond has a value consistent with a C-C single bond. The enol form is 49 kJ mol^{-1} less stable, and a substantial lengthening of the C-O bond and concurrent shortening of the C-C bond can be seen. The enolate ion form is considerably less stable, although some inaccuracy may exist due to the methodology in calculation of the energy of the charged species. As it is not possible to utilise a unit cell with a net charge, a uniform background charge has been introduced to render an overall neutral unit cell for the enolate species in the gas phase; in the adsorbed state, the abstracted proton can be included as a separate surface-bound atom. The C-O and C-C bond lengths are intermediate between the values expected for a single and double bond, indicating that a degree of delocalisation may be present.

5.6.1 Adsorption of keto-acetone

The adsorption of acetone onto a Pt (111) surface has already been found to occur into one of two adsorption modes [26]. One mode exists bonding through the oxygen atom, with the molecular plane perpendicular to the surface. The Pt-O-C angle is distorted away from 180°; one of the CH_3 groups is closer to the surface than the other. This is termed a η^1 (O) adsorption mode. The other adsorption mode has the C-O bond parallel to the surface plane, and the terminal CH_3 groups bent away from the surface. This is termed a $\mu_2(C_2,O)$ adsorption mode, as the C-O bond is bridging two metal atoms. Interpretation of TDS data using RAIRS and HREELS [27] has led to the conclusion that the two desorption peaks seen in the TDS spectrum are due to the η^1 (O) adsorption mode (184 K) and a secondary peak (199 K) is assigned to the $\mu_2(C_2,O)$ mode.

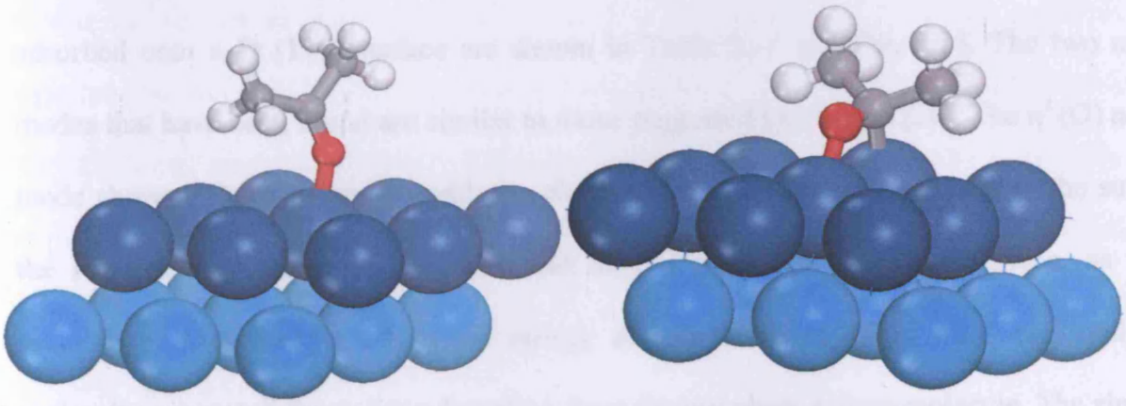

Figure 5.15: Optimised surface structures for acetone adsorbed onto Pt (111) in the η^1 (O) (left) and $\mu_2(C_2,O)$ (right) adsorption modes. Only two surface layers shown for clarity.

Isomer	Geometry	E_{ads} ($kJmol^{-1}$)	C_2-O (Å)	C_1-C_2 (Å)	M-O (Å)	M-C (Å)	CCO (°)	CCCO (°)	C_2XM (°)
Keto	η^1 (O)	39.6	1.25	1.49	2.15	-	123/117	1	133
Keto	$\mu_2(C_2,O)$	20.5	1.38	1.52	2.04	2.18	112/113	47	-
Enol	η^1 (C_1)	60.8	1.33	1.42	-	2.15	122/114	7	96
Enol	$\mu_2(C_1,C_2)$	79.8	1.39	1.51	-	2.09/2.19	116/110	44	-
Enol	$\mu_3(C_1,C_2,O)$	52.5	1.47	1.50	2.29	2.09/2.12	108	52	-
Enolate	$\eta^1(C_1)$ (holl.)	28.9	1.24	1.50	3.16	2.10	121	3	-
Enolate	$\eta^1(C_1)$ (top)	37.8	1.24	1.50	3.06	2.10	121/118	2	-
Enolate	$\mu_2(C_1,O)$	65.2	1.25	1.48	2.12	2.06	115/126	2	-
Enolate	$\mu_3(C_1,C_2,O)$	50.8	1.34	1.50	2.06	2.10/2.31	115/112	37	-

Table 5.17: Calculated minimum energy structures for the adsorption of acetone in the ketone, enol and enolate forms onto Pt (111). Where the angles differ, the first CCO angle refers to C_1C_2O and the second to C_3C_2O. Where more than one M-C bond is present, the first angle given refers to M-C_1 and the second to M-C_2. CCCO refers to the angle between the $C_1C_2C_3$ plane and the C_2-O bond.

The calculated adsorption energies and geometries for acetone in the ketone form adsorbed onto a Pt (111) surface are shown in Table 5.17 and Fig. 5.15. The two adsorption modes that have been found are similar to those suggested previously [26]. The η^1 (O) adsorption mode shows an adsorption site with the plane of the molecule perpendicular to the surface and the Pt-O=C angle distorted to place one methyl group closer to the surface, as predicted previously. A favourable adsorption energy of approximately 40 kJ mol^{-1} is found, and the molecular geometry shows little distortion from the gas phase ketone molecule. The single metal atom coordinating to the acetone is pulled out of the surface because of the molecule-surface interaction by approximately 0.13 Å.

The $\mu_2(C_2,O)$ adsorption mode has a favourable adsorption energy of approximately 21 kJ mol^{-1}. Much more distortion away from the gas phase geometry is notable here. The C-O bond has lengthened to the value for the gas-phase enol isomer, and the CC_2O bond angles have

become consistent with an sp^3 geometry at the central carbon atom of the acetone. The CCCO pseudo-torsion angle has increased from a negligible 1 ° in the η^1 (O) structure to 47 ° here. This is as a result of the distortion of the two terminal methyl groups away from the surface and the plane of the molecule; the planarity of the acetone molecule has been lost. The stronger adsorption energy for the η^1 (O) over the $\mu_2(C_2,O)$ structure here reverses the trend seen for the adsorption of formaldehyde. This indicates a degree of steric interaction between the methyl groups and the surface which is not present in formaldehyde.

These calculated energies are in approximate agreement (within 6 kJ mol^{-1}) with previous theoretical calculations [28]. However, this is at odds with the experimentally observed evidence [27]. The thermal desorption spectra, through vibrational interpretation, indicated that the η^1 (O) mode desorbs at 184 K and the $\mu_2(C_2,O)$ mode at 199 K. Therefore, the $\mu_2(C_2,O)$ mode should be more strongly bound to the surface and a more favourable adsorption energy should be expected; this is the reverse of the trend found here. The secondary peak observed at 199 K may not therefore be due to the $\mu_2(C_2,O)$ mode as suggested previously; in fact, we have confirmed this by vibrational analysis (section 5.6.4). The question therefore remains as to what is observed experimentally. As stated previously, evidence exists for a possible stable enol or enolate ion of acetone adsorbed onto a Pt surface. Therefore, the adsorption of enol and enolate isomers of acetone onto Pt needs to be considered.

5.6.2 Adsorption of enol-acetone

The first question to be addressed when considering the adsorption of acetone in the enol form is the geometry of possible adsorption states. The enol is formed by abstraction of a proton

from one of the methyl groups and subsequent protonation of the ketone oxygen atom. It is obvious at first glance that this makes an adsorption mode analogous to the η^1 (O) mode for the ketone highly unlikely. A M-H-O bond is unlikely to occur and all attempts to isolate such a structure resulted in desorption from the surface; the most favourable interaction energy was found to be -47 kJ mol^{-1}. The removal of the proton has, however, created a CH_2 moiety similar to that discussed previously for ethene.

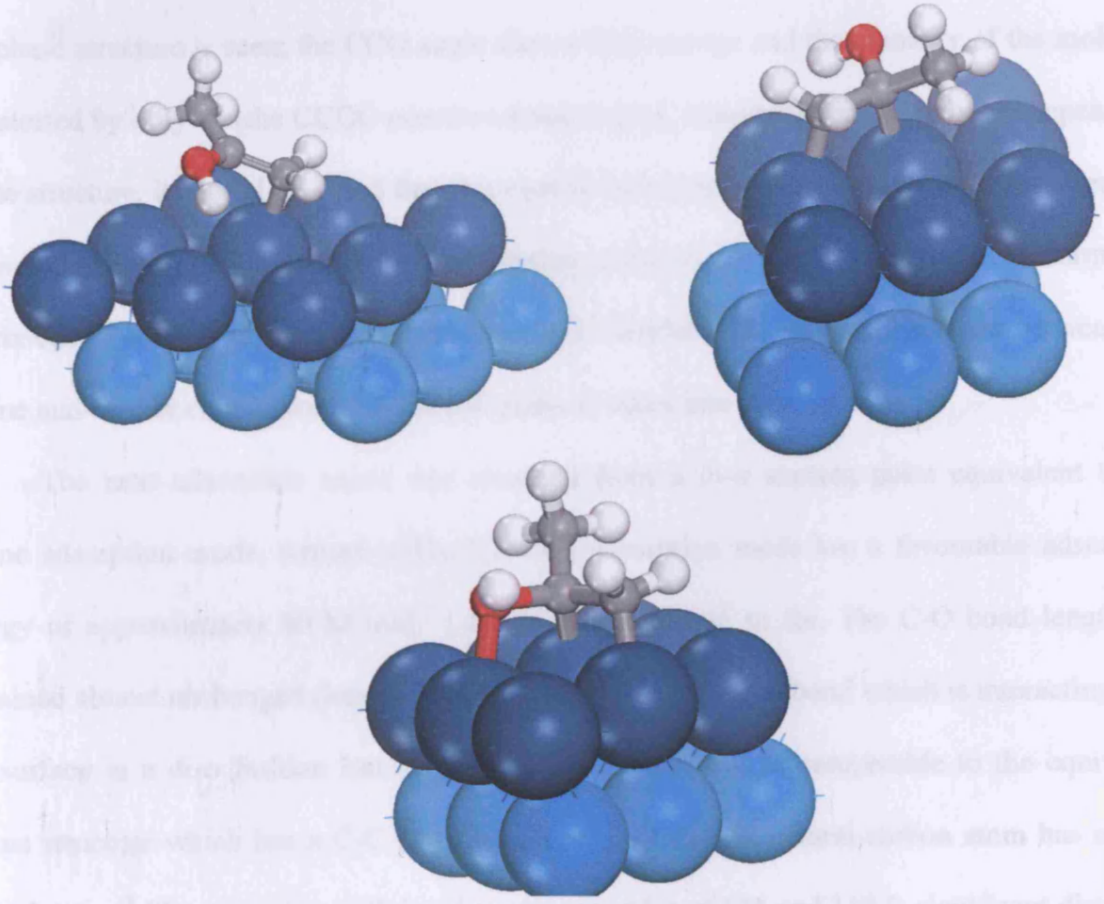

Figure 5.16: Optimised surface structures for acetone (enol form) adsorbed onto Pt (111) in the η^1 (C_1) (top left), μ_2(C_1,C_2) (top right) and μ_3(C_1,C_2,O) (bottom middle) adsorption modes. Only two surface layers shown for clarity.

The first adsorption mode to be considered (Fig. 5.16 and Table 5.17) was obtained from a starting structure similar to the π-bridge mode discussed previously for ethene. However, the more heavily-substituted carbon (with the –OH moiety) moved away from the surface upon relaxation to give a structure with the molecular plane inclined at approximately 30° to the surface plane, designated $\eta^1(C_1)$. A small lengthening of the C=C bond occurs with this interaction with the surface (0.08 Å extension compared to the gas phase) and concurrent shortening of the C-O bond (0.05 Å) is noted. Aside from that, little deviation from the optimal gas-phase structure is seen; the CCO angle shows little change and the planarity of the molecule is distorted by only 7° (the CCCO pseudo-torsion angle). Despite the initial unlikely appearance of the structure, it should be noted that this enol form has an adsorption energy 50% larger than the most stable ketone structure; the adsorption energies for the ketone and enol forms are referenced to the gas-phase ketone structure and therefore the energy difference between the ketone and enol or enolate forms in the gas phase is taken into account.

The next adsorption mode was obtained from a di-σ starting point equivalent to the ethene adsorption mode, termed $\mu_2(C_1,C_2)$. This adsorption mode has a favourable adsorption energy of approximately 80 kJ mol^{-1} ; the highest obtained so far. The C-O bond length has remained almost unchanged (lengthening by 0.01 Å), but the C-C bond which is interacting with the surface in a di-σ fashion has lengthened to 1.51 Å. This is comparable to the equivalent ethene structure which has a C-C bond length of 1.49 Å. The central carbon atom has moved towards an sp^3-like geometry, with bond angles around it of 116 and 110 °; significant distortion of the molecular plane is noted, with a CCCO pseudo-torsion of 44 °. The Pt-C bond lengths are 2.09 Å and 2.19 Å, compared to the Pt-C bond lengths of 2.12 Å for ethene. This shows that

there is a degree of constraint present, most likely due to steric hindrance around the central, heavily substituted, carbon atom.

The final stable adsorption structure to be obtained for the enol form of acetone was also obtained from a di-σ starting point; in this case, a C-O bridged bond. Upon optimisation, the CH_2 moiety also adsorbed on the surface to give an extra point of contact; hence, this is termed $\mu_3(C_1,C_2,O)$. This structure, although having a favourable adsorption energy of 53 kJ mol^{-1}, appears to show a large amount of constraint. The C-C bond length is similar to the $\mu_2(C_1,C_2)$ structure, but the C-O bond length has lengthened to become 1.47 Å. This is significantly longer than the 1.37 Å noted for adsorption of the equivalent formaldehyde structure. The M-O surface bond is 2.29 Å, again significantly longer than the 2.03 Å bond for the formaldehyde structure. The CCO bond angles around the central carbon have reached 108°, close to the 109° expected for tetrahedral symmetry. Therefore, although this structure contains an extra point of contact, this is offset by the distortion needed to obtain this M-O bond compared to the $\mu_2(C_1,C_2)$ structure.

To summarise, no stable structure equivalent to the η^1 (O) structure for the ketone form can be obtained for the enol form. The most stable structure is a $\mu_2(C_1,C_2)$ structure equivalent to a di-σ bonded ethene structure. Alternative structures including a $\eta^1(C_1)$ geometry inclined away from the surface plane and a $\mu_3(C_1,C_2,O)$ structure containing a C-O surface bridged bond both have a higher adsorption energy than any of the optimised ketone geometries.

5.6.3 Adsorption of enolate-acetone

The stable adsorption geometries for the enolate form of acetone are shown in Fig. 5.17.

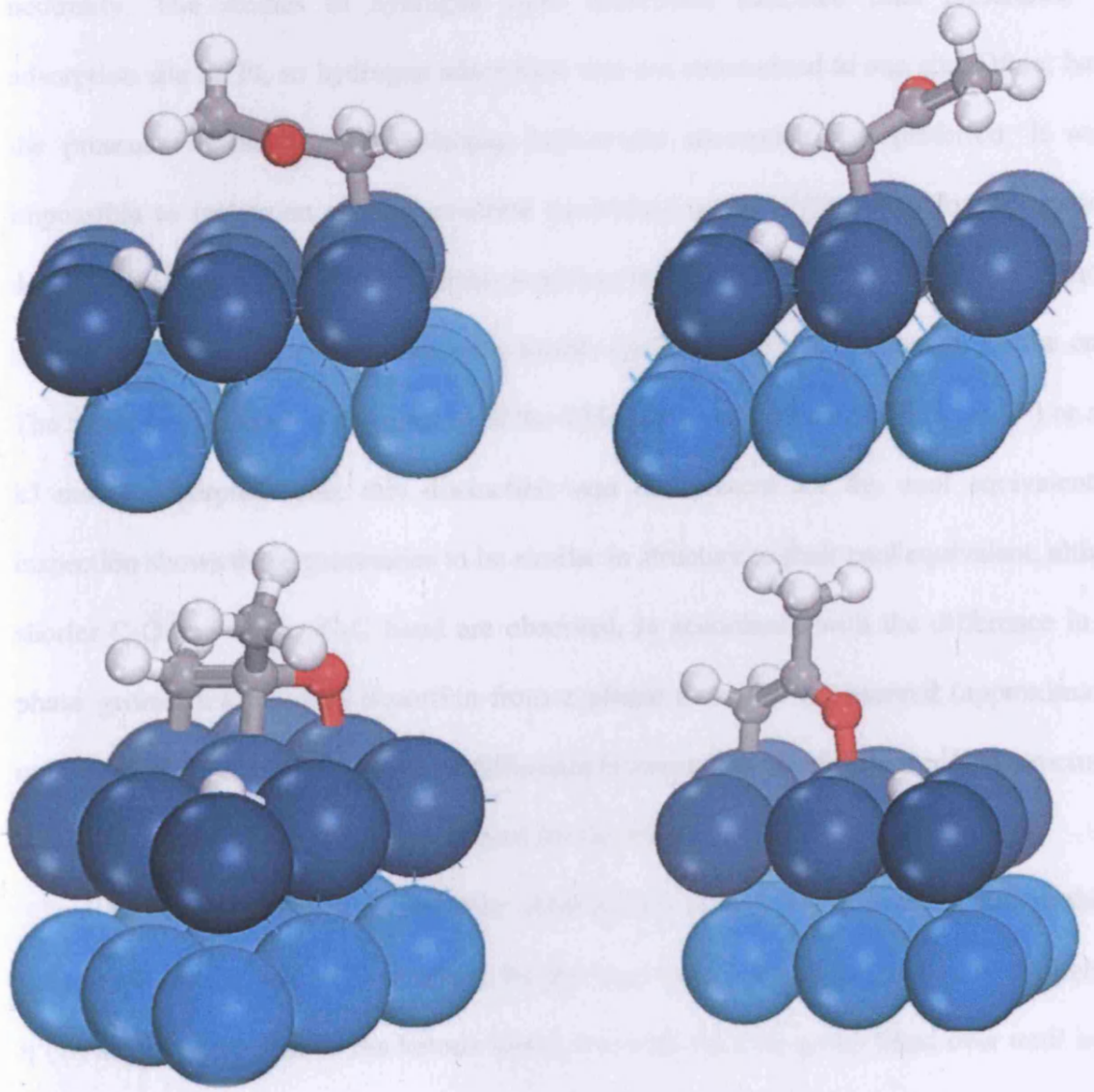

Figure 5.17: Optimised surface structures for acetone (enolate form) adsorbed onto Pt (111) in the η^1 (C_1) (hollow) (top left), η^1 (C_1) (top) (top right), $\mu_3(C_1,C_2,O)$ (bottom left) and $\mu_2(C_1,O)$ (bottom right) adsorption modes. Only two surface layers shown for clarity.

In all of the enolate adsorption structures, the likely fate of the abstracted proton is assumed to be surface adsorption; this maintains atom balance and overall unit cell charge neutrality. The studies of hydrogen atom adsorption indicated little preference between adsorption site on Pt, so hydrogen adsorption was not constrained to one site. Often, because of the presence of the acetone molecule, hollow-site adsorption was preferred. It was again impossible to isolate an enolate structure equivalent to the $\eta^1(O)$ mode for the ketone form; desorption occurred, and the most stable structure had an adsorption energy of -50 kJ mol^{-1}. Two almost equivalent $\eta^1(C_1)$ structures were found, similar to the $\eta^1(C_1)$ structure for the enol form. The structures differed in the placing of the CH_3 group over a hollow (29 kJ mol^{-1}) or a top (38 kJ mol^{-1}) adsorption site; this distinction was not present for the enol equivalent. Visual inspection shows these geometries to be similar in structure to their enol equivalent, although the shorter C-O and longer C-C bond are observed, in accordance with the difference in the gas-phase geometries. Limited distortion from a planar molecule is observed (approximately 2-3° maximum distortion). One potential difference between the two different $\eta^1(C_1)$ structures is the shorter (by 0.1 Å) M-O distance observed for the more stable (top) structure.

The third enolate structure to be obtained was a $\mu_2(C_1,O)$ structure, although this is very different from the $\mu_2(C_1,C_2)$ structure for the enol form. This structure can be thought of as a $\eta^1(O)$ structure (similar to the ketone form), but with the CH_2 group tilted over until interaction with the surface is achieved, in effect creating a M-C-C-O-M bridge. A favourable adsorption energy of 65 kJ mol^{-1} is found. The C-O bond length is close to the gas-phase enolate value, although a lengthening of the C_1-C_2 bond is observed (by 0.09 Å), possibly as a result of the C_1

atom reaching a more sp^3-like geometry. An M-O bond of 2.12 Å and an M-C bond of 2.06 Å indicate that good interaction with the surface is achieved. The distortion from planarity is just 2 °, which may mean that a good degree of the delocalisation seen in the gas phase may be retained here.

The final enolate structure is a $\mu_3(C_1,C_2,O)$ with an adsorption energy of 51 kJ mol^{-1} which, upon inspection, is visually similar to the equivalent enol form structure. The C-O bond length is longer than observed in the gas phase, but still considerably shorter than that observed for the enol structure; the same lengthening of the C-C bond is noted. The M-O interaction is also noticeably shorter here (by 0.23 Å compared to the enol), but one of the M-C interactions is significantly longer (2.10 Å and 2.31 Å) which suggests that there may still be steric constraint here, as seen for the equivalent enol structure.

To conclude, both enol and enolate structures have been identified on a Pt (111) surface with adsorption energies higher than noted for the ketone form of acetone. The adsorption energies of 80 kJ mol^{-1} for the best enol form structure and 65 kJ mol^{-1} for the best enolate structure compared to 40 $kJmol^{-1}$ for the best ketone structure do indicate that they could potentially be responsible for the secondary adsorption peak noted experimentally. However, more evidence is needed to be able to conclusively prove this. In order to attempt to provide this, a vibrational analysis will be undertaken for the most favourable of these structures and then compared to experimental evidence.

5.6.4 Vibrational analysis

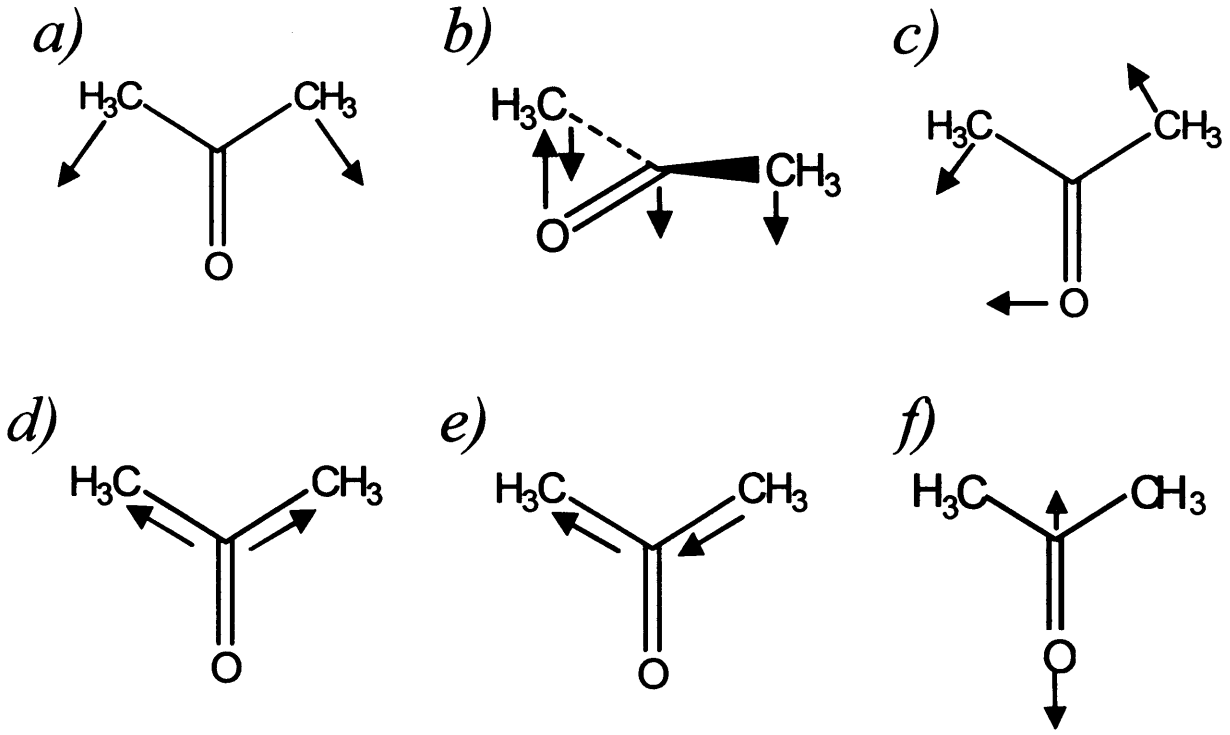

Figure 5.18: The six normal vibrational modes of acetone, as defined in [26]; a) δ(MeCMe) A_1, b) π(CO) B_1, c) δ(CO) B_1, d) υ_s(MeCMe) A_1, e) υ_{as}(MeCMe) B_1 and f) υ (CO) A_1.

In the EELS studies undertaken by Avery [26], six fundamental normal vibrational modes were identified; these are shown in Fig. 5.18. Out of all of the vibrational modes of acetone, these six can be used as a 'fingerprint' to identify the species present. A comparison of the liquid phase IR data from [26] with the gas phase vibrational frequencies calculated here is given in Table 5.18.

	Acetone IR Liquid [26] (cm^{-1})	Acetone gas-phase (calc) (cm^{-1})	Difference between theory and experiment (cm^{-1})
υ (CO) A_1	1710	1737	+27
υ_{as}(MeCMe) B_1	1220	1200	-20
υ_s(MeCMe) A_1	785	775	-10
δ(CO) B_1	530	509	-21
π(CO) B_1	488	461	-27
δ(MeCMe) A_1	390	372	-18

Table 5.18: Comparison of vibrational frequencies of the six key vibrational modes for acetone in the liquid phase (ref [26]) and the calculated values for the gas-phase.

It can be seen from Table 5.18 that there is good correlation between our calculated vibrational frequencies and experimental liquid-phase values. The calculations were performed on a single acetone molecule isolated in a periodic box; this provides a good approximation of gas-phase conditions. The largest discrepancy was found in the *υ (CO) A_1* frequency, which was over-estimated by 27 cm^{-1}. The more complicated bending and stretching modes were typically under-estimated by approximately 20 cm^{-1}. These values are within acceptable variance from the experimental values, and are consistent with other DFT vibrational mode calculations [32].

	η^1(O) (HREELS) (cm^{-1})	$\mu_2(C_2,O)$ (HREELS/RAIRS) (cm^{-1})	η^1(O) (calculated) (cm^{-1})	$\mu_2(C_2,O)$ (calculated) (cm^{-1})
υ (CO) A_1	1640	1610, 1530-1585, 1511	1600	1161
υ_{as}(MeCMe) B_1	1250	1240	1227	1330
υ_s(MeCMe) A_1	810	830	805	775
δ(CO) B_1	570	-	546	445
π(CO) B_1	-	-	470	588
δ (MeCMe) A_1	-	350	387	416

Table 5.19: Comparison of vibrational frequencies of the six key vibrational modes for acetone in the η^1 (O) and $\mu_2(C_2,O)$ adsorption modes for HREELS/RAIRS experimental data [27] and calculated values in this study.

A comparison of the calculated vibrational frequencies calculated in this study and from the experimental HREELS and RAIRS data [27] for both adsorbed ketone forms of acetone is shown in Table 5.19. Comparing the η^1 (O) adsorption mode first, it can be seen that the same trend is observed here as was seen in the gas / liquid phase data. The key υ (CO) adsorption mode is this time underestimated by 40 cm^{-1}, with a calculated vibrational frequency of 1600 cm^{-1}. This decrease of over 100 cm^{-1} is to be expected, as the frequency of the C=O stretch is being damped by the addition of the heavy metal atom. The other key vibrational modes are again approximately 20-25 cm^{-1} lower than the experimental results. Therefore, there is good agreement again between the calculated values and the experimental vibrational frequencies.

The second observed adsorption mode from the HREELS spectrum is more difficult to assign. In this case, the υ (CO) mode is seen to have a frequency of between 1510-1610 cm^{-1} experimentally, but the calculated frequency is just 1161 cm^{-1}. The error between the two sets of data for the rest of the key vibrational modes is of the order of 60-90 cm^{-1}; larger than noted for the η^1 (O) adsorption mode. Whilst some deviation between theory and experiment is inevitable, an error of 400 cm^{-1} is too great to be attributable to experimental error or error in the calculation. If the second adsorption peak is, in fact, due to a $\mu_2(C_2,O)$ adsorption mode as depicted in Fig. 5.9, then the υ (CO) frequency would be expected to show a dramatic decrease from the gas-phase value because of interaction with the two metal atoms. The C=O bond will obtain a more single bond-like character, as evinced by the increase in bond length noted in Table 5.17. As an example, the C-O single bond stretching frequency in the gas-phase for methyl pyruvate (where carbon atoms are attached to each end of the C-O bond) is in the region of 1190-1220 cm^{-1} [33]. Given the expectation that the gas-phase values should decrease upon adsorption onto the surface, a value of 1510-1610 cm^{-1} for a $\mu_2(C_2,O)$ adsorption mode is

unfeasibly high. Therefore, the secondary peak observed in the HREELS spectrum may be an experimental artefact or may represent a different surface species. In light of the data in Table 5.17 suggesting the possible viability of the enol or enolate form of acetone being a stable surface species, the next step is to perform a vibrational analysis of these species and compare the data to the experimental values.

	Ketone $\mu_2(C_2,O)$ (HREELS/RAIRS) (cm^{-1})	Ketone $\mu_2(C_2,O)$ (calculated) (cm^{-1})	Enol $\mu_2(C_1,C_2)$ (calculated) (cm^{-1})	Enolate $\mu_2(C_1,O)$ (calculated) (cm^{-1})
υ (CO) A_1	1610, 1530-1585, 1511	1161	1223	1574
υ_{as}(MeCMe) B_1	1240	1330	1212	1228
υ_s(MeCMe) A_1	830	775	794	835
δ(CO) B_1	-	445	455	580
π(CO) B_1	-	588	595	602
δ (MeCMe) A_1	350	416	365	383

Table 5.20: Comparison of vibrational frequencies of the six key vibrational modes for acetone in the $\mu_2(C_2,O)$ adsorption mode from HREELS/RAIRS experimental data [27] and calculated values for the $\mu_2(C_2,O)$ ketone mode and the most stable enol and enolate structures in this study.

Table 5.20 shows the comparison of the secondary HREELS species and the most favourable of the enol and enolate species listed in Table 5.17. The ketone $\mu_2(C_2,O)$ adsorption mode is included for comparison. It is immediately apparent that the enol structure contains a C-O-H singly-bonded moiety and hence the expected C-O stretch will occur at too low a frequency. Although there is approximate agreement with the other key vibrational modes, the υ (CO) A_1 mode is of cardinal significance and hence the enol structure can be discounted. Much better agreement is found when the most stable enolate structure is considered. The υ (CO) A_1 vibrational frequency is within the range observed experimentally and good agreement is seen

with the other vibrational modes. It is therefore feasible that this enolate mode could be responsible for the secondary adsorption peak observed experimentally.

In conclusion, the adsorption energies and geometries for acetone on the Pt (111) surface have been calculated. A η^1 (O) adsorption mode, where the plane of the acetone molecule is adsorbed perpendicular to the surface is found to be more stable than a $\mu_2(C_2,O)$ adsorption mode (where the plane of the molecule is parallel to the surface). This is contradictory to the observed experimental evidence where the opposite trend is expected; therefore, it is hypothesised that the more stable surface species observed experimentally may be as a result of the adsorption of acetone in the enol or enolate ion form. Calculations using the enol and enolate forms show a strong, favourable adsorption energy can be obtained; the most stable species are $\mu_2(C_1,C_2)$ (enol, involving a bridged C=C bond similar to ethene) and $\mu_2(C_1,O)$ (enolate, similar to a tilted η^1 (O) adsorption mode). Vibrational analysis confirms that there is good agreement between theory and experiment for the ketone η^1 (O) mode, but poor agreement for the $\mu_2(C_2,O)$ mode. Further vibrational analysis of the enol and enolate modes finds acceptable agreement for the enolate $\mu_2(C_1,O)$ mode; this is suggested as a possible candidate for the second surface-adsorbed species observed experimentally.

5.7 Conclusions

The adsorption of a number of smaller molecules onto group 10 transition metal surfaces has been successfully studied. This includes hydrogen (Ni, Pd and Pt (111) surfaces), CO (Ni, Pd and Pt (111) surfaces), ethene (Pt (111), (211) and (511) surfaces), formaldehyde (Pt (111)) and acetone (Pt (111)). Where necessary, vibrational frequency analysis has been performed in order to explain the observed adsorption energies and geometries.

The calculated adsorption energies for hydrogen are in agreement with previous theoretical studies. For both Ni and Pd (111) surfaces the fcc and hcp hollow sites are the most favourable adsorption sites by approximately 13 kJ mol^{-1}. For the Pt (111) surface there is little to distinguish all of the adsorption sites, with only a slight preference (4 kJ mol^{-1}) for adsorption in the top site. Subsurface hydrogen adsorption is only favourable for Ni (a small 5 kJ mol^{-1} adsorption energy) and Pd (the adsorption energy is larger, but still 30-35 kJ mol^{-1} less than the most stable surface adsorption site. This is in agreement with the perceived ability of Pd to adsorb hydrogen within the surface, as observed experimentally.

CO also adsorbs preferentially in the fcc and hcp hollow sites for Ni, Pd and Pt; however it should be noted that the last case, although in agreement with previous theoretical calculations, is at odds with experimental evidence where top adsorption is observed. Formaldehyde adsorbs preferentially with the C=O bond parallel to the metal surface (38 kJ mol^{-1} more stable than 'end-on' adsorption); this is possible due to the low steric interaction between the surface and the hydrogen atoms of the formaldehyde molecule.

On both (100) and (111) surfaces ethene was found to preferentially adsorb in a di-σ adsorption mode (with the C=C bond bridging two metal atoms), but this adsorption mode is

approximately 20 kJ mol^{-1} more stable for the adsorption onto the (100) surface. Adsorption onto a step-edge (of either (100) or (111) type) was of approximately the same energy as adsorption onto the (100) flat surface. This suggests that adsorption onto the step-edge may be more favourable than adsorption onto a flat surface in certain cases, and that the most favourable part of the interaction is between the ethene π and metal d-orbitals, as observed with DOS calculations.

The adsorption of acetone was found to be more stable in the enol (by 40 kJ mol^{-1}) and enolate forms (25 kJ mol^{-1}) than in the ketone form. This may have important implications when studying larger molecules and the relative surface stabilities of the enol and enolate forms may be crucial. This effect may be observed for methyl- and ethyl-pyruvate and this will affect whether C=C or C=O bonds are presented for hydrogenation, which will in turn affect the enantioselectivity or even the sense of the product that is formed. DOS calculations suggest that it is the ethene C=C bond which interacts more strongly than the formaldehyde C=O bond. Understanding of the surface adsorption and preferred adsorption structures of formaldehyde, ethene and acetone in particular will enable calculations using bigger systems, such as methyl pyruvate, to be set up and performed.

5.8 References

(1) Watson, G. W.; Wells, R. P. K.; Willock, D. J.; Hutchings, G. J. *J. Phys. Chem. B.* **2001**, *105*, 4889.
(2) Watson, G. W.; Wells, R. P. K.; Willock, D. J.; Hutchings, G. J. *Chem. Comm.* **2000**, *8*, 705.
(3) Bertolini, J. C.; Dalmai-Imelik, G.; Rousseau, J. *Surf. Sci.* **1977**, *68*, 539.
(4) Persson, B. N. J.; Ryberg, R. *Phys. Rev. Lett.* **1985**, *54*, 2119.
(5) Davis, R.; Woodruff, D. P.; Hofmann, P.; Schaff, O.; Fernandez, V.; Schindler, K.-M.; Fritzsche, V.; Bradshaw, A. M. *J. Phys.: Condens. Matter* **1996**, *8*, 1367.
(6) Hammer, B.; Hansen, L. B.; Nørskov, J. K. *Phys. Rev. B* **1999**, *59*, 7413.
(7) Sautet, P.; Rose, M. K.; Dunphy, J. C.; Behler, S.; Salmeron, M. *Surf. Sci.* **2000**, *453*, 25.
(8) Blackman, G. S.; Xu, M.-L.; Ogletree, D. F.; Van Hove, M. A.; Somorjai, G. *Phys. Rev. Lett.* **1988**, *61*, 2352.
(9) Pederson, M. O.; Bocquet, M. L.; Sautet, P.; Laegsgaard, E.; Stensgaard, I.; Besenbacher, F. *Chem. Phys. Lett.* **1999**, *299*, 403.
(10) Feibelman, P. J.; Hammer, B.; Nørskov, J. K.; Wagner, F.; Scheffler, M.; Stumpf, R.; Watwe, R.; Dumesic, J. *J. Phys. Chem. B* **2001**, *105*, 4018.
(11) Olsen, R. A.; Philipsen, P. H. T.; Baerends, E. J. *J. Chem. Phys.* **2003**, *119*, 4522.
(12) Orita, H.; Itoh, N.; Inada, Y. *Chem. Phys. Lett.* **2004**, *384*, 271.
(13) Gil, A.; Clotet, A.; Ricart, J. M.; Kresse, G.; García-Hernández, M.; Rösch, N.; Sautet, P. *Surf. Sci.* **2003**, *530*, 71.
(14) Sheppard, N. *J. Electron Spectrosc. Relat. Phenom.* **1986**, *38*, 175.
(15) Cremer, P. S.; Stanners, C.; Niemantsverdriet, J. W.; Shen, Y. R.; Somorjai, G. A. *Surf. Sci.* **1995**, *328*, 111.
(16) Shen, J.; Hill, J. M.; Watwe, R. M.; Spiewak, B. E.; Dumesic, J. A. *J. Phys. Chem. B* **1999**, *103*, 3923.
(17) Ge, Q.; King, D. A. *J. Chem. Phys.* **1999**, *110*, 4699.
(18) Watson, G. W.; Wells, R. P. K.; Willock, D. J.; Hutchings, G. J. *J. Phys. Chem. B* **2000**, *104*, 6439.
(19) Dahl, S.; Logadottir, A.; Egeberg, R. C.; Larsen, J. H.; Chorkendorff, I.; Törnqvist, E.; Nørskov, J. K. *Phys. Rev. Lett.* **1999**, *83*.
(20) Alcalá, R.; Greeley, J.; Mavrikakis, M.; Dumesic, J. A. *J. Chem. Phys.* **2002**, *116*, 8973.
(21) Site, L. S.; Sebastiani, D. *Phys. Rev. B* **2004**, *70*, 115401.
(22) Abbas, N. M.; Madix, R. J. *Appl. Surf. Sci.* **1981**, *7*, 241.
(23) Hirschl, R.; Eichler, A.; Hafner, J. *J. Catal.* **2004**, *226*, 273.
(24) Desai, S. K.; Neurock, M.; Kourtakis, K. *J. Phys. Chem. B* **2002**, *106*, 2559.
(25) Delbecq, F.; Sautet, P. *Langmuir* **1993**, *9*, 197.
(26) Avery, N. R. *Surf. Sci. Lett.* **1983**, *125*, 70.
(27) Vannice, M. A.; Erley, W.; Ibach, H. *Surf. Sci.* **1991**, *254*, 1.
(28) Delbecq, F.; Sautet, P. *Surf. Sci.* **1993**, *295*, 353.
(29) Vargas, A.; Bürgi, T.; Baiker, A. *J. Catal.* **2004**, *222*, 439.
(30) Hall, T. J.; Johnston, P.; Vermeer, W. A. H.; Watson, S. R.; Wells, P. B. *Stud. Surf. Sci. Catal.* **1996**, *101*, 221.
(31) Sim, W.-S.; Li, T.-C.; Yang, P.-X.; Yeo, B.-S. *J. Am. Chem. Soc.* **2002**, *124*, 4970.

(32) Loffreda, D.; Jugnet, Y.; Delbecq, F.; Bertolini, J. C.; Sautet, P. *J. Phys. Chem. B* **2004**, *108*, 9085.
(33) Wimshurst, J. K.; Horwood, J. F. *Aust. J. Chem.* **1971**, *24*, 1183.

6. The adsorption of methyl pyruvate onto a platinum surface

6.1 Introduction

The next stage after studying the adsorption of smaller molecules such as acetone is to expand the study to the larger molecules which are of more interest catalytically. The adsorption of methyl pyruvate to a metal surface has not been very widely studied theoretically, and the experimentally-predicted structures are not yet definitive.

Experimentally, STM, NEXAFS, XPS and TPR have been used to study the interaction of methyl pyruvate with the Pt (111) surface[1]. In this study, the observed adsorption geometry of methyl pyruvate was found to depend strongly on the presence of hydrogen in this system. In the presence of hydrogen, monomeric methyl pyruvate molecules were found adsorbed on the surface; whereas, in the absence of hydrogen, polymer chains were formed. The C=O bonds of the adsorbed methyl pyruvate molecule were inclined at 64° to the surface; although no exact adsorption structure can be elucidated from this, it implies that the main interaction between the adsorbate and surface is *via* the lone pairs of the pyruvate oxygen atoms. The adsorption of ethyl pyruvate has also been studied using XANES[2] and a hydrogen dependency was again found. When hydrogen is present, the angle between the plane of the molecule and the surface decreases to approximately 58°, compared to 72° when hydrogen is not present. Clear evidence is presented that two different adsorption modes are present on the surface at the same time.

Therefore, pDFT calculations will be used in order to attempt to rationalise the adsorption mode of MP onto Pt (100) and (111) surfaces, two of the most commonly investigated systems. The VASP package will be used along with the standard protocols as described in the methodology section. For both (100) and (111) surface calculations a five-layer slab of metal atoms, with the lower two layers frozen at the bulk positions, was sufficient to obtain accurate results. The (100) metal slab super-cell is square with dimensions $a = b = 11.9589$ Å, $c =$

17.9726 Å (including vacuum gap); the (111) super-cell is hexagonal with dimensions $a = b =$ 11.2750 Å, c = 19.2060 Å. The (111) surface contains 80 Pt atoms, whilst (100) surface contains 90 Pt atoms.

It order to compare the calculated structures with experimental data, the tilt angle of the molecule on the surface, (φ), was measured using the mean plane of the non-hydrogen adsorbate atoms and that of the surface layer Pt atoms. These planes were calculated using an optimisation procedure in which the constants, a-d, in the general equation of the plane,

$$ax + by + cz + d = 0 \qquad \text{Eqn. 6.1}$$

were variables and the sum of squares of distances of the atom set to the plane was the minimised variable. The normal to the planes produced is the vector (a,b,c) and so the angle between this and the normal to the surface plane was used to find the angle between the planes.

The angles made between the C-O bonds and the surface were calculated as simply the Pt-O-C angle, based on the surface Pt atom to which the C-O bond is co-ordinated using the dot product between C-O and O-Pt vectors. In some cases the C-O vector is pointing away from the surface and this results in a negative angle.

6.2 Gas phase calculations

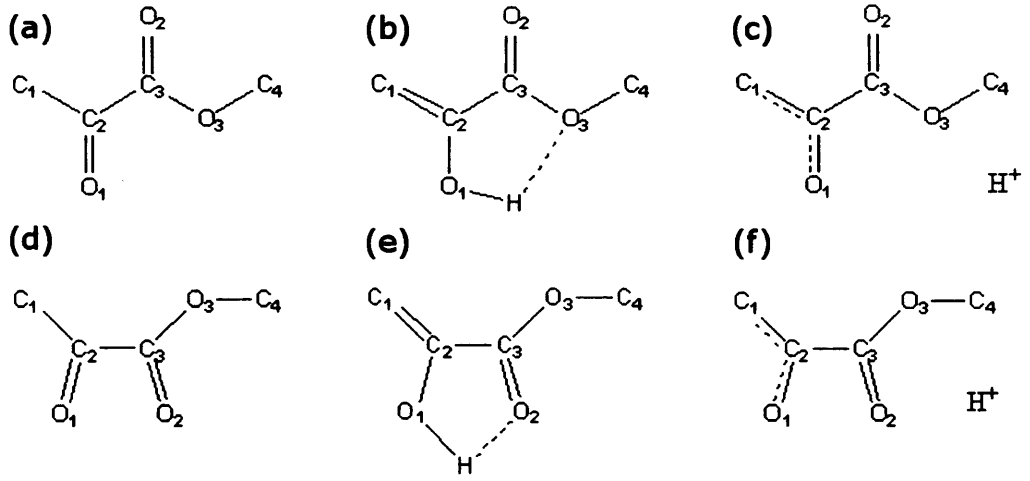

Fig. 6.1. The six molecular species used in this study; (a) s-trans-keto isomer, (b) s-trans-enol isomer, (c) s-trans-enolate ion isomer, (d) s-cis-keto isomer, (e) s-cis-enol isomer and (f) s-cis-enolate ion isomer. H atoms on carbon omitted for clarity.

In an analogous fashion to our analysis of the adsorption modes of acetone onto a platinum (111) surface (section 5.6), we have considered the adsorption of methyl pyruvate to the metal surface in different conformations for each possible isomer. Firstly, both *s-trans*- (Fig. 6.1a) and *s-cis*-forms (Fig. 6.1d) of methyl pyruvate in the keto configuration are studied; we have then extended the study to include the enol (Fig. 6.1b and 6.1e for *s-trans* and *s-cis* respectively) and enolate (Fig. 6.1c and 6.1f) isomers in both *s-trans* and *s-cis* configurations, giving a total of six surface species to be studied. The enolate isomer is produced by removal of the hydroxylic proton of the enol to form an anionic species; in surface calculations this proton can be assumed to bind to the surface but in gas-phase reference calculations this is not possible. The creation of an isolated proton gives a very large estimate for the heat of formation of this species. Under normal circumstances the O-H bond would break in the presence of some other species able to receive the proton and so stabilise the product. A more reasonable solution to calculate the relative energy is not to explicitly include the abstracted proton and instead introduce a net positive background charge in order to maintain a neutrally-charged unit cell (the same methodology which is used for the acetone study described previously). As a result, the calculated gas phase energy for this system may not be as reliable as for the *enol*- and *keto*-

forms.

Structure	Isomer	E_{rel}[a] (kJ mol^{-1})	C_2-O_1 (Å)	C_3-O_2 (Å)	C_1-C_2 (Å)	C_2-C_3 (Å)
Ketone	*s-cis*	4.3	1.22	1.21	1.51	1.56
	s-trans	0.0	1.22	1.22	1.50	1.55
Enol	*s-cis*	6.7	1.36	1.23	1.34	1.49
	s-trans	18.1	1.37	1.22	1.34	1.49
Enolate	*s-cis*	187.9	1.27	1.22	1.39	1.54
	s-trans	185.6	1.28	1.23	1.39	1.55

Table 6.1. Calculated gas-phase energies and selected geometric data for the six isomers of methyl pyruvate considered in this study. All energies are referenced to the lowest calculated isomer (i.e. ketone s-trans form).

The gas phase reference calculations for all six isomers of methyl pyruvate are presented in Table 6.1. The two keto forms have C=O bond lengths similar to the C=O bond in acetone as expected; the C_1.C_2 bond is equivalent to a C-C single bond. There is a preference for the *s-trans*-keto form of about 4 kJ mol^{-1} over the *s-cis*-keto isomer; this is in line with earlier calculations[3] and the barrier to interconversion between the two isomers is known to be small [4]. When considering the enol isomer, it was discovered that the question of hydrogen bonding has an effect on the relative stability of the systems. The enol hydrogen atom can either be orientated away from the central backbone of the methyl pyruvate molecule or towards the O_2 (*s-cis*) or O_3 (*s-trans*) atom (as shown in Fig. 6.1). This intramolecular hydrogen bond results in a stabilisation of the gas-phase enol by 27 *(s-cis)* and 14 (*s-trans*) kJ mol^{-1}. The extra stabilisation of the less constrained *s-cis* structure is sufficient to reverse the predilection for the *s-trans* isomer seen for the ketone form. Therefore, for the gas-phase enol form of methyl pyruvate, the *s-cis* isomer is preferred as a result of intramolecular hydrogen bonding. Clearly, hydrogen bonding plays an important role in the geometry of the enol form; therefore, all results presented here include the lower energy, hydrogen bonded, form. Finally, the enolate has a significantly higher energy than either the ketone or enol; this is to be expected because of the caveat noted earlier on the treatment of charged species. Of more importance are the geometric parameters;

the C_2-O_1 and C_1-C_2 bond lengths are intermediate between those expected for a single and double bond, suggesting tautomerisation between the C=C and C=O bonds. This is as expected, due to delocalisation around the C-C and C-O bonds.

6.3 Surface adsorption

6.3.1 Adsorption of keto methyl pyruvate

When considering adsorption of methyl pyruvate, in the ketone form, to platinum metal surfaces there are three key types of adsorption mode to consider (optimised structures shown in Fig. 6.2); firstly, an end-on form with the methyl pyruvate bound through one or both C=O moieties (depending on the *s-cis/s-trans* nature). Here the molecule is almost perpendicular to the plane of the surface. Secondly, a similar adsorption mode, but tilted towards the surface at angle of approximately 45 degrees (as commonly observed in the experimental data). Lastly, a mode similar to the second but with additional stabilisation through adsorption of the carbon atom of the *keto* carbonyl functionality (labelled C_2 in Fig. 6.1). In order to describe the geometry of the structures reported here, we will use the same nomenclature used to describe the adsorption of acetone; η^n will be used to describe adsorption modes with *n* adsorbate atoms interacting with one metal atom (e.g. a π -bound mode when n=2) and μ_n to describe adsorption modes where the adsorbate bridges *n* surface atoms (e.g. a di-σ mode when n=2); a *tilted* suffix will be added to distinguish between the first two types of adsorption mode considered above in order to avoid ambiguity and indicate that the molecular plane is not perpendicular to the surface plane.

Surface	Isomer	Geometry	E_{ads} ($kJmol^{-1}$)	M-O (Å)	M-C (Å)	C_2-O_1 (Å)	C_3-O_2 (Å)	C_1-C_2 (Å)	O_1-C_2-C_3-O_3 (°)	M-O-C (°)	Φ (°)	Δ_Z (Å)	Figure
100	Keto	Cis $\mu_2(O_1,O_2)$	37.4	2.12, 2.16	-	1.25	1.24	1.49	2.3	56.9, 54.7	87.9	0.35	6.2a
100	Keto	Cis $\mu_2(O_1,O_2)$-tilted	27.7	2.19, 2.20	-	1.25	1.25	1.49	1.4	27.0, 26.1	33.9	0.30	6.2b
100	Keto	Cis $\mu_3(C_2,O_1,O_2)$	66.2	2.06, 2.16	2.16	1.35	1.27	1.52	43.5	5.4, 14.6	27.6	0.53	6.2c
100	Keto	Trans η^1 (O_1)	14.7	2.14	-	1.24	1.22	1.49	27.6	70.6, -74.6	84.9	0.15	6.2d
100	Keto	Trans η^1 (O_1)-tilted	4.9	2.26	-	1.24	1.22	1.49	4.3	26.2, -23.2	24.4	0.13	6.2e
100	Keto	Trans $\mu_3(C_2,O_1,O_3)$	42.3	2.05, 2.47	2.15	1.36	1.21	1.52	35.1	6.4, -42.0	29.6	0.42	6.2f
111	Keto	Cis $\mu_2(O_1,O_2)$	32.3	2.16, 2.20	-	1.24	1.24	1.49	1.4	56.6, 54.5	89.8	0.15	-
111	Keto	Cis $\mu_2(O_1,O_2)$-tilted	28.3	2.11, 2.22	-	1.29	1.26	1.50	7.3	16.2, 16.1	29.1	0.21	-
111	Keto	Cis $\mu_3(C_2,O_1,O_2)$	47.8	2.05, 2.26	2.22	1.35	1.26	1.52	30.2	16.2, 16.1	30.1	0.37	-
111	Keto	Trans η^1 (O_1)	15.2	2.25	-	1.23	1.22	1.49	1.8	75.9, -78.5	85.5	0.08	-
111	Keto	Trans $\mu_3(C_2,O_1,O_2)$	27.9	2.06, 2.38	2.19	1.36	1.21	1.52	30.5	7.8, -41.4	30.6	0.34	-

Table 6.2: Calculated minimum energy structures for the adsorption of MP in the keto form onto the (100) and (111) surfaces of Pt

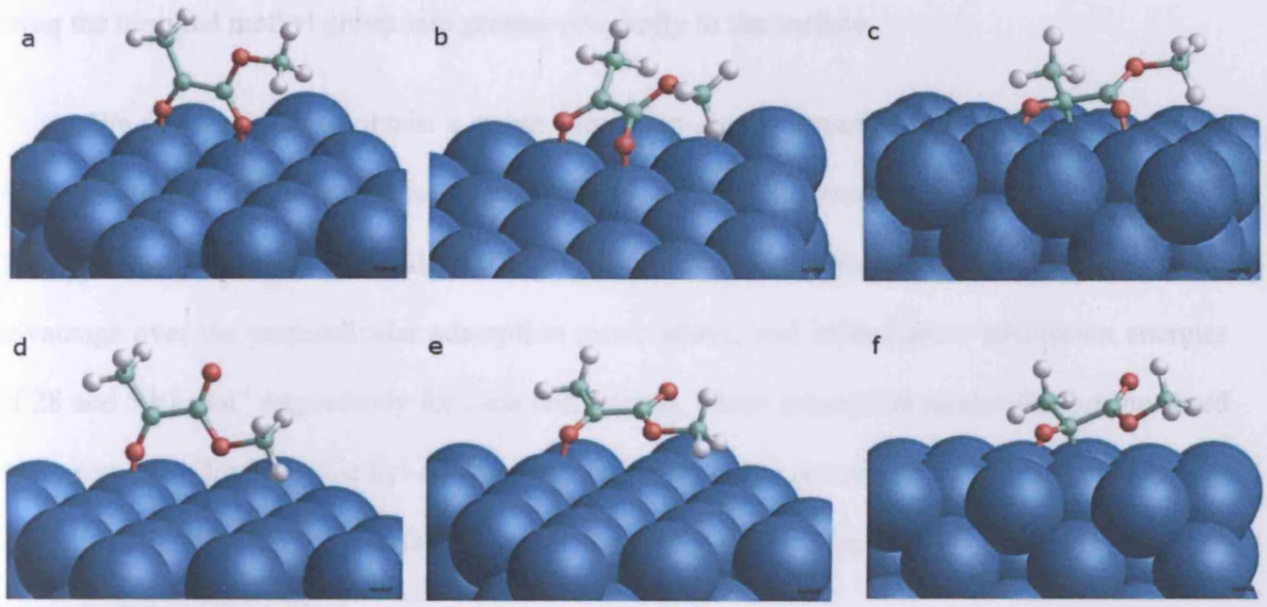

Figure 6.2: Calculated stable adsorption modes of methyl pyruvate (keto form) on the platinum (100) surface. a) s-cis $\mu_2(O_1,O_2)$, b) s-cis $\mu_2(O_1,O_2)$-tilted, c) s-cis $\mu_3(C_2,O_1,O_2)$, d) s-trans η^1 (O_1), e) s-trans η^1 (O_1)-tilted and f) s-trans $\mu_3(C_2,O_1,O_3)$

Considering adsorption to the (100) surface of platinum, the first adsorption modes to be investigated are the $\mu_2(O_1,O_2)$ (*s-cis*) and s-trans η^1 (O_1) (*s-trans*) adsorption modes (Fig. 6.2a and Fig. 6.2d) which are similar to the end-on adsorption mode which is preferred for the keto form of acetone. The geometry of the methyl pyruvate changes little from the gas phase form and the adsorbate is found to be almost perpendicular to the surface plane ($\varphi = 88^{\circ}$). This is one of the modes considered to be theoretically the most favourable when interpreting experimental data; the two lone pairs on the keto oxygen atoms are orientated towards the surface (for *s-cis*) in order to effect efficient interaction with the metal atoms; additionally, this geometry will also minimise steric repulsion between the two relatively bulky methyl groups and the surface. We find this structure to have a favourable adsorption energy of 37 and 15 kJ mol^{-1} for the *s-cis* and *s-trans* forms respectively. This difference is explained by the inability of the *s-trans* isomer to bond both carbonyl oxygen atoms to the surface; instead, the second interaction is via the O_3 atom. This ester oxygen atom is less suited to interact strongly with the surface; this will also

bring the terminal methyl group into greater proximity to the surface.

We are also able to obtain a stable minimum energy structure similar to that described above but tilted towards the surface plane (φ =24 *s-cis* or 34° *s-trans*) (Fig. 6.2b and Fig. 6.2e). These $\mu_2(O_1,O_2)$-tilted *(s-cis)* and η^1 (O_1)-tilted *(s-trans)* adsorption modes have no theoretical advantage over the perpendicular adsorption mode above, and indeed show adsorption energies of 28 and 5 kJ mol^{-1} respectively for *s-cis* and *s-trans*. These adsorption modes exhibit increased steric repulsion from the methyl-surface interaction and also orientates the two C=O lone pairs 'off-axis' to interact with the surface. A weak (M-C_3 = 2.9Å) interaction is observed between the ester oxygen and the surface.

The most favourable adsorption mode for the ketone form is found to be a $\mu_3(C_2,O_1,O_x)$ (Fig. 6.2c (x=2) and Fig. 6.2f (x=3)) geometry which is similar to the $\mu_2(C_2,O)$ geometry observed for acetone but with an additional point of contact *via* a keto or ester oxygen atom. Although the two oxygen lone pairs are again orientated away from an interaction with the surface, the π-system of the methyl pyruvate is ideally positioned to interact with the surface. This is shown by an additional C_2-Pt bond, in effect creating a di-σ bridged C=O bond. The C_2 carbon atom now displays a slightly distorted sp^3-like geometry; the C_2-O_1 bond has also lengthened to the value seen in the gas-phase enol form in order to accommodate the additional surface bond. The *s-cis* structure is again preferred to the *s-trans* isomer due to the ability to bond the second *keto* oxygen to the surface, whereas only a weak ester – metal bond is possible for the *s-trans* isomer.

This di-σ bridged C=O bonding mode is also seen for both acetone and formaldehyde adsorption. This is the most favourable adsorption mode for formaldehyde, but is destabilised for acetone due to interaction of the methyl groups with the surface. In methyl pyruvate, however, this steric repulsion is overcome by the additional Pt-O_3 interaction and the ability of the O-CH_3 group to increase the height of the methyl group above the surface plane.

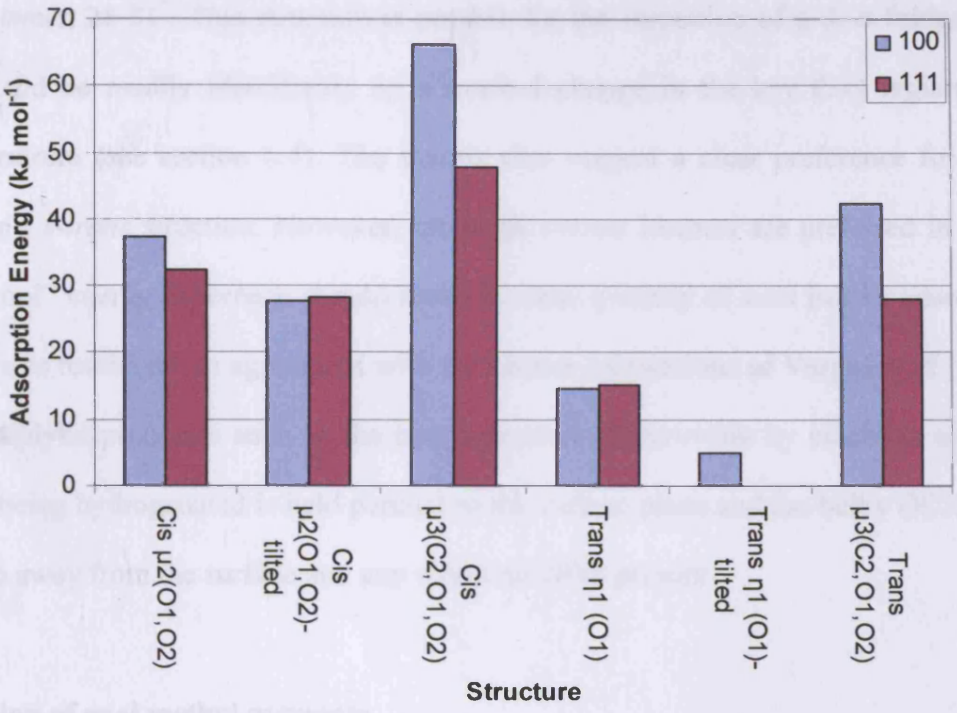

Figure 6.3: The trend in adsorption energies for MP in the ketone form adsorbed onto (100) and (111) Pt surfaces

The adsorption of the keto form of methyl pyruvate to a Pt (111) surface exhibits the same trends as those seen for the Pt (100) surface (Fig. 6.3). However, a significant decrease in adsorption energy is observed for the most favourable (111) structures when compared to their (100) analogues; the most stable $\mu_3(C_2,O_1,O_2)$ adsorbate has an adsorption energy of approximately 30% less for the (111) form. In general, the (111) adsorbates show more geometrical strain and a less idealised geometry than the (100) adsorbates as seen, for example, through a slight increase in bond lengths when comparing (111) to equivalent (100) structures. The weakest (100) structure (the s-trans- $\mu_2(O_1,O_2)$-tilted geometry) was found not to have an equivalent on the (111) surface (the structure was unstable).

The preferential adsorption mode for the methyl pyruvate keto form on either Pt (100) or

(111) surfaces is thus expected to be a $\mu_3(C_2,O_1,O_2)$ structure inclined towards the surface plane at angle of between 28-31°. This structure is notable for the formation of a di-σ bridged C=O bond; this should be readily identifiable by a marked change in the key C-O region of the vibrational spectrum (see section 6.4). The results also suggest a clear preference for a *s-cis* adsorbate over a *s-trans* structure. However, although *s-trans* isomers are preferred in the gas phase, a 4 kJ mol^{-1} energy difference should result in some quantity of *s-cis* isomer adsorbed on the surface. These results are in agreement with the cluster calculations of Vargas *et al* [5]. This is crucial to catalytic processes such as the hydrogenation of pyruvates by cinchona alkaloids; the C-C bond being hydrogenated is held parallel to the surface plane and the bulky OCH_3 group is free to rotate away from the surface and any chiral modifier present.

6.3.2 Adsorption of enol methyl pyruvate

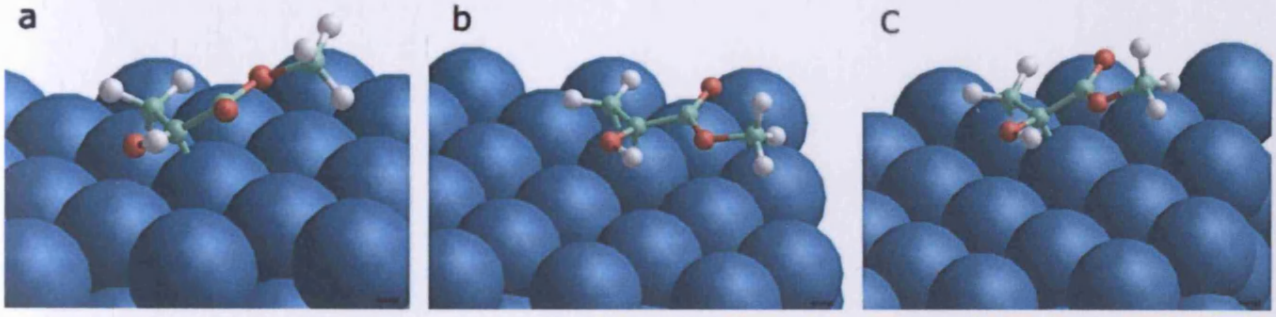

Figure 6.4: Calculation stable adsorption modes of methyl pyruvate (enol form) on the platinum (100) surface. a) s-cis $\mu_3(C_1,C_2, O_1)$, b) s-trans $\eta^2(C_1, C_2)$, c) s-trans $\mu_2(C_1,C_2)$.

When studying the adsorption of the enol form of methyl pyruvate to the platinum surfaces, the $\mu_2(O_1,O_2)$ form is not a stable minima for either surface; protonation of the O_1 atom destabilises the C=O(H)-M interaction. As the bulk of the methyl group has been reduced due to the removal of the proton to form the enol, the terminal carbon atom can now interact with the surface and revert to a more sp^3-like geometry as seen in Fig. 6.4 and Table 6.3. All stable energy minima for the enol form involve the interaction of the C=C bond with the surface (either

as a π- or di-σ interaction), with a possible tertiary interaction between the hydroxyl oxygen atom and the surface; the remainder of the molecule orients itself away from the surface. This is a marked change from the keto form where the primary metal – adsorbate interaction was *via* the two carboxyl groups.

Surface	Isomer	Geometry	E_{ads} (kJmol^{-1})	M-O (Å)	M-C (Å)	C_2-O_1 (Å)	C_3-O_2 (Å)	C_1-C_2 (Å)	O_1-C_2-C_3-O_3 (°)	M-O-C (°)	Φ (°)	Δ_Z (Å)	Figure
100	Enol	Cis $\mu_3(C_1,C_2,O_1)$	100.2	2.39	2.12, 2.11	1.43	1.23	1.49	14.3	-5.8, -15.0	19.5	0.51	6.4a
100	Enol	Trans η^2 (C_1, C_2)	68.6	-	2.18, 2.19	1.38	1.21	1.42	27.0	-3.8, -21.2	19.7	0.35	6.4b
100	Enol	Trans $\mu_2(C_1,C_2)$	95.6	-	2.10, 2.14	1.39	1.22	1.49	28.5	-15.4, -11.6	17.4	0.44	6.4c
111	Enol	Cis $\mu_2(C_1,C_2)$	86.7	-	2.12, 2.16	1.38	1.23	1.50	22.3	-16.6, -19.3	21.2	0.44	-
111	Enol	Trans η^2 (C_1, C_2)	51.2	-	2.16, 2.41	1.35	1.22	1.41	14.0	-8.2, -8.2	13.9	0.32	-
111	Enol	Trans $\mu_2(C_1,C_2)$	64.8	-	2.12, 2.19	1.38	1.22	1.49	30.9	-19.8, -10.5	16.4	0.46	-

Table 6.3: Calculated minimum energy structures for the adsorption of MP in the enol form onto the (100) and (111) surfaces of Pt

The *s-cis* enol form (Fig. 6.4a) adsorbed on (100) has the strongest adsorption energy of any isomer considered in this section of the study (100 kJ mol^{-1}). This structure has a di-σ bridged C=C bond and a relatively weak (2.39Å) hydroxyl oxygen-metal interaction. The C-O bond has lengthened to 1.43Å as a result of this interaction, although the C=C bond has lengthened from the gas-phase value of 1.34Å to 1.49Å, a value more consistent with a C-C single bond. A large surface-adsorbate interaction is observed (Δz = 0.51Å) and the plane of the molecule is at a very shallow angle to the surface (φ = 14.3°).

The *s-trans* enol form exists in two similar adsorption modes (Fig. 6.4b, 6.4c), differentiated by the type of C=C – metal bond; as seen for the keto form, the *s-cis* form exhibits a stronger adsorption energy than the *s-trans* form. The $\eta^2(C_1, C_2)$ structure (Fig. 6.4b) has a π-bound C=C bond as the primary interaction with the surface. The C=C bond has lengthened compared to the gas phase, but is still shorter than the di-σ bound modes at 1.42Å. The η^2 (C_1, C_2) mode has an adsorption energy of 69 kJ mol^{-1}, but a related structure, the $\mu_2(C_1,C_2)$ mode (Fig. 6.4c), has a more favourable adsorption energy of 96 kJ mol^{-1}. This structure differs only by having a di-σ bound C=C bond with an greater C-C bond length of 1.49Å. The difference in adsorption energies between the di-σ and π-bound enol methyl pyruvate is of the order predicted by previous periodic DFT calculations studying the adsorption of ethane to the platinum (111) surface[6] ; the bond lengths calculated here for the methyl pyruvate C=C, 1.42Å for π-bound (1.40Å for ethene) and 1.49Å for di-σ bound (1.48Å for ethene), are in accordance with the earlier adsorbed ethane model as well. In both of these structures the tertiary M-O interaction noted for the *s-cis* form had decreased to the point where the M-O distance (approximately 2.9Å) was too large to be considered a significant interaction.

One important point to note is that, in line with previous calculations on acetone, all three calculated enol geometries (it was not possible to obtain a stable *s-cis* π-bound mode, although this should be lower in energy) have a more favourable adsorption energy than any of the keto

structures. The strong interaction of the two C=C carbon atoms with the surface, and the much weaker interaction of the hydroxylated oxygen atom, results in the relative energetic difference between the most stable *s-cis* and *s-trans* modes being only 5 kJ mol^{-1}.This is much less than found for the keto-isomer.

The adsorption of methyl pyruvate in the enol form to the (111) surface of platinum follows the same trend in structure and energetic ordering as that observed for the (100) surface. The most favourable structure is a di-σ bound *s-cis* geometry, with an adsorption energy of 87 kJ mol^{-1}, and a geometry similar to that found on the (100) surface (although the tertiary M-O interaction is not present due to the differing geometry of the (111) surface). Two *s-trans* structures are also found, one a π- and one a di-σ bound structure. The π-bound $\eta^2(C_1, C_2)$ geometry has an adsorption energy of 51 kJ mol^{-1} and the di-σ $\mu_2(C_1,C_2)$ geometry has an adsorption energy of 65 kJ mol^{-1}, following the trend observed for the (100) surface.

6.3.3 Adsorption of enolate methyl pyruvate

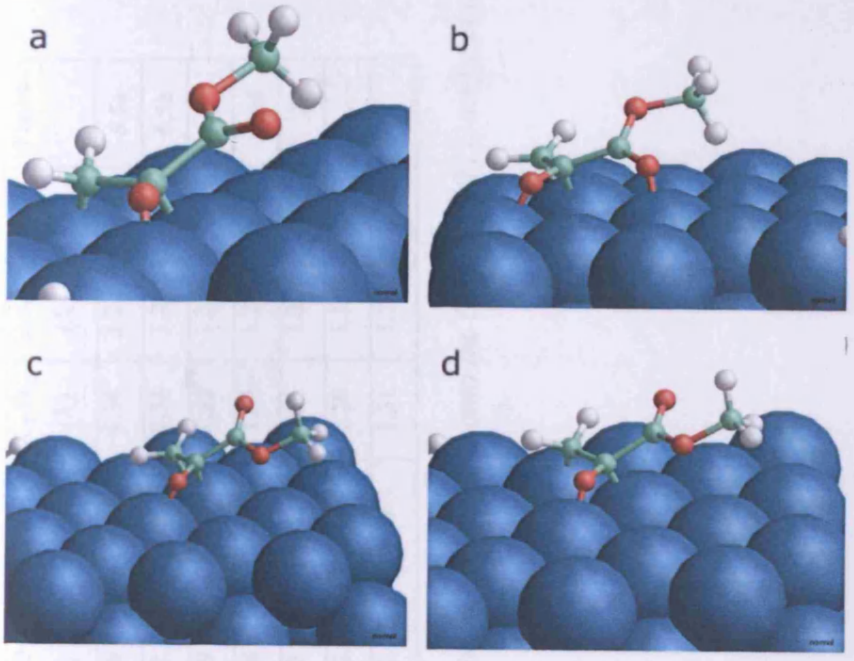

Figure 6.5: Calculated stable adsorption modes of methyl pyruvate (enolate form) on the platinum (100) surface. a) s-cis $\mu_3(C_1,C_2, O_1)$, b) S-cis μ_3 (η^2 (C_1,C_2), O_1, O_2), c) s-trans μ_2 (η^2 (C_1,C_2), O_1), d) s-trans $\mu_3(C_1,C_2, O_1)$.

Surface	Isomer	Geometry	E_{ads} (kJmol^{-1})	M-O (Å)	M-C (Å)	C_2-O_1 (Å)	C_3-O_2 (Å)	C_1-C_2 (Å)	Figure
100	Enolate	Cis $\mu_3(C_1,C_2,O_1)$	80.8	2.06	2.11, 2.19	1.34	1.22	1.49	6.5a
100	Enolate	Cis μ_3 (η^2 (C_1,C_2), O_1, O_2)	82.0	2.10, 2.18	2.16, 2.23	1.33	1.25	1.44	6.5b
100	Enolate	Trans μ_2 (η^2 (C_1,C_2), O_1)	71.0	2.09	2.16, 2.27	1.32	1.22	1.44	6.5c
100	Enolate	Trans $\mu_3(C_1,C_2,O_1)$	77.8	2.08	2.11, 2.17	1.34	1.22	1.50	6.5d
111	Enolate	Cis $\mu_4(C_1,C_2,O_1,O_2)$	34.0	2.05, 2.30	2.16, 2.31	1.33	1.26	1.48	-
111	Enolate	Cis $\mu_3(C_1,O_1,O_2)$	32.2	2.12, 2.25	2.14	1.29	1.26	1.46	-
111	Enolate	Trans μ_2 (η^2 (C_1,C_2), O_1)	28.0	2.12, 2.17	2.39	1.31	1.22	1.43	-

Table 6.4: Calculated minimum energy structures for the adsorption of MP in the enolate form onto the (100) and (111) surfaces of Pt

The adsorption of methyl pyruvate as an enolate with the associated H atom follows a similar trend as that exhibited for the enol form, with the exception that the formerly enolised-oxygen atom is now available for bonding to the surface atoms more readily. Interaction is primarily via the C=C bond, but significant interaction also occurs through one, or both, of the keto oxygen atoms. In a similar fashion to the convention used for enolate acetone, the extra hydrogen atom is placed in a 3-fold hollow adsorption site; this is the most favourable for hydrogen adsorption (section 5.2). The *s-cis* enolate form bonds to the (100) surface via either a di-σ or π-bound mode in a similar fashion to the enol form. The $\mu_3(C_1,C_2, O_1)$ di-σ bound mode (Fig. 6.5a) bonds to the surface in a similar manner to the analogous enol form, with an increased M-O interaction with the keto oxygen (2.06 Å compared to 2.39 Å for the enol form). The (η^2 (C_1,C_2), O_1, O_2) π-bound mode (Fig. 6.5b), which was less stable in the enol form, shows a similar adsorption energy to the di-σ mode (only 1 kJ mol^{-1} energy difference). This is due to the extra stabilisation arising from an additional M-O bond caused by the ability of the enolate to get closer to the surface than the enol, and the different geometry of the π-bound mode placing the oxygen in a more favourable position to bond to the surface.

The *s-trans* enolate form bonds to the surface in a similar fashion, with the exception that the second oxygen atom no longer interacts with the surface. This means that the π-bound mode (Fig. 6.5c), which exhibited the second oxygen bond in *s-cis* form, is destabilised relative to the di-σ (Fig 6.5d), albeit not to the extent seen in the enol form (only 7 kJ mol^{-1} destabilisation compared to 35 kJ mol^{-1} for the enol case). In an analogous fashion to the enol form, the energy difference between the *s-cis* and *s-trans* isomers has decreased markedly when compared to the keto form (the least stable *s-trans* structure is only 11 kJ mol^{-1} less stable than the most favourable *s-cis* structure. Adsorption of the enolate form onto the Pt (111) surface shows the same pattern of adsorption energies for the *s-cis* and *s-trans* isomers as described above. A slight preference is shown for the *s-cis* di-σ ($\mu_4(C_1,C_2, O_1, O_2)$ mode over the second *s-cis* mode ($\mu_3(C_1$, O_1, O_2) where one carbon is bound in an atop fashion together with the two surface-oxygen

bonds. Finally only one stable *s-trans* species is observed – a π-bound (η^2 (C_1,C_2), O_1) geometry, with an adsorption energy just lower than that of the *s-cis* species.

6.4 Vibrational Analysis

Vibration	Experimental Liquid Phase (keto form)		Calculated (keto form)		Calculated (enol form)		Calculated (enolate form)	
	s-cis	*s-trans*	*s-cis*	*s-trans*	*s-cis*	*s-trans*	*s-cis*	*s-trans*
Enol O-H str.	-	-	-	-	3545	3679	-	-
Sym. C=O str.	1762	1741	1766	1741	1701	1737	1685	1630
Asym. C=O str.	1733	1737	1747	1713	-	-	1390	1381
Alkene C=C str.	-	-	-	-	1672	1661	1462	1454
Alcohol C-O str.	-	-	-	-	1357	1316	-	-
Ester C-O str.	1213	1191	1202	1254	1242, 1191	1221, 1120	1227	1225
Alkene-H out of plane bend	-	-	-	-	842, 718	853, 722	858, 683	849, 464

Table 6.5: Selected key gas-phase calculated vibrational frequencies compared with experimental liquid phase values (reference [7]). All frequencies in cm^{-1}.

The gas phase calculated vibrational frequencies for methyl pyruvate in all of its isomeric forms, compared with experimental reference data, is presented above in Table 6.5. There is good agreement between our calculated keto vibrations and the experimental data. It is interesting to note that the enol and enolate form show a markedly different pattern of vibrations to the keto form. The enol form has a high-frequency O-H stretching mode not present in any of the other isomers; if this is readily detectable, this should be a unique characteristic of the gas-phase enol form. However, on supported catalyst particles this region is complicated by surface hydroxyl species. One of the C=O stretches is replaced by a C-O enol vibration some $350cm^{-1}$ lower than the keto C=O stretch. An additional C=C stretch from the newly-created CH_2 group is observed at 1660-1672 cm^{-1}; additionally, an alkene hydrogen out of plane bend is seen at lower

frequencies. The protonation of the oxygen atom also means that the ester C-O stretch now splits into symmetric and asymmetric vibrations. The enolate form has a similar spectrum to that of the keto form, with the additional C=C stretch and hydrogen out of plane bends mentioned before. One of the C=O stretches also shifts approximately 330 cm^{-1} lower, most likely due to delocalisation around the C=C and C=O moiety.

Vibration	S-cis $\mu_2(O_1,O_2)$ (cm^{-1})	S-cis $\mu_2(O_1,O_2)$-tilted (cm^{-1})	S-cis $\mu_3(C_2,O_1,O_2)$ (cm^{-1})	S-trans η^1 (O_1) (cm^{-1})	S-trans η^1 (O_1)-tilted (cm^{-1})
OMe stretches	3136, 3084, 3007	3114, 3049, 2908	3113, 3066, 2960	3083, 3077, 2987	3098, 3064, 2976
CMe stretches	3108, 3037, 2987	3081, 3038, 2978	3070, 3035, 2969	3103, 3038, 2985	3096, 3056, 2976
C=O stretches	1618, 1536	1469, 1432	1498, 1180	1723, 1653	1738, 1160
C-O stretch	1226	1239	1250	1247	1025
OMe modes	1440-1418, 1184, 1129	1423-1397, 1169, 1114	1435-1408, 1168, 1123	1434-1409, 1162, 1126	1427-1401, 1131, 1119
CMe modes	1404-1337, 1136	1405-1337, 1125	1416-1344, 1101	1398-1332, 1114	1417-1341, 1148

Table 6.6: Selected calculated vibrational frequency data for adsorbed keto form of methyl pyruvate on Pt (111)

The calculated vibrational frequencies for all of the keto forms on a Pt (111) surface considered in this study are shown in Table 6.6. The most interesting feature of this data is the downshifting of the two C=O vibrational frequencies, as already demonstrated for the vibrational spectrum of adsorbed acetone. A key feature is the ability to distinguish *s-cis* and *s-trans* modes on the surface. In the *s-trans* form of methyl pyruvate, only one oxygen atom is involved in bonding with the surface; the other shows negligible shifting of frequency, remaining close to the calculated gas phase value. In contrast, *s-cis* methyl pyruvate interacts via both of the ketone oxygen atoms, and both are shifted down in frequency.

The magnitude of the shift in the C=O stretching frequency could be used to 'fingerprint' the adsorption mode, as already used in the study of acetone adsorption. The two perpendicular

adsorption modes, s-cis $\mu_2(O_1,O_2)$ and s-trans η^1 (O_1), show the least shifting; the *s-cis* isomer shifts down by approximately 110 and 200 cm^{-1}, and the *s-trans* isomer shifts by 90 cm^{-1} compared to the gas phase values. These shifts in vibrational frequencies are in agreement with the acetone η^1 (O_1) ketone shift of 130 cm^{-1}, which also contains C=O bonds alignment perpendicular to the surface. The two tilted adsorption modes, s-cis $\mu_2(O_1,O_2)$-tilted and s-trans η^1 (O_1)-tilted, have a similar pattern of vibrational frequencies as the perpendicular modes, with the C=O stretching frequencies shifted further downward by approximately 30-50 cm^{-1} compared to the perpendicular modes. The two $\mu_3(C_2,O_1,O_2)$ modes show further shifting of C=O stretching frequencies. In the *s-cis* isomer, one of the C=O stretches shifts by 100cm^{-1} compared to the tilted adsorption mode; the other C=O stretch for the *s-cis* isomer, together with the one shifted *s-trans* frequency, show considerable shifting to approximately 1120-1180cm^{-1}, which is in agreement to the parallel-bonded acetone C=O stretch (1161cm^{-1}).

	S-cis $\mu_2(C_1,C_2)$ (cm^{-1})	S-trans η^2 (C_1, C_2) (cm^{-1})	S-trans $\mu_2(C_1,C_2)$ (cm^{-1})
Enol O-H stretch	3447	3554	3453
OMe stretches	3129, 3084, 2988	3116, 3097, 3008	3109, 3076, 3000
CMe stretches	3114, 3032	3168, 3067	3080, 2997
C=O stretch	1672	1732	1699
C=C modes	1381, 1345, 1073	1498, 1366	1380, 1330, 1074
C-O stretches	1233, 1187	1283, 1189	1204, 1170, 1148
OMe modes	1443-1403, 1155, 1120	1439-1411, 1172, 1131	1443-1415, 1124
CMe modes	1032	1110	1032

Table 6.7: Selected calculated vibrational frequency data for adsorbed enol form of methyl pyruvate on Pt (111)

The calculated vibrational frequencies of the enol form of MP on a Pt (111) surface are shown in Table 6.7. The key features to note here are the presence of the high-level O-H stretching mode as noted in the gas-phase, and the lack of down-shifting of the C=O bond. A C=O-surface bond is not present in any of the enol structures shown here, so the C=O stretching frequency remains close to that observed for the gas phase. The stretching C=C modes of the

alkene functionality are downshifted from approximately 1660 cm^{-1} in the gas phase to approximately 1380 cm^{-1}, with the exception of the most weakly-bound mode (s-trans η^2 (C_1, C_2)) which is only downshifted to 1500 cm^{-1}. A variety of modes associated with the C-O stretching of the enol group overlap with those with the ester C-O moiety and occur between 1230 and 1180 cm^{-1}. Again, the least strongly bound mode is slightly higher at 1280 cm^{-1}.

	s-cis $\mu_4(C_1,C_2,O_1,O_2)$	s-cis $\mu_3(C_1,O_1,O_2)$	s-trans μ_2 (η^2 (C_1,C_2), O_1)
OMe stretches	3122, 3064, 2968	3123, 3063, 2988	3109, 3067, 2977
CMe stretches	3093, 3012	3113, 3022	3144, 3040
C=O stretches	1491, 1222	1493, 1355	1720, 1324
C=C stretch	1389, 1251	1412, 1233	1422, 1242
OMe modes	1430-1402, 1168, 1116	1438-1401, 1178, 1127	1425-1406, 1162, 1128
CMe modes	1122	1136	1096

Table 6.8: Selected calculated vibrational frequency data for adsorbed enolate form of methyl pyruvate on Pt (111)

The vibrational frequencies for the enolate form of MP show a marked downshifting of the C=O bond stretching, especially for the S-cis $\mu_4(C_1,C_2,O_1,O_2)$ structure, the geometry with the most interaction with the surface. The *s-trans* form again exhibits one non-interacting C=O stretch close to the gas phase value. A C=C frequency close to that observed for the enol form is seen here as well.

6.5 Conclusions

The structures of the keto, enol and enolate ion forms of methyl pyruvate adsorbed onto a (100) and (111) surface have been investigated. In terms of geometry and energy, similar trends were observed for adsorption on the two surfaces. The (111) surface tended to show more constrained and less favourable adsorption geometries, resulting in a small lowering of stability compared to adsorption on the (100) surface. It was proposed that the keto form could adsorb in one of three modes; "end-on" (*via* the lone pairs of the oxygen atoms), a tilted adsorption mode similar to end-on and a closely bound mode interacting through the π-system of the MP. The last form was found to be the most stable. The most stable keto structure was a *s-cis* structure bound through the π-system of the two oxygen atoms and the carbonyl carbon atom, having an adsorption energy of 66 kJ mol^{-1}. The end-on structure was the next most stable structure. The *s-trans* keto form had the same geometry, but a slightly lower adsorption energy (42 kJ mol^{-1}). The enol form showed a surface bridged C=C bond with additional stabilisation from the enolised oxygen atom. The *s-cis* enol isomer had the highest adsorption energy found in this study (100 kJ mol^{-1}), close to the *s-trans* form at 96 kJ mol^{-1}; this is in agreement with acetone, where the enol structure was more stable than either keto and enolate forms. These structures effectively anchor one end of the MP to the surface *via* the π-system, leaving the bulk of the molecule free for any possible interactions. The enolate had a similar structure to the enol, with additional oxygen interactions; adsorption energies of 82 kJ mol^{-1} (*s-cis*) and 78 kJ mol^{-1} (*s-trans*) were found. Therefore, although the *s-trans*-keto form is favoured in the gas phase, the *s-cis* form is favoured on the surface. However, with the exception of the keto form, the energy difference between *s-cis* and *s-trans* form is minimal. The most stable species was found to be the *s-cis* enol form of MP. However, given that much of the incoming MP is in the *s-trans*-keto form, studies of the barrier to conversion between forms (and *s-cis*/*s-trans* isomers) are needed in order to determine whether this is feasibly possible.

In terms of identifying species on the surface, the calculated vibrational frequencies show

promise in differentiating between the different forms of MP. Irrespective of the type of MP present, the *s-trans* isomer exhibits one free C=O bond which doesn't interact with the surface; therefore, the vibrational frequency is close to the free gas-phase C=O frequency. The C=O moiety which is bonded to the surface shows a downshift of approximately 200-300 cm^{-1}. The enol form of MP typically shows a characteristic high-level O-H band at about 3400-3500 cm^{-1} which is not present for the keto or enolate form. Although the enolate form shows a similar shifting of the C=O frequency, additional bands are introduced at around 1400-1200 cm^{-1} due to the C=C bond stretching. Therefore, it should be possible to determine experimentally which form of MP is present on the surface.

6.6 References

(1) Bonello, J. M.; Williams, F. J.; Santra, A. K.; Lambert, R. M. *J. Phys. Chem. B* **2000**, *104*, 9696.
(2) Bürgi, T.; Atamny, F.; Knop-Gericke, A.; Hävecker, M.; Schedel-Niedrig, T.; Schlögl, R.; Baiker, A. *Catal. Lett.* **2000**, *66*, 109.
(3) Hutchings, G. J.; Willock, D. J. *Topics in Catalysis* **1998**, *5*, 177.
(4) Ferri, D.; Bürgi, T.; Baiker, A. *J. Chem. Soc. Perkin Trans. 2* **2000**, *2*, 221.
(5) Vargas, A.; Bürgi, T.; Baiker, A. *J. Catal.* **2004**, *222*, 439.
(6) Watson, G. W.; Wells, R. P. K.; Willock, D. J.; Hutchings, G. J. *J. Phys. Chem. B* **2000**, *104*, 6439.
(7) Wimshurst, J. K.; Horwood, J. F. *Aust. J. Chem.* **1971**, *24*, 1183.

7. Transition state searching

7.1 Introduction

In chapters 5 and 6 a wide variety of systems have been considered in terms of the adsorption of molecules onto a metal surface. This provides an insight into the start point of many surface reactions, but on its own does not help to elucidate reaction barriers and mechanism. For example, the enolate form of acetone may be the most stable on the surface, but adsorption from the gas phase will primarily occur in the ketone form; if the barrier to interconversion is high, the stability of the enolate is of less importance. Also, the ketone η^1(O) adsorption mode of acetone may be more stable than the μ_2(C,O) mode, but if hydrogenation of the η^1(O) mode cannot directly occur (due to a high energy barrier for geometric reasons) then the barrier to convert directly between adsorption modes needs to be taken into account. Therefore, it would be advantageous to be able to obtain the energies and structures of the transition states within these systems.

7.2 Methodology

Within the VASP code, there is no built-in method for the direct calculation of transition states. Therefore, in order to calculation energy barriers, a protocol must be developed to obtain a good approximation to a transition state energy and structure. This will then be applied to a simple system (hydrogen on a metal surface) before moving on to larger, more complicated, systems such as the interconversion between isomers of acetone.

In order to obtain an initial guess for a transition state, the Nudged Elastic Band (NEB) method will be used as implemented in VASP [1] (section 4.1). A series of intermediate states along the reaction path between a start and end point must be defined. These structures are then simultaneously minimised, restricting atomic motion such that changes only occur perpendicular to the reaction path. The generation of the intermediate images is performed using the *inter_vasp* program (a utility program for generating first guess structures along a reaction co-ordinate based on chemically informed rules [2]). For these calculations a central atom is defined and all other atoms in the molecule are interpolated so that the distance to the central atom varies smoothly from the start to end point as the central atom moves along the reaction path. This is to avoid problems with artificial shortening of interatomic distances observed when a linear interpolation is performed with all atoms.

Once the initial calculation using the NEB has been performed, a plot of reaction coordinate *vs* energy should give a well-defined maximum. If an energy maximum cannot easily be realised, additional NEB calculations can be performed between two of the intermediate structures from the first calculation; this will have the effect of introducing points which are closer together along the reaction path and hopefully helping to more clearly define the energy maximum. Once a candidate for the maximum energy structure has been identified, a full

geometry optimisation is performed; there should be minimal change in the calculated total energy of this structure to ensure that it is close to the maximum point.

In order to refine the maximum point further, a vibrational frequency analysis is performed upon the candidate structure (all adsorbate atoms are included in the Hessian matrix, all metal atoms are frozen) which will yield 3N vibrational modes. If the image is sufficiently close to the transition state, one strong negative vibrational frequency will be found. The *inter_vasp* program can then be used to 'follow' this frequency; a number of finely-spaced images are produced along the vector corresponding to this frequency and a single point energy calculation is performed on each image. This has the effect of 'stepping along' the vector. A plot of coordinate *vs* energy should reveal an energy maximum corresponding to the transition state; a plot of coordinate *vs* force should show a coincident minimum.

7.3 Hydrogen

Having defined the methodology to be used in section 7.2, it is now necessary to apply this to a simple test case in order to verify that it works. The simplest case described in chapter 5 was the adsorption of hydrogen onto and into Group 10 metal surfaces. Therefore, the transition state and corresponding energy barrier for hydrogen transition between a subsurface and the equivalent surface site will be calculated.

7.3.1 Hydrogen on Ni (111)

The first case to be considered is the movement of a hydrogen atom from an O_h hole to an fcc-type surface site on Ni (111). This particular system was previously studied using a periodic-slab model and an energy barrier of approximately 85 kJ mol^{-1} was predicted for the surface to subsurface transit [3]. The starting and ending structures are those described in section 5.2. The 'first pass' run between these starting and ending structures is shown in Fig. 7.1 using five intermediate images between the two structures.

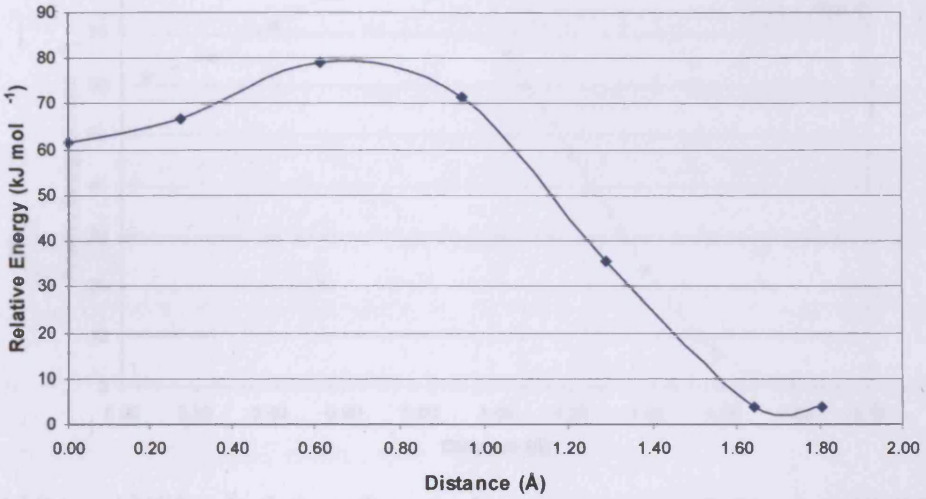

Figure 7.1: The first pass NEB calculation for a hydrogen atom resurfacing on a Ni (111) surface from a O_h subsurface hole.

In Fig. 7.1, the subsurface state is shown on the left side of the graph, and the surface-bound state on the right side. The x-axis shows the reaction coordinate; in this case, the only movement is in the z-direction; the reaction coordinate is therefore simply the distance from the starting (subsurface site). An initial first guess of 80 kJ mol^{-1} is obtained for the barrier to surface-subsurface movement and 15-20 kJ mol^{-1} for the reverse reaction (reemergence). Although an approximate guess for the energy barrier can be made, there is not a sharply defined maximum to be able to attempt to locate a transition state. Therefore, additional NEB calculations are needed (Fig. 7.2).

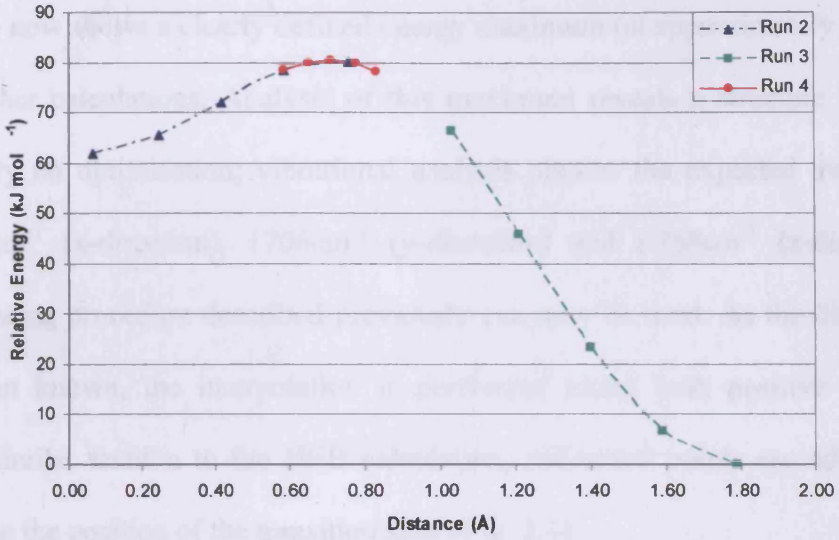

Figure 7.2: Additional NEB calculations for a hydrogen atom resurfacing on a Ni (111) surface from a O_h hole.

In Fig. 7.2, three additional calculations have been performed; one run to each side of the initial maximum point, and a finer run over the top of the maximum point. The energies from all four calculations have been combined in Fig. 7.3.

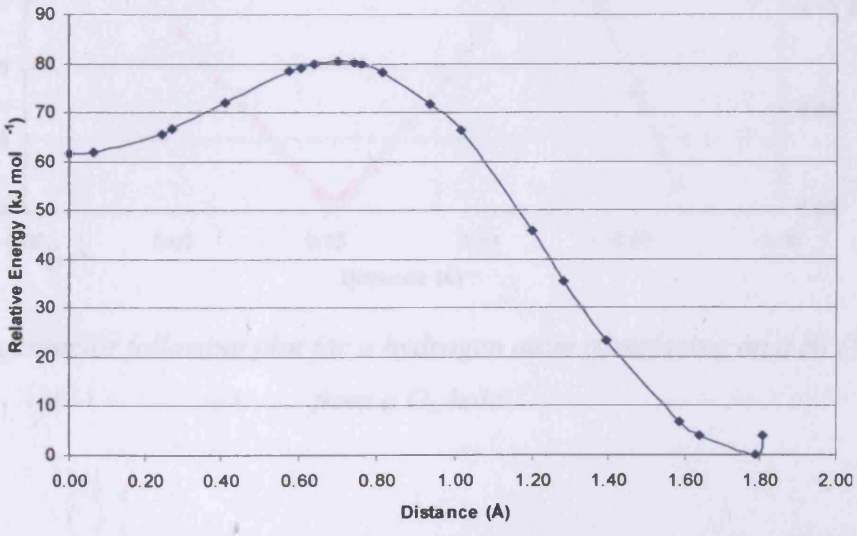

Figure 7.3: Combined NEB plot for a hydrogen atom resurfacing on a Ni (111) surface from a O_h hole.

Figure 7.3 now shows a clearly defined energy maximum (at approximately 0.7 Å) which can used for further calculations. Analysis of this maximum reveals a structure that does not move significantly on optimisation; vibrational analysis obtains the expected three modes of hydrogen: 1709cm^{-1} (x-direction), 1706cm^{-1} (y-direction) and *i*-768cm^{-1} (z-direction). The eigenvector following procedure described previously can now be used. As the direction of the eigenvector is not known, the interpolation is performed along both positive and negative directions; in a similar fashion to the NEB calculation, additional points are added in where necessary to refine the position of the transition state (Fig. 7.4).

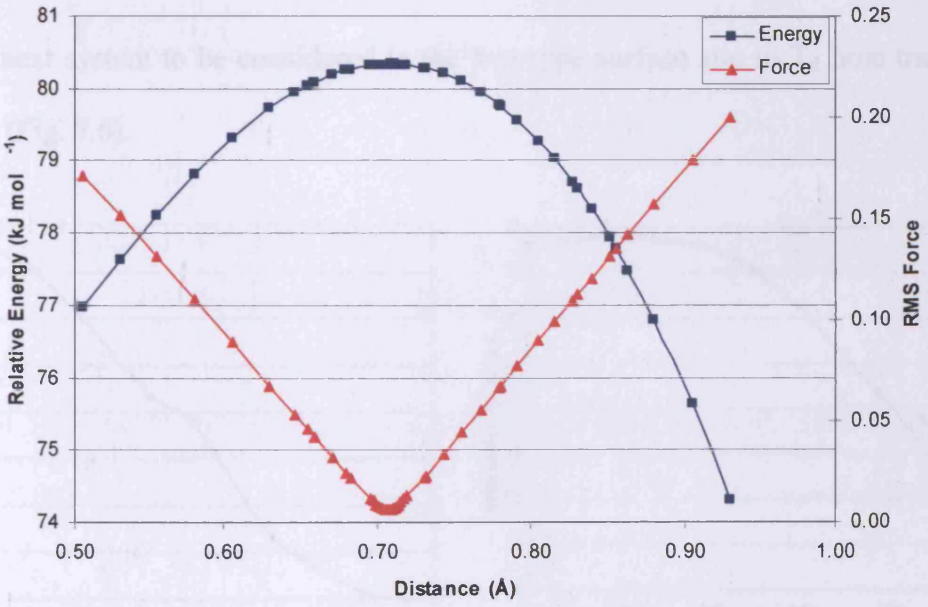

Figure 7.4: Eigenvector following plot for a hydrogen atom resurfacing on a Ni (111) surface from a O_h hole.

The eigenvector plot in Fig. 7.4 shows a maximum in energy and a coincident minimum in force; therefore, this is the likely location of the transition state. The corresponding structure is shown in Fig. 7.5. The hydrogen atom is 0.18 Å below the plane of the metal atoms.

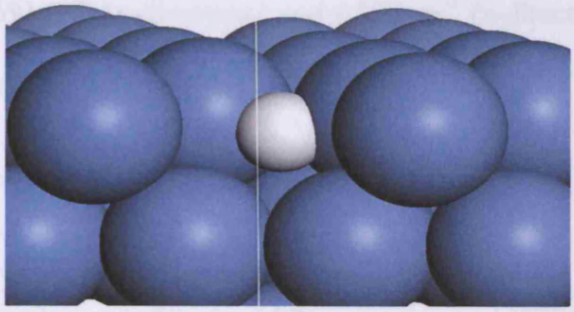

Figure 7.5: Structure of the transition state for a hydrogen atom resurfacing on a Ni (111) surface from a O_h hole.

The next system to be considered is the hcp-type surface site to T_d hole transition, also for Ni (111) (Fig. 7.6).

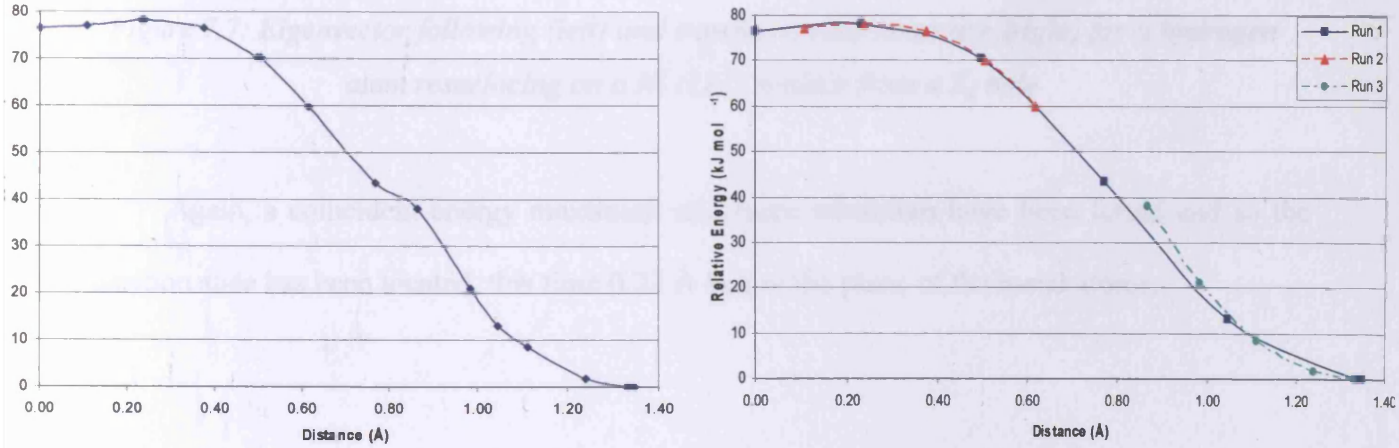

Figure 7.6: Composite (left) and individual (right) NEB calculations for a hydrogen atom resurfacing on a Ni (111) surface from a T_d hole

Fig. 7.6 shows the NEB calculation for the Ni T_d hole – hcp hollow case. In a normal transition state calculation this would be problematic as there is no clearly defined

location for the transition state. However, if we pick one of the two similar points at about 0.24Å reaction coordinate and perform a geometry optimisation there is minimal movement of the hydrogen atom. A frequency calculation obtains vibrational frequencies for the hydrogen atom of 1696cm^{-1} (y-direction), 1691cm^{-1} (x-direction) and *i*-533cm^{-1} (z-direction). We can then use this to perform the eigenvector following in the z-direction (Fig. 7.7).

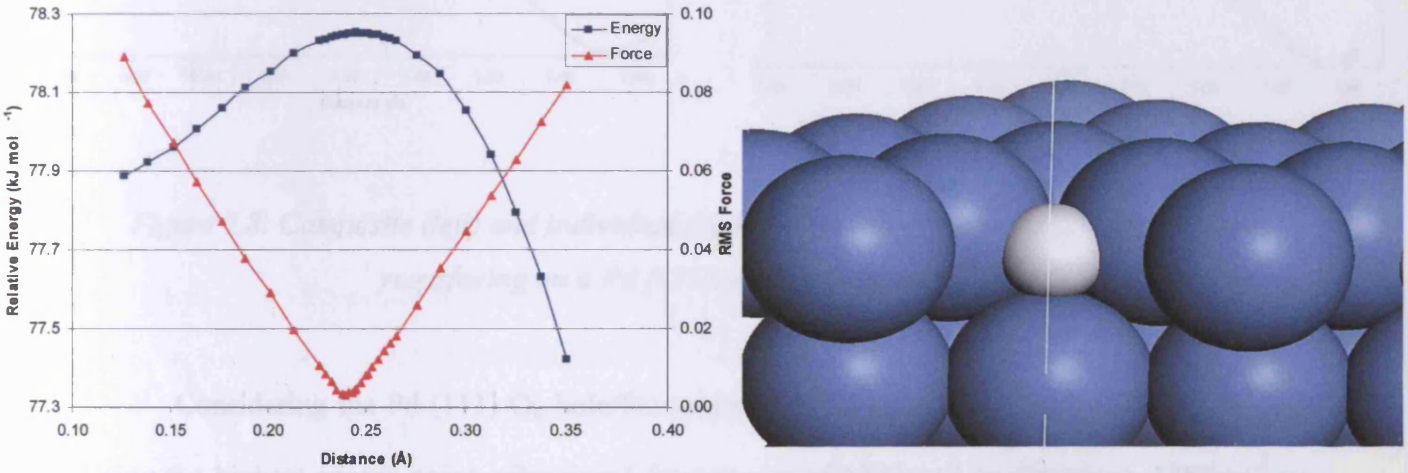

Figure 7.7: Eigenvector following (left) and transition state structure (right) for a hydrogen atom resurfacing on a Ni (111) surface from a T_d hole

Again, a coincident energy maximum and force minimum have been found and so the transition state has been located, this time 0.23 Å below the plane of the metal atoms.

7.3.2 Hydrogen on Pd (111)

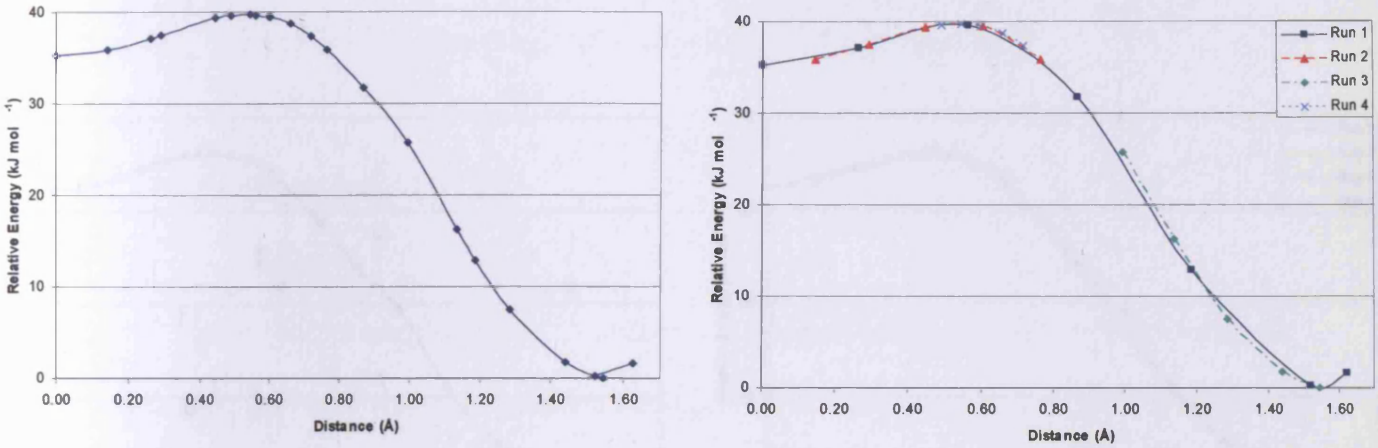

Figure 7.8: Composite (left) and individual (right) NEB calculations for a hydrogen atom resurfacing on a Pd (111) surface from a O_h hole

Considering the Pd (111) O_h hole/fcc system (Fig. 7.8), a broad maximum can be seen. Using the highest energy point, vibrational frequencies of 1383cm^{-1} (y-direction), 1382cm^{-1} (x-direction) and *i*-514cm^{-1} (z-direction) are obtained.

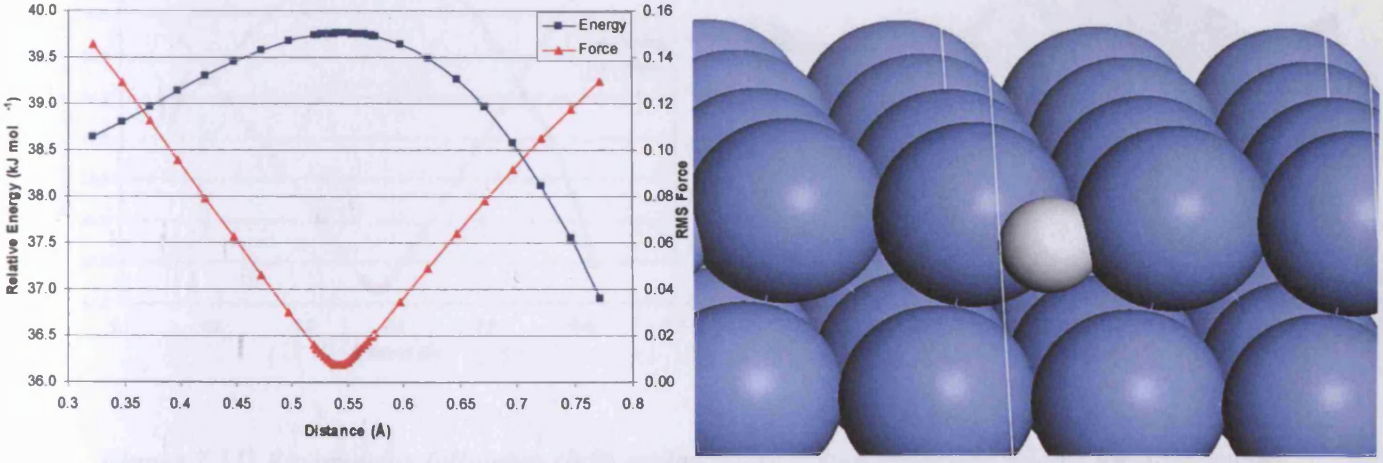

Figure 7.9: Eigenvector following (left) and transition state structure (right) for a hydrogen atom resurfacing on a Pd (111) surface from an O_h hole

An energy plot similar to those observed for Ni has been found, along with a possible transition state. Considering Pd (111), but from a T_d hole (Fig. 7.10):

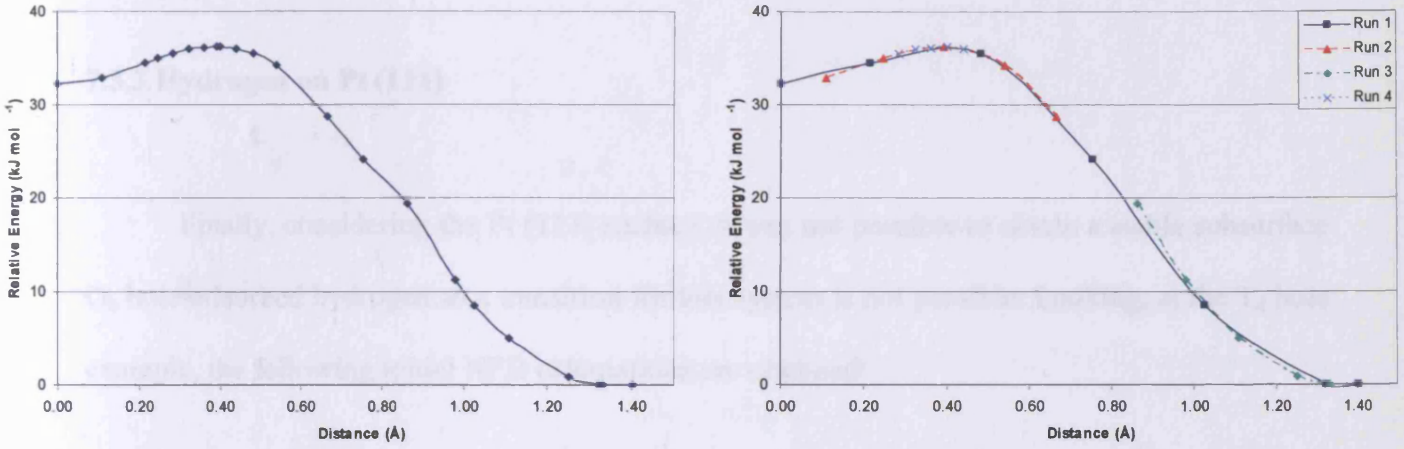

Figure 7.10: Composite (left) and individual (right) NEB calculations for a hydrogen atom resurfacing on a Pd (111) surface from a T_d hole

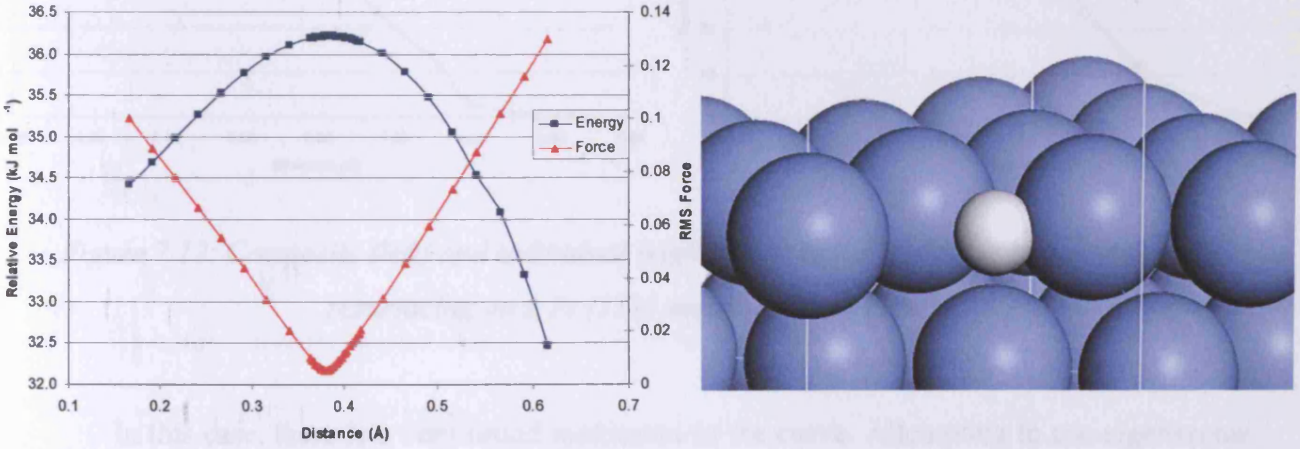

Figure 7.11: Eigenvector following (left) and transition state structure (right) for a hydrogen atom resurfacing on a Pd (111) surface from an T_d hole

The same result has been obtained here as for the O_h hole case. The maximum corresponds to an image with vibrational frequencies of 1442cm^{-1} (y-direction), 1440cm^{-1} (x-direction) and *i*-567cm^{-1} (z-direction) and lead to a possible transition state.

7.3.3 Hydrogen on Pt (111)

Finally, considering the Pt (111) surface, it was not possible to obtain a stable subsurface O_h hole-adsorbed hydrogen so a transition for this system is not possible. Looking, at the T_d hole example, the following initial NEB calculations are obtained:

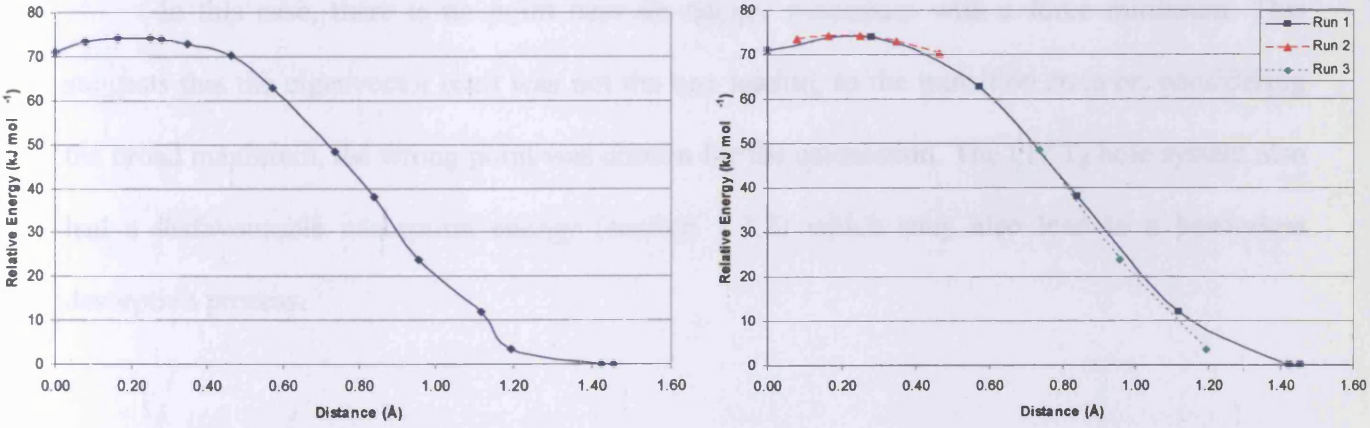

Figure 7.12: Composite (left) and individual (right) NEB calculations for a hydrogen atom resurfacing on a Pt (111) surface from a T_d hole

In this case, there is a very broad maximum to the curve. Attempting to use eigenvector-following at one of the top points yields poor results (Fig. 7.13).

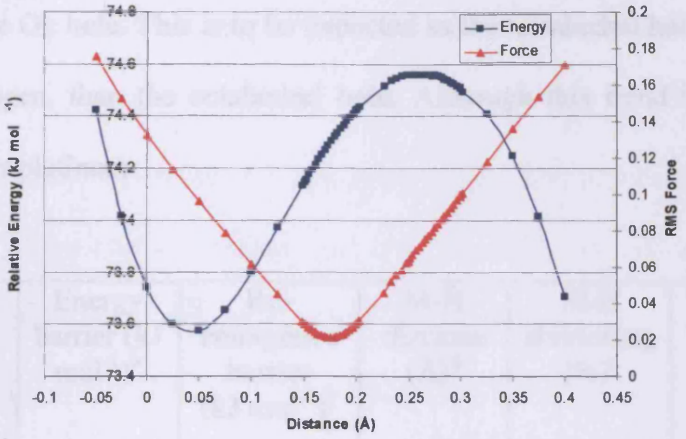

Figure 7.13: Eigenvector following for a hydrogen atom resurfacing on a Pt (111) surface from an T_d hole

In this case, there is no point near an energy maximum with a force minimum. This suggests that the eigenvector used was not the one leading to the transition state or, considering the broad maximum, the wrong point was chosen for the calculation. The Pt / T_d hole system also had a disfavourable adsorption energy (section 5.2.2) which may also lead to a barrierless desorption process.

7.3.4 Analysis

The transition states calculated in the previous sections have been summarised in Table 7.1. A few general conclusions can immediately be drawn. Firstly, palladium has a very much smaller barrier to placing the hydrogen atom below the surface compared to nickel and platinum. This is in agreement with the reputation of palladium as being able to absorb large quantities of hydrogen. There is, however, a relatively low barrier to removing the hydrogen from the subsurface region – this may be of key importance when considering surface hydrogenation

reactions. Looking at the nickel systems, the re-emergence barrier for the T_d hole is much smaller than that for the Oh hole. This is to be expected as the tetrahedral hole is a much smaller cavity, even for hydrogen, than the octahedral hole. Although this trend is not observed for palladium, it may be for platinum.

System	Area increase (%)[a]	Energy barrier (kJ mol^{-1})[b]	Re-emergence barrier (kJ mol^{-1})[c]	M-H distance (Å)[d]	M-H shortening (%)[e]	Imaginary frequency (cm^{-1})[f]	Vertical separation (Å)[g]
Ni O_h-fcc	7.5	80.3	18.8	1.54	9.5	-768	0.18
Ni T_d-hcp	3.0	78.3	1.9	1.54	9.2	-533	0.23
Pd O_h-fcc	4.9	39.8	4.5	1.70	6.5	-514	0.25
Pd T_d-hcp	2.9	36.2	4.0	1.70	6.5	-567	0.16
Pt T_d-hcp*	-	74.6	3.6	-	-	-	-

*Table 7.1: Geometries and energies for calculated transition states for various hydrogen transit subsurface-surface systems. * = not final transition state; 'best guess' structure. a) Increase in area of the triangle defined by three nearest surface metal atoms compared to surface-adsorbed structure. b) Energy barrier for surface-subsurface transition. c) Reverse energy barrier (moving from subsurface to surface adsorption). d) Average M-H distance at transition state. e) Shortening of M-H bond at transition state compared to surface adsorbed state. f) Transition state imaginary frequency. g) Vertical distance between hydrogen atom and plane of metal atoms*

In all cases, the transition state found corresponds to the hydrogen atom being just a small distance (about 0.2Å) below the plane of the surface atoms. This causes the surface atoms to be pushed apart, increasing the area of the surface 'triangle' by about 3-8%. The M-H distances at the transition state show shortening of about 6-9% when compared to surface adsorption, showing the strained nature of the transition state. Looking at the results for the Ni O_h/fcc system, it can be seen that we have fairly good agreement with previous calculations. The re-emergence barrier of 19 kJ mol^{-1} (approximately 0.19eV) is of the correct order of other theoretical calculations (between 0.16-0.18 eV using similar methodology with the VASP

program) [4,5]. The calculated barrier for the surface-subsurface transit (80 kJ mol^{-1}) for Ni O_h/fcc is also in the correct region when compared to the other theoretical calculations (85 kJ mol^{-1}) [6].

Using the methodology in section 7.2, a number of barriers and transition state structures have been calculated which can be rationalised and compared to existing data. However, problems with this methodology can arise when the system lacks a well-defined energy maximum upon which to base the transition state calculation, or when the initial guess structure is far from the transition states. In such systems, only an approximate guess to an energy barrier can be obtained. More accurate initial guesses can be obtained by increasing the number of initial NEB calculations performed; however these are relatively computationally expensive, so a balance must be found between accuracy and calculation time.

7.4 Formaldehyde

Increasing the system size, the next most useful system to consider is formaldehyde. As discussed in section 5.5, formaldehyde on Pt (111) preferentially adsorbs with the C=O bond parallel to the surface; if the C=O bond is perpendicular to the surface, adsorption is less favourable. However, both adsorption modes are viable surface structures and hence the barrier to conversion between them is of importance, especially when considering that the adsorption preference is reversed for acetone (section 5.6).

Initial NEB calculations using the two optimised end-points were repeated until a maximum point could be clearly defined (Fig. 7.14).

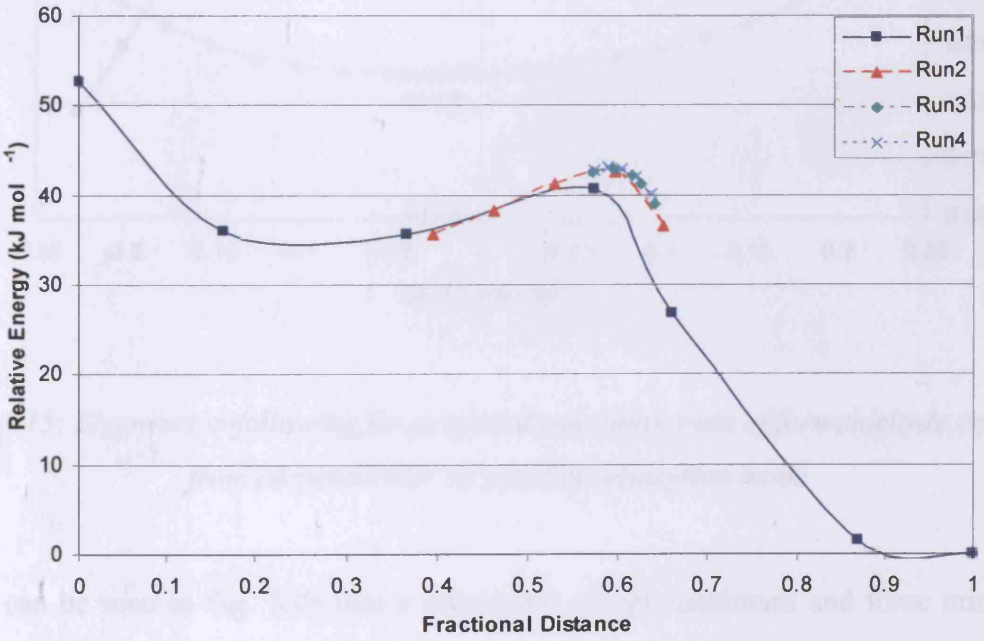

Figure 7.14: Initial NEB calculations for formaldehyde converting from perpendicular (left-hand side) to parallel (right-hand side) adsorption mode.

The maximum obtained from the combined runs suggests an approximate energy barrier of 7 kJ mol^{-1} for the forward process and 42 kJ mol^{-1} for the reverse reaction. The fractional distance quoted on the *x*-axis is calculated using the *inter_vasp* program. Taking the maximum point from the combined runs, the result of the eigenvector-following procedure is shown in Fig. 7.15.

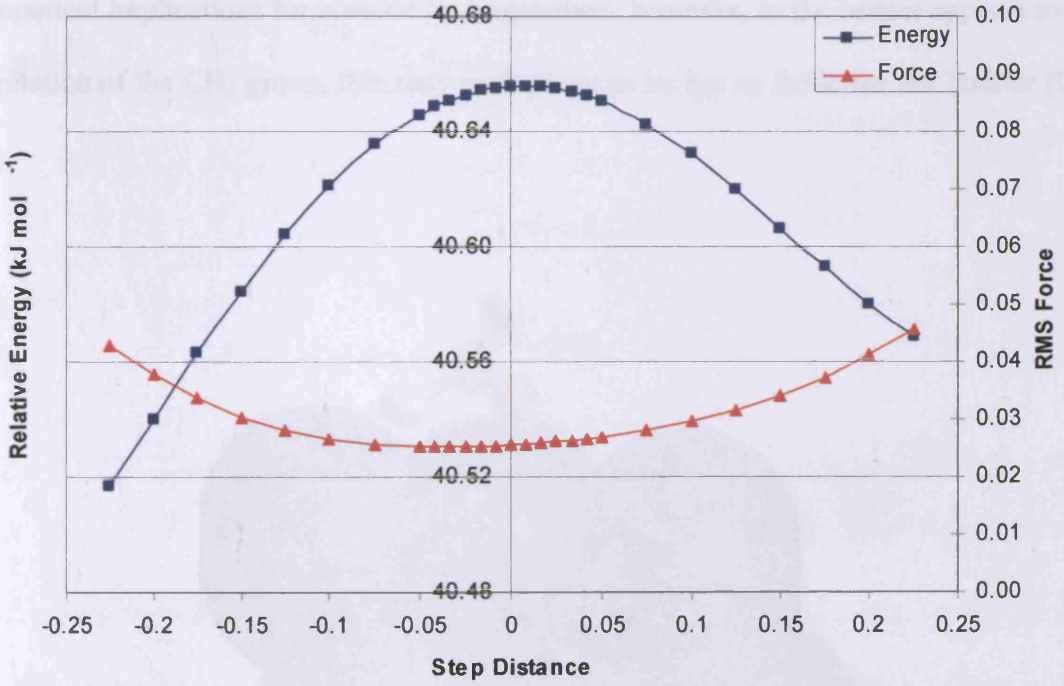

Figure 7.15: Eigenvector-following for proposed transition state of formaldehyde converting from perpendicular to parallel adsorption mode

It can be seen in Fig. 7.15 that a coincident energy maximum and force minimum has been found. This corresponds to a barrier of 5 kJ mol^{-1} for the forward reaction and 41 kJ mol^{-1} for the reverse reaction; the structure of the transition state can be seen in Fig. 7.16. This implies that the barrier to the formaldehyde 'lying down' on the surface is negligible compared to the

reverse reaction, and that most of the formaldehyde present on the surface will be in the parallel configuration. The structure of the transition state suggests that the barrier is due to the rotation of the CH_2 group from a twisted position to lie parallel to the surface. Extending this further, hydrogenation is likely to occur more favourably for the parallel mode (as the bond being hydrogenated is in close proximity to the surface), and the barrier to conversion to this mode (irrespective of what geometry adsorption from the gas-phase produces) is small. This could have important implications for acetone hydrogenation; however, as the barrier appears to be due to the rotation of the CH_2 group, this may well prove to be not as facile for the bulkier $(CH_3)_2C$ moiety.

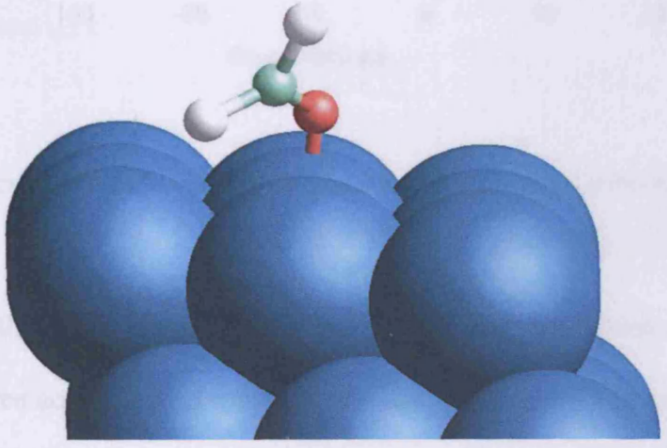

Figure 7.16: Structure of transition state for formaldehyde converting from perpendicular to parallel adsorption mode

The results presented in Figures 7.15 and 7.16 are from four separate, amalgamated, NEB calculations. Whilst this provides acceptable results, it would be preferable to be able to obtain these results using fewer calculations. Therefore, as a test, an attempt will be made to obtain a transition state from the maximum point on the first NEB calculation. The eigenvector following procedure from this is shown in Fig. 7.17.

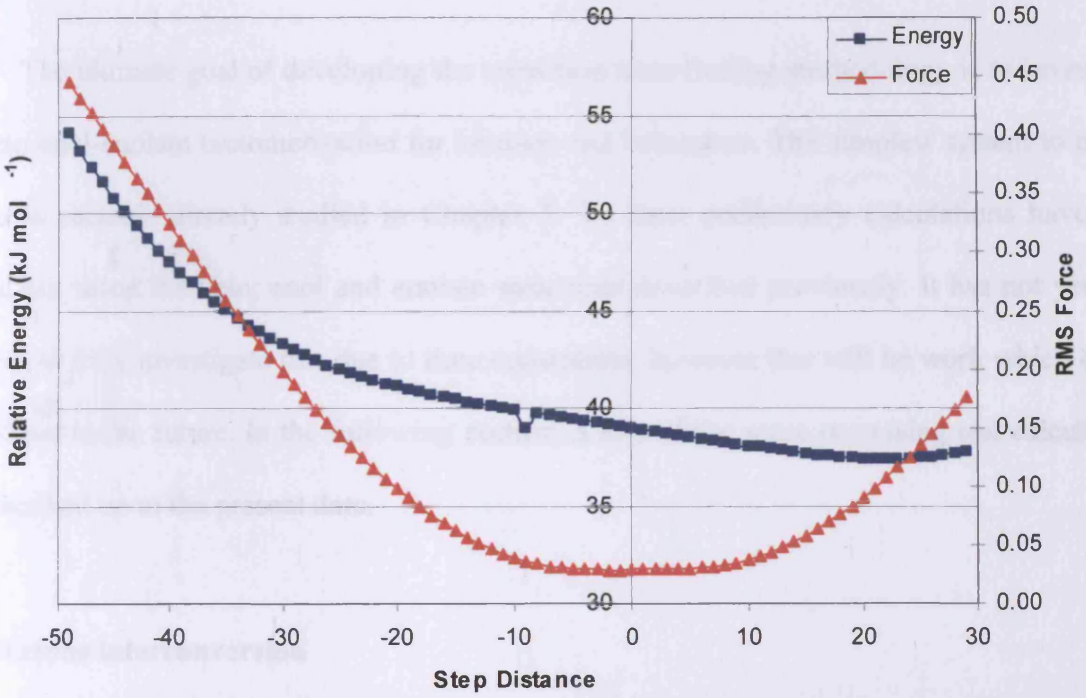

Figure 7.17: Eigenvector-following procedure using only data from run 1 of Fig. 7.15.

It can be seen that there is no longer a coincident force minimum and energy maximum; there is still a large force acting on the system. Therefore, it appears that multiple runs are indeed necessary in order to obtain a satisfactory solution and in order to use the eigenvector following the image must already be reasonably close to the TS.

7.5 Acetone

The ultimate goal of developing the transition state-finding methodology is to investigate the keto-enol-enolate tautomerisation for ketones and ketoesters. The simplest system to extend this to is acetone, already studied in Chapter 5. To date, preliminary calculations have been carried out using the keto, enol and enolate structures described previously. It has not yet been possible to fully investigate this due to time constraints, however this will be work which can be carried out in the future. In the following section, a few of the more promising test calculations are described up to the present date.

7.5.1 Ketone interconversion

The first system which can be investigated is the transition between the two adsorption modes of keto-acetone: η^1 (O) and $\mu_2(C_2,O)$. This is an important step as it has been proved that the η^1 (O) is the more favourable structure and, as the ketone form is considerably more stable in the gas-phase, this will likely be the most prevalent surface structure. However, it is likely to be more difficult for enol and enolate structures to be formed from the η^1 (O) structure (this is also under investigation), so it is possible that an interconversion step is first necessary. The result of the NEB calculation is presented in Fig. 7.18.

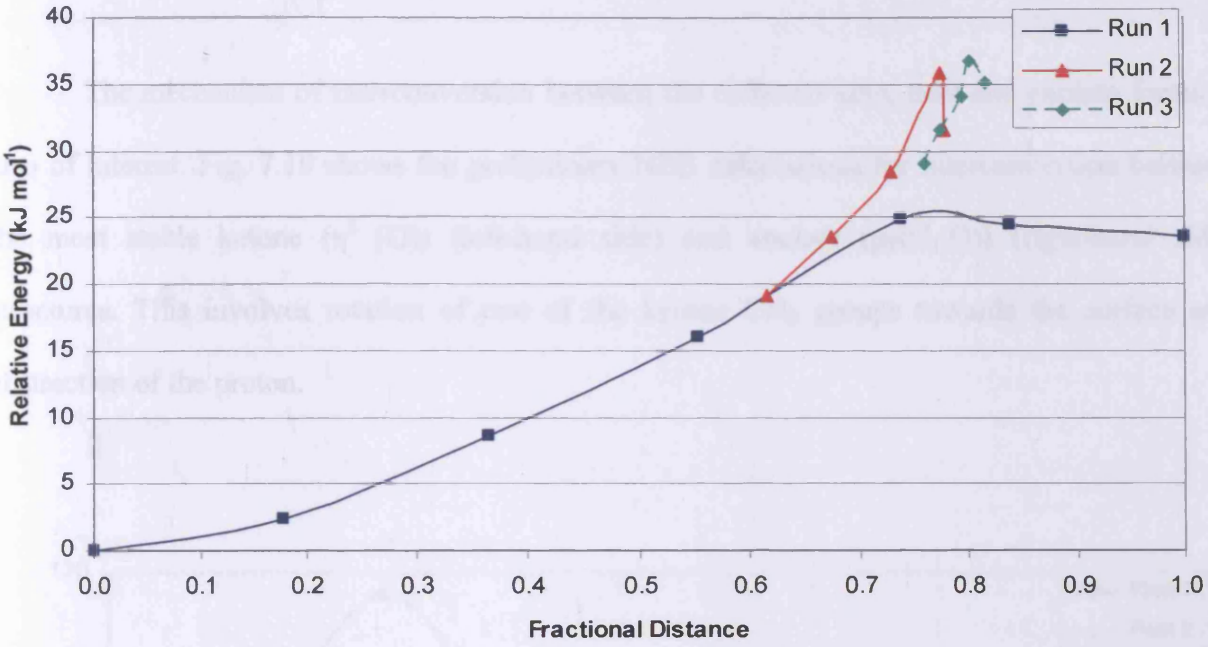

Figure 7.18: Initial NEB calculations for ketone acetone converting from η^1 (O) (perpendicular, left-hand side) to $\mu_2(C_2,O)$ (parallel, right-hand side) adsorption mode.

The picture from Fig. 7.18 is less clear than those seen previously for the other systems under test. The location of any potential transition state is unclear. Further calculations may be necessary in order to refine this. A preliminary guess TS was found by optimising the highest point on the NEB (that from run 3), and a structure which didn't move upon optimisation was found. However, a frequency search upon this structure failed to find a single negative frequency which was of the correct geometry to lead to a potential TS. This point on the NEB path does correspond to the approximate geometry of the expected TS, the bending of the two terminal methyl groups away from the surface (losing the planarity of the molecular backbone) but an exact structure was not located. The approximate barrier of 35 kJ mol^{-1} was reasonable for this system.

7.5.2 Enolate formation

The mechanism of interconversion between the different keto, enol and enolate forms is also of interest. Fig. 7.19 shows the preliminary NEB calculations for interconversion between the most stable ketone (η^1 (O)) (left-hand side) and enolate ($\mu_2(C_1,O)$) (right-hand side) structures. This involves rotation of one of the ketone CH_3 groups towards the surface and abstraction of the proton.

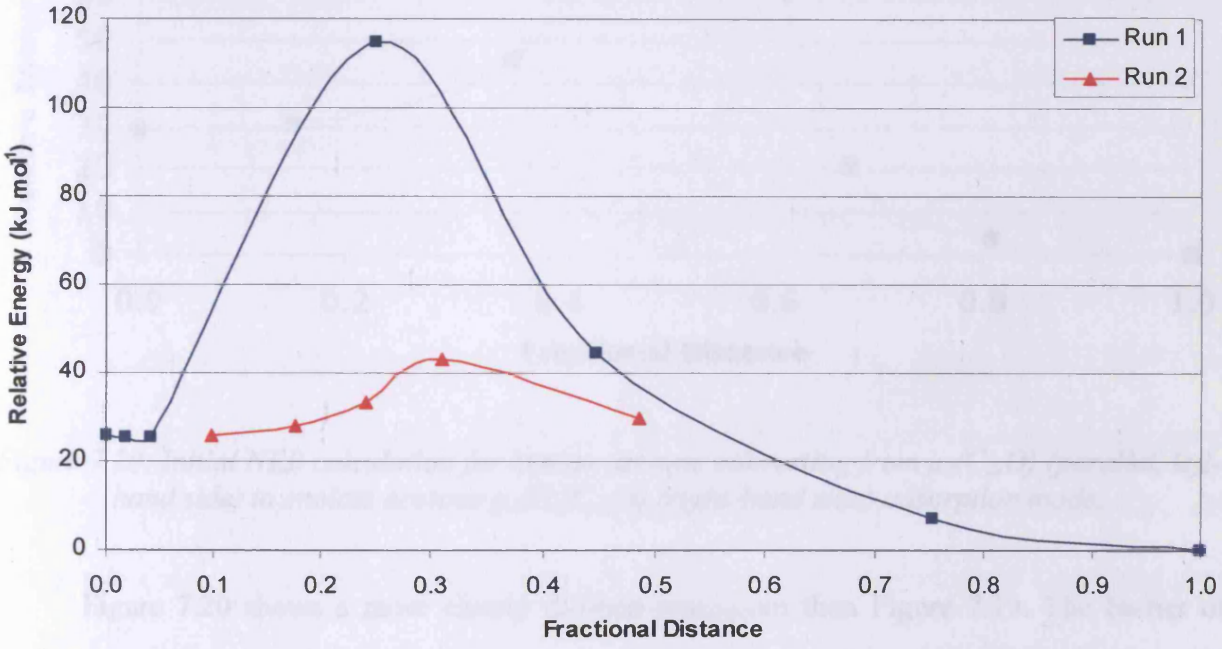

Figure 7.19: Initial NEB calculations for ketone acetone converting from η^1 (O) (perpendicular, left-hand side) to enolate acetone $\mu_2(C_1,O)$ (right-hand side) adsorption mode.

Fig. 7.19 shows a somewhat confusing picture from the TS. It is possible that either a very sharp TS is present (the maximum point from run 1), or that this point is an artifact of the methodology used. Vibrational frequency and optimisation calculations on the absolute maximum point do not yield a structure or frequency which is likely to point towards a possible

transition state. The energy barrier for this structure, approximately 120 kJ mol^{-1} is higher than that seen previously, although perhaps is not unreasonable given that this mechanism involves the breaking of a C-H bond.

Attempting to create the second-most stable enolate, $\mu_3(C_1,C_2,O)$, from the parallel ketone adsorption mode, $\mu_2(C_2,O)$, are shown in Fig. 7.20.

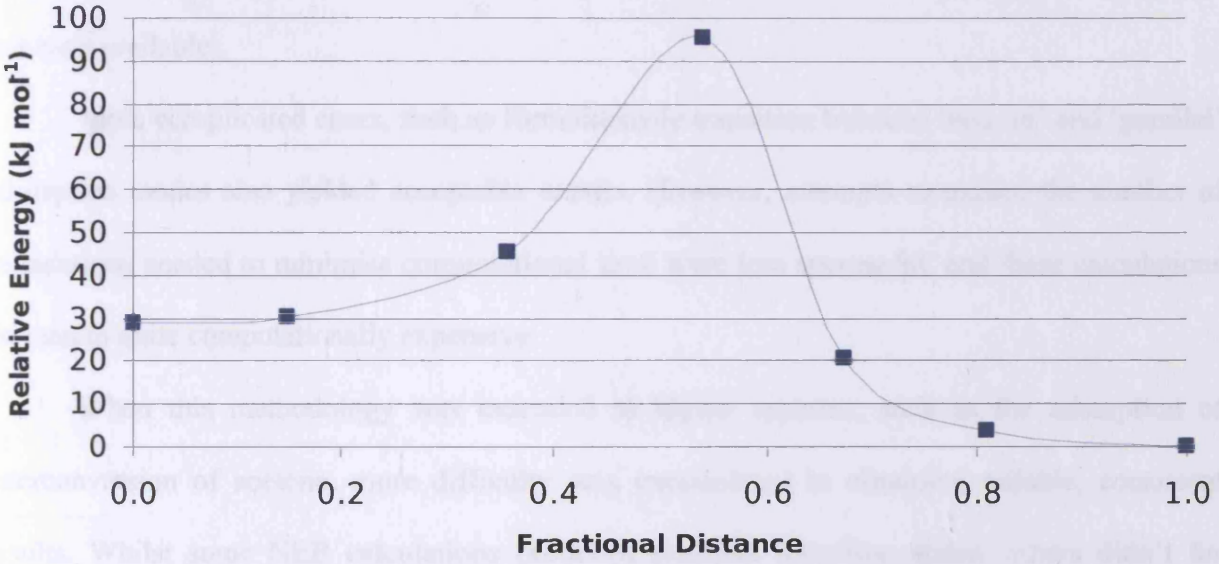

Figure 7.20: Initial NEB calculation for ketone acetone converting from $\mu_2(C_2,O)$ (parallel, left-hand side) to enolate acetone $\mu_3(C_1,C_2,O)$ (right-hand side) adsorption mode.

Figure 7.20 shows a more clearly defined maximum than Figure 7.19. The barrier of nearly 100 kJ mol^{-1} is of the same order as that discussed previously. Work is still continuing on these, and other similar systems, at the present time.

7.6 Conclusions

Work has been carried out to determine a reliable method for calculating transition state structures and reaction barriers for larger periodic systems using the Nudged Elastic Band methodology with eigenvector following. Initial calculations were successfully performed in nearly all cases for the transition of hydrogen between surface and subsurface sites (the simplest test case available).

More complicated cases, such as formaldehyde transition between 'end-on' and 'parallel' adsorption modes also yielded acceptable results. However, attempts to reduce the number of calculations needed to minimise computational time were less successful, and these calculations do remain quite computationally expensive.

When this methodology was extended to bigger systems, such as the adsorption of interconversion of acetone, more difficulty was encountered in obtaining reliable, consistent results. Whilst some NEB calculations produced possible transition states, others didn't for reasons that have yet to be discerned. At the moment this therefore remains quite a 'hit and miss' approach. However, work is continuing in this field of research, so it is hoped that the methodology can be developed further and extended. The use of higher accuracy calculations for the NEB section, in order to 'fine-tune' the calculation, and ways to correct the direction of the eigenvector are currently being examined.

7.7 References

(1) Mills, G.; Jónsson, H.; Schenter, G. K. *Surf. Sci.* **1995**, *324*.
(2) Willock, D. J.; Cardiff University, 2006.
(3) Greeley, J.; Mavrikakis, M. *Surf. Sci.* **2003**, *540*, 215.
(4) Sha, X.; Jackson, B. *Chem. Phys. Lett.* **2002**, *357*, 389.
(5) Ledentu, V.; Dong, W.; Sautet, P. *J. Am. Chem. Soc.* **2000**, *122*, 1796.
(6) Greeley, J.; Mavrikakis, M. *Surf. Sci.* **2003**, *540*, 215.

8. QM/MM modelling of enantioselective hydrogenation

8.1 Introduction

One of the aims of this project is to effectively model the enantioselective hydrogenation of a variety of α-ketoesters. This class of reaction is important as the products can be used in the manufacture of pharmaceuticals. Although such processes can occur through hydrogenation using chiral metal complexes, such as rhodium [1] (reviewed in [2]), there are problems with the stability of such catalysts. Therefore, in 1979, a method was developed in which the asymmetric reduction occurs on a Pt surface modified using a variety of cinchona alkaloids [3] (scheme 8.1). Since this date, this methodology has been applied to a wide variety of systems, as reviewed in [4]. As an example, the hydrogen of methyl pyruvate (MP) and ethyl pyruvate (EP) can be achieved in greater than 95% ee. The system that is most often studied is EP, although MP can be used as an acceptable model compound, and more heavily functionalised derivatives have also been considered experimentally.

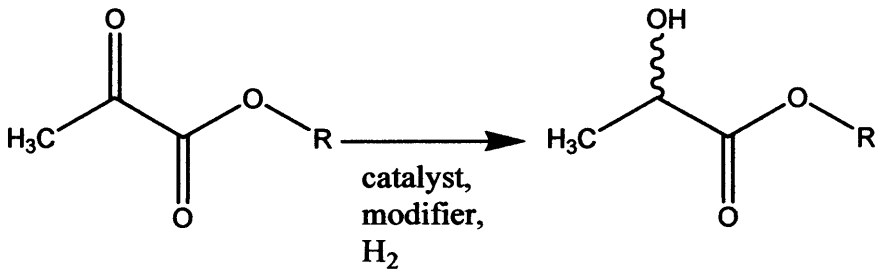

Scheme 8.1: Enantioselective hydrogenation of an α-ketoester.

Several models have been proposed to explain how the modifier-adsorbate-surface system works, with the most commonly accepted being that proposed by the research group of

Baiker [5-7]. In this model, a 1:1 complex is formed between the substrate and modifier mainly by hydrogen bonding between the keto oxygen atom of the substrate and the quinuclidene nitrogen atom of the modifier. In acidic media, this nitrogen atom can be safely assumed to be protonated [8]; for non-acidic media, a "half-hydrogenated" variation of this model has been proposed [6]. In these models the modifier is strongly anchored to the metal surface, and the variation in enantioselectivity occurs mainly through the orientation of the substrate with respect to the surface and modifier. The modifier is usually considered to adsorb with the aromatic ring system parallel to the metal surface [9]. The modifier can exist in several different conformations; under reaction conditions it has been shown that cinchonidine and cinchonine adopt the open(3) conformation, which also experimentally often affords the best ee [10,11]. The open(3) conformation was proven to be the most stable conformer under apolar solvent conditions [10].

The complete catalytic system is particularly problematic to study theoretically. The presence of the substrate, a relatively large chiral modifier and a metal surface makes it difficult to find one acceptable methodology for modelling the system. Due to the previously stated importance of the substrate-modifier interaction, this has been one of the primary areas of study; the metal surface is often simply ignored. For example, in one of the key studies to date, HF calculations with a 6-31G(d,p) basis set were performed using the Gaussian 94 code [12]. The *s-trans* conformer of MP (which is a pro-*R* complex) was found to be the most stable producing a predicted 92% ee, in good agreement with experiment. To represent the substrate interaction with the surface the calculations were performed with the quinoline ring and the backbone of MP constrained to be co-planar. This approach may yield good results for the MP case, but when applied to more complex systems we have found it to be unsuitable.

8.2 Experimental Investigation

Experimental investigations of enantioselective catalysis using cinchona alkaloids have been undertaken within the Hutchings group at Cardiff University. One particular substrate of importance is N-acetyl-dehydrophenylalanine methyl ester (NADPME) (Fig. 8.1).

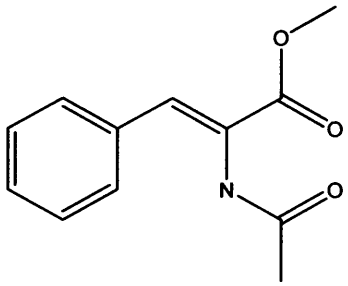

Figure 8.1: N-acetyl-dehydrophenylalanine methyl ester (NADPME)

The hydrogenation of NADPME has been studied using cinchonine as a chiral modifier catalysed by Pd supported on alumina [13]. The observed ee of approximately 30% of the *S*-isomer is significantly lower than that observed for EP (as noted earlier), however this is the first documented observed enantioselectivity for this class of substrates. When performed with cinchonidine instead of cinchonine, the *R*-isomer is preferentially formed; however, as the concentration of modifier is increased, the sense of enantioselectivity changes, leading to enantioinversion [14]. Current efforts are aimed at varying the ratio of NADPME:modifier, solvent polarity and temperature to improve enantioselectivity, although 33% remains the highest ee obtained to date [15]. A further avenue which is being explored is structural modification of the NADPME molecule and the modifier itself. It is hoped that by combining these experimental studies with theoretical modelling, the relatively low ee seen here can be explained, along with the effects of the structural modifications on the ee.

8.3 Gas phase modelling

The structures of both cinchonine and cinchonidine were optimised in the gas phase using B3LYP/6-31G(d,p). The open(3) structure was used in both cases as described in section 8.1. Reoptimisation took place after protonation of the quinuclidene nitrogen, as the reaction proceeds in acidic media, and the optimised structures are presented in Fig. 8.2. The structures of cinchonine and cinchonidine are defined by three principal dihedral angles, and these are presented and compared to those of Baiker [10] in Table 8.1 using the numbering scheme shown in Fig. 8.2. The calculated dihedral angles are in good agreement with those previously observed. The relative position of the quinidine aromatic system and the quinuclidene ring (C3-C4-C9-C8 and C4-C9-C8-N angles) are in close agreement, with a small variation in the torsion angle containing the two hydrogen atoms. Although no comparison data is available for CN, as CN and CD are enantiomers the equivalent negative values are expected from CN.

	Cinchonidine, Baiker [10]	Cinchonidine (calculated)	Cinchonine (calculated)
C3-C4-C9-C8	101.4	99.1	-100.1
C4-C9-C8-N	153.6	153.9	-167.6
H9-C8-C9-H8	-78.3	-75.8	63.3

Table 8.1: Calculated dihedral angles for cinchonidine and cinchonine (B3LYP/6-31G(d,p) in the open(3) conformation, compared to literature standard values. All angles in degrees.

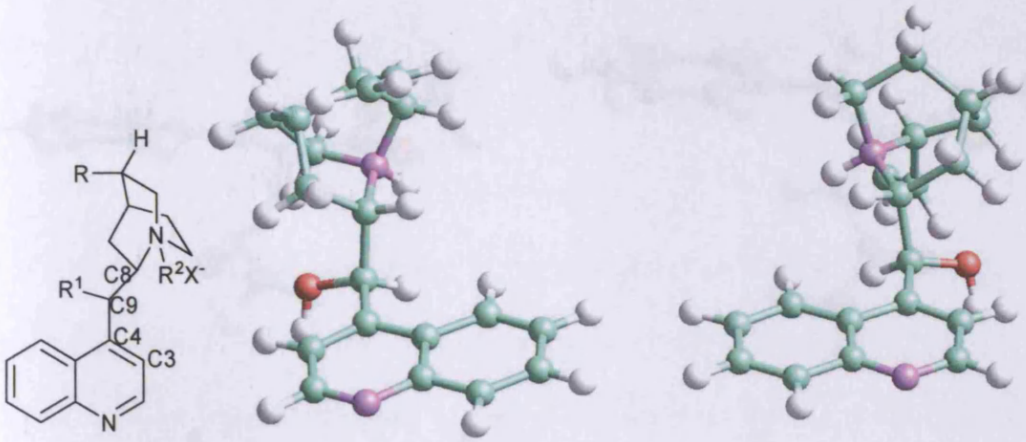

Figure 8.2 : Numbering scheme used for cinchona alkaloids (left) and optimised structures of protonated cinchonidine (middle) and cinchonine (right), open(3) structures

The structures of the two substrates to be considered here were optimised in the gas phase using B3LYP/6-31G(d,p). In the case of NADPME, four distinct gas phase isomers were found to exist (Fig. 8.3). Two types of structure were found, which differed by rotation about the C-N bond placing either the NH or acetyl group over the phenyl ring. The most stable isomer is found to exist when the acetyl moiety of the NADPME molecule is located above the phenyl ring. The alternative configuration, with the NH group above the phenyl ring and the acetyl group pointing away from the body of the molecule is less stable by approximately 10 kJ mol^{-1}. For both of these cases, a mirror image of the isomer is found to exist, created by reflection in the plane of the molecule. As these structures are related by symmetry, in both cases they are isoenergetic. In the gas phase, MP can exist in the s-*cis*- and s-*trans*-conformations. After optimisation, we find that the s-*trans* isomer is favoured by 4 kJ mol^{-1}, in accordance with previous work [16].

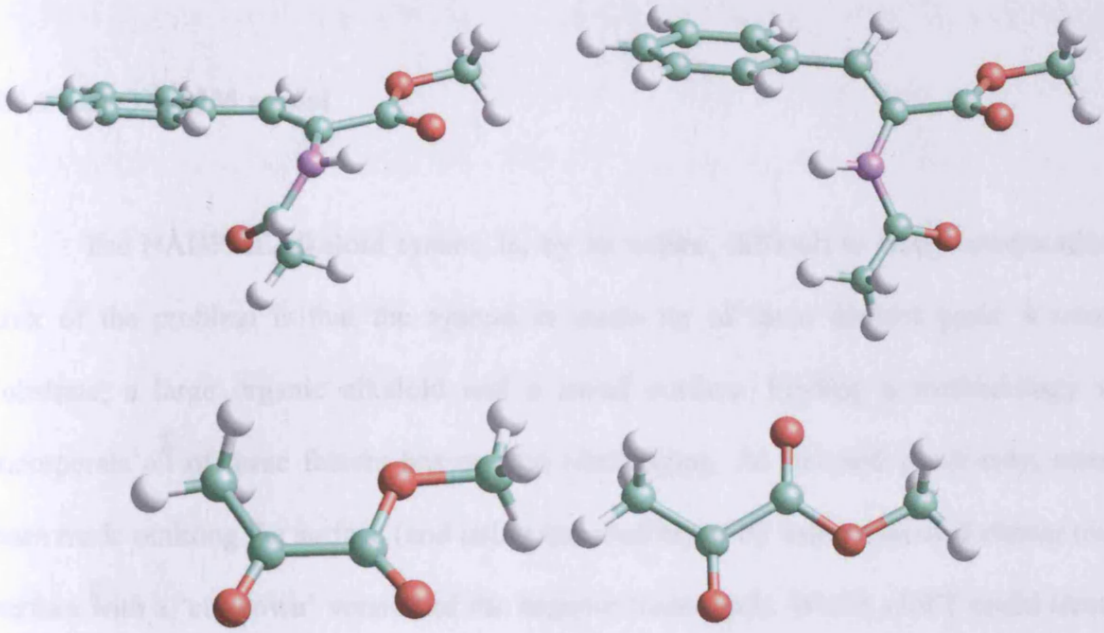

Figure 8.3: Optimised gas phase structures of MP and NADPME. Most stable NADPME (acetyl over phenyl ring) top left, hydrogen over phenyl right top right. MP s-cis form bottom left, s-trans form bottom right.

8.4 QM/MM modelling

8.4.1 The QM/MM model

The NADPME/alkaloid system is, by its nature, difficult to study computationally. The crux of the problem is that the system is made up of three distinct parts; a small organic substrate; a large organic alkaloid and a metal surface. Finding a methodology which can incorporate all of these factors has proved challenging. As detailed previously, attempts have been made omitting the surface (and using constraints) or by using a limited cluster model of the surface with a 'cut-down' version of the organic framework. Whilst pDFT could treat the metal surface very accurately, the organic section would be overly large to fit within a reasonably sized simulation cell. Therefore, we have decided to attempt to apply a different approach to this system.

The NADPME/alkaloid system will be treated using a QM/MM approach, as implemented within Gaussian03 [17], with the ONIOM approach [18-21]. This methodology allows the system to be divided into two parts. A high-level system (the alkaloid and substrate) is modeled at a QM level (using B3LYP/6-31G(d,p)). The metal surface is modelled at a MM level. The choice of potential to be used proved to be problematic. Most forcefield potentials are parameterised primarily for biological applications. Therefore, the metal-organic interaction is suited for a single metal atom interacting with an organic structure, which is not applicable for a surface interaction [22]. The chosen force field is the one primarily implemented within Gaussian, using AMBER potentials [23].

To overcome the problem of the metal-adsorbate forcefield, initial calculations are performed with the metal surface replaced with a sheet of graphite, which is frozen at the optimised bulk-coordinates; all other degrees of freedom in the system are allowed to relax fully.

To test the validity of this system, test calculations were performed adsorbing benzene onto the graphitic surface using this QM/MM methodology. Periodic DFT calculations predict an adsorption energy of benzene on Pt of between 60-120 kJ mol^{-1}, depending on the precise methodology used [24,25]. Using the QM/MM methodology, the calculated adsorption energy was approximately 110 kJ mol^{-1}. Therefore, whilst not an ideal solution to the problem, this methodology is producing acceptable agreement with more accurate approaches. Before it is applied to the unknown NADPME system, however, the methodology will be tested for an interacting system using the cinchonine/MP reaction setup, for which previous computational and experimental data are known. Ultimately, the solution to this problem is to use a set of full quantum simulations on small organic molecules adsorbing on metal surfaces to parameterise our own force field designed specifically for these applications.

8.4.2 The Kinetic Model

The output of the theoretical calculations can give reliable energies regarding the stability of various interacting surface species of substrate/modifier. However, while this enables comparison with other theoretical calculations, available experimental data is usually expressed in terms of ee. Therefore, some kind of kinetic interpretation model is needed to relate the calculated interaction energies to a predicted reaction ee (and hence sense of enantioselectivity).

In order to compare several sets of related structures in which thermal equilibrium populations have been reached, a simple Boltzmann distribution can be used (equation 8.1).

$$\frac{c_i}{c_0} = \exp\left(\frac{-\Delta E_i}{RT}\right) \qquad \text{Eq. 8.1.}$$

Here, c_0 is the relative population of the lowest energy structure, c_i is the relative population of the structure in question (the i^{th} in the set) and ΔE_i the energy difference between the two structures. This equation will predict the relative surface population of each species. In this study, each pair of dimers in the reaction lead to different chiral outcomes and hence their relative populations can be used to predict the ee (equation 8.2):

$$ee = \left\{\frac{(R-S)}{(R+S)}\right\} * 100\% \qquad \text{Eq 8.2}$$

In the case of the substrate/modifier systems, two models can be easily envisaged; the implications of each are discussed below.

In the first model, termed the 'pre-equilibrium model', the substrate (A) and modifier (M) adsorb onto the surface from the gas phase to make an interacting intermediate dimer complex (AM). This is a stable surface species, which can then undergo hydrogenation to the product (P) or decompose before reaction to reform A and M, i.e.

$$A + M \rightleftharpoons AM \rightarrow M + P \qquad \text{Eq 8.3}$$

The AM species reaches equilibrium with the gas phase reactants, so the surface AM species will reach an equilibrium population as defined in equation 8.3 above. Therefore, the stereochemistry of the product formed will be dependant on the relative population of the surface species.

In the second model, the 'reactant-controlled model', the actual hydrogenation process is fast relative to the adsorption event, i.e.

$$A + M \rightarrow AM \rightarrow M + P \qquad \text{Eq 8.4}$$

Here, surface equilibrium of the intermediate dimer complexes is never reached; as soon as the reactants adsorb, the reactant complex is formed and undergoes immediate reaction to form the products. The relative population of the surface dimer species is hence less important, as immediate reaction occurs regardless of the stability of the intermediate species. The enantiosense of the product will hence largely depend on the relative stability of the gas phase species. The enantioselectivity should therefore be weighed by the population of each species in the gas phase.

8.4.3 Test Case: Enantioselective hydrogenation of methyl pyruvate

From a computational point of view, the NADPME/cinchonine system is fundamentally unknown. In order to ensure that the results obtained are valid, it is first necessary to test the methodology, including calculation of predicted ee, against a known system. The simplest example of this is the enantioselective hydrogenation of methyl pyruvate with a cinchonidine modifier. This was studied theoretically, as previously described, by Bürgi and Baiker [12] (which correctly predicted the pro-*R* sense of the enantioselectivity) and experimentally (using an acetic acid solvent) [26], which yielded a 95% ee.

The optimised gas phase structures for MP (see section 8.3) were docked with cinchonidine and the simulation surface to form four possible reaction complex geometries. The *s*-cis- and *s*-trans-isomers can both be docked in a parallel and anti-parallel configuration with respect to the surface, which will yield opposite stereoisomers upon hydrogenation. The pro-*R* and pro-*S* configurations are assigned with the assumption that the source of H for hydrogenation

is from the surface. The calculated energies and geometries for the four reaction complexes are shown in Table 8.2.

Complex	ΔE / kJ mol^{-1}	NH..O hydrogen bonds / Å
s-cis, pro-*R*	0	1.95, 2.45
s-cis, pro-*S*	3	1.95, 2.48
s-trans, pro-*R*	9	1.84
s-trans, pro-*S*	29	1.86

Table 8.2: Calculated energetic and geometric parameters for MP interacting with CD. All energies referenced to the most stable system; pro-R s-cis.

The most stable reactant complex was that of the pro-*R s-cis* geometry, which is 3 kJ mol^{-1} more stable than the pro-*S s-cis complex.* The pro-*R s-trans* geometry is 9 kJ mol^{-1} less stable than pro-*R s-cis*, with the pro-*S s-trans* complex the least stable by a considerable amount.

The optimised geometries for the pair of *s-cis* complexes are shown in Fig. 8.4. In both cases, the interaction between reactant and modifier is primarily via a bifurcated hydrogen bond. The bifurcated bond has a shorter (about 1.95Å) and longer (2.45-2.48Å) N^+-H...O interaction, most likely caused by steric interaction between the terminal methyl group and the phenyl ring. Pro-*R* and pro-*S* geometries are similar, although the slightly increased steric bulk of the pro-*S* ester group compared to the methyl group of the pro-*R* structure in proximity to the quinidine ring system may account for the slight difference in energies.

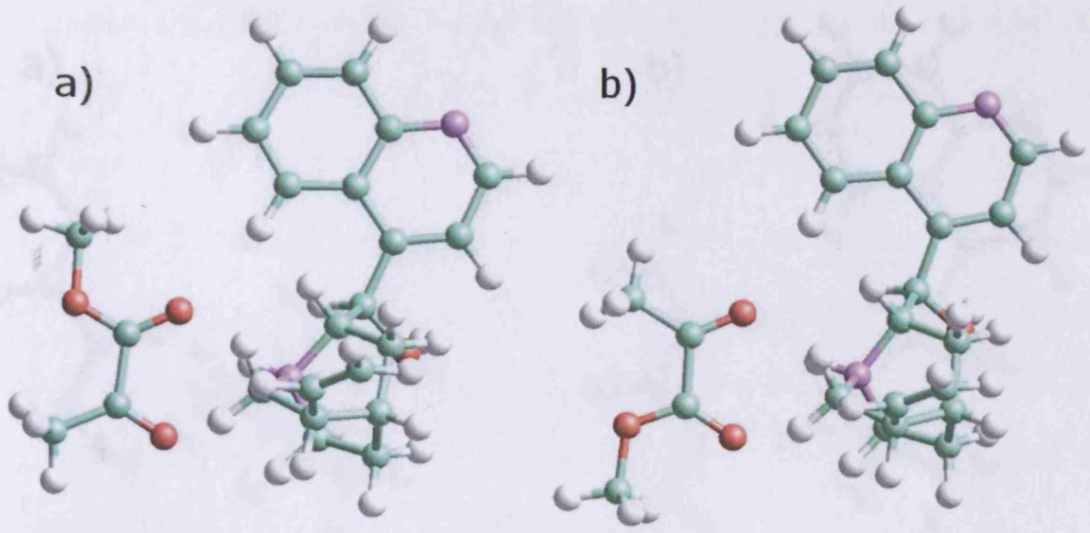

Figure 8.4: Optimised reaction complexes of s-cis-MP and cinchonidine; a) pro-S, b) pro-R. Structures are presented with the surface omitted and viewed from directly above.

The optimised reaction complexes for the *s-trans* isomers are shown in Fig. 8.5. It can be seen that, because of the *s-trans* nature, a bifurcated hydrogen bond is no longer possible, with both complexes exhibiting a single, shorter (than *s-cis*) hydrogen bond (approximately 1.85Å). Except for the single hydrogen bond, the pro-*R* structure exhibits a similar geometry compared to the *s-cis* counterpart. However, the pro-*S* structure shows considerable distortion away from an idealised geometry due to the close proximity of the bulk of the MP molecule and the quinoline ring of the modifier. This accounts for the large energy destabilization of this isomer.

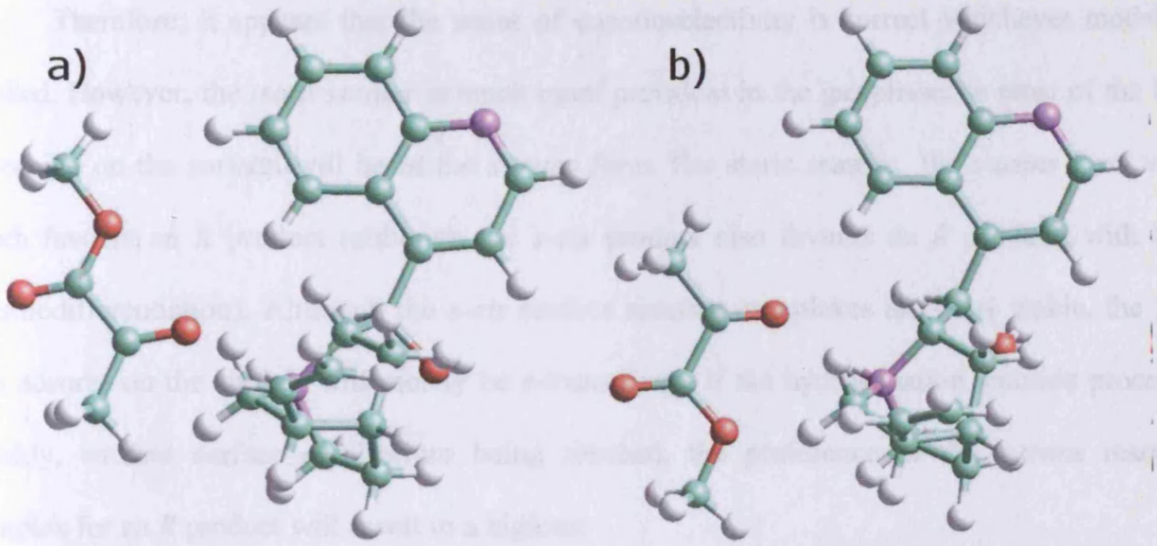

Figure 8.5: Optimised reaction complexes of s-trans-MP and cinchonidine; a) pro-S, b) pro-R. Structures are presented with the surface omitted and viewed from directly above.

Having obtained the optimised geometries and energies of the reactant complex, it is now possible to attempt to predict the ee of the reaction using the two models discussed previously. The relative abundance of the surface species (pro-*R* : pro-*S*) would be 78:22 (s-*cis*) and 100:0 (s-*trans*), assuming a temperature of 298K. If the pre-equilibrium model, as described above, is applied this will result in an equilibrium surface population of 76% pro-*R* *s-cis*, 22% pro-*S* *s-cis* and 2% pro-*R* *s-trans*. Calculating the ee using equation 8.2, the overall reaction ee is 56% in favour of the *R* product. This model therefore correctly predicts the sense of enantioselectivity, although the actual ee is lower than observed experimentally.

If the reactant-controlled model is applied, the surface population is weighted by the gas phase population distribution. As noted earlier, this is approximately 4 kJ mol^{-1} in favour of the *s-trans* isomer which, using a simple Boltzmann distribution, will result in an approximate 6:1 ratio in the gas phase. Weighting the surface population by the 6:1 ratio and recalculating the ee, we obtain an ee of 93% in favour of the *R* product, which is comparable to that observed experimentally.

Therefore, it appears that the sense of enantioselectivity is correct whichever model is applied. However, the *trans* isomer is much more prevalent in the gas phase, so most of the MP adsorbing on the surface will be in the *s-trans* form. For steric reasons, the *s-trans* form very much favours an *R* product (although the *s-cis* product also favours an *R* product, with less enantiodifferentiation). Although the *s-cis* surface reactant complexes are more stable, the MP that adsorbs on the surface will mostly be *s-trans* form; if the hydrogenation reaction proceeds quickly, without surface equilibrium being reached, the preference of the *s-trans* reactant complex for an *R* product will result in a high ee.

8.4.4 Enantioselective hydrogenation of NADPME

Having proved the validity of the methodology using the test case example above, the next step is to apply this to the system to be studied, the enantioselective hydrogenation of NADPME. The gas-phase optimised NADPME molecule was docked with the modifier in a similar fashion to MP; for each structure another was produced in an anti-parallel configuration. As stated previously, interaction between the NADPME and modifier is primarily between the hydrogen of protonated nitrogen of the quinuclidene system and a polar atom on the NADPME molecule. By inspection, there are three possible hydrogen bonding points: the nitrogen, ether (carbonyl) oxygen and amide oxygen of the NADPME. Trial structures were set up using each of these bonding points. Upon optimisation, the hydrogen bond between the proton and nitrogen atom reverted to either one of the carbonyl groups. As will be noted later, optimisation with the surface resulted in a significant flattening of the NADPME molecule, meaning that the choice of gas-phase starting geometry became less important. After all calculations were completed, there were a set of three unique pairs of reactant complexes bonded *via* a carbonyl group or *via* a bifurcated hydrogen bond in a similar fashion to that noted for MP (table 8.3).

Structure and selectivity		Relative Energy (kJ mol^{-1})	Hydrogen bond type	Hydrogen bond length (Å)
A	*R*	0.1	Ester	1.87
	S	0.0	Amide	1.82
B	*R*	15.1	Ester	1.91
	S	7.4	Ester	1.75
C	*R*	15.3	Bifurc.	2.04, 2.20
	S	5.6	Bifurc.	1.97, 2.18

Table 8.3: Optimised geometries and energies of NADPME interacting with the modifier.

The most stable pair of isomers (labeled A in table 8.3) are depicted in figure 8.6. The pro-*R* and pro-*S* isomers are isoenergetic within the accuracy of these calculations, and each exhibit a single H...O hydrogen bond. The pro-*R* isomer has a hydrogen bond to the ester oxygen of 1.87Å and the pro-*S* isomer to the amide oxygen of 1.82 Å. The bonding has changed between ester and amide oxygen in order to minimise repulsion between the NADPME and the phenyl ring of the modifier. One feature which is notable for both structures in the presence of the model surface is a flattening out of the NADPME molecule. The optimised gas-phase structure has a dihedral angle of approximately 50° between the plane of the phenyl group and the main body of the molecule. Upon interaction with the surface, however, this has reduced and the molecule has become almost planar. A side effect of this is that a rough symmetry has been introduced to the molecule. As indicated on figure 8.6, an approximate C_2 rotation axis can be added; although the actual atom types may differ, the shape of the molecule remains the same upon rotation; there is an oxygen atom available for bonding on either side of this axis. Rotation around this axis will convert a pro-*R* isomer into a pro-*S* isomer and *vice versa*. This explains why the two isomers are isoenergetic and will lead to a lack of enantiodifferentiation for this pair of isomers.

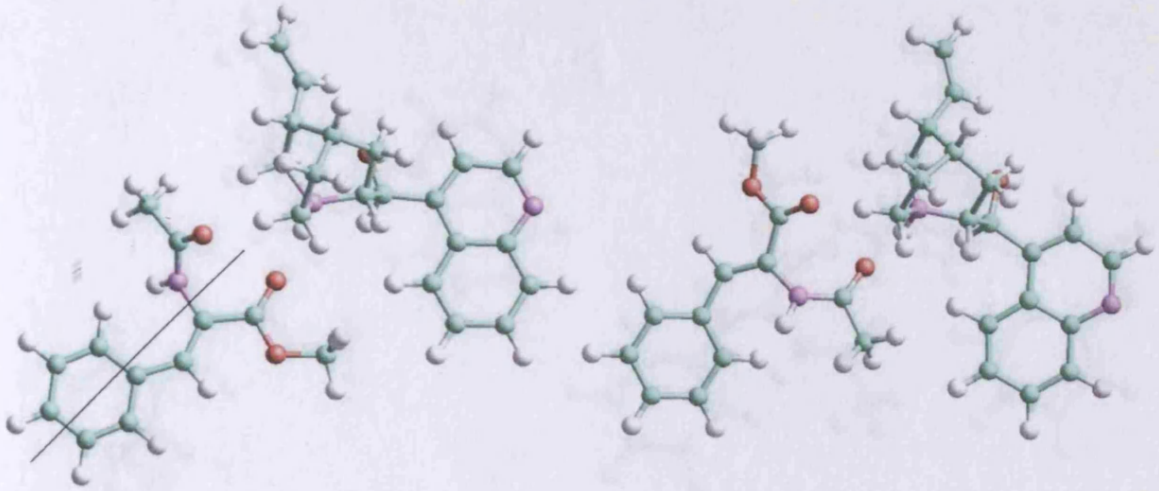

*Fig. 8.6: Optimised structures of the most stable pair of isomers (A) of NADPME interacting with the modifier. Left pro-*R*, right pro-*S*. Solid black line indicates pseudo-C_2 rotation axis (see text). Surface omitted for clarity.*

The next most stable pair of isomers are depicted below in Fig. 8.7. The pro-*S* isomer is structurally similar to that of set A, being slightly displaced with respect to the modifier with a longer 1.91 Å bond between the proton and the ester oxygen atom resulting in a destabilization of 7 kJ mol^{-1} compared to the pro-*R* isomer of set A. The pro-*R* isomer is now bonded *via* the ester oxygen (1.75 Å); this will result in an increase in steric repulsion as can be seen in Fig. 8.7 and results in a significant destabilization of energy of 15 kJ mol^{-1} compared to the most stable structure.

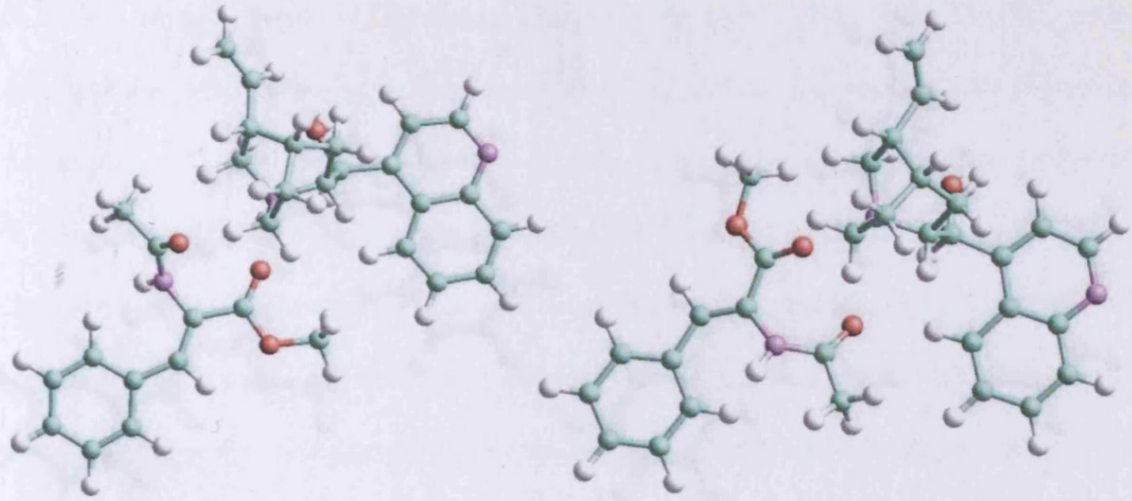

*Fig. 8.7: Optimised structures of isomer set B of NADPME interacting with the modifier. Left pro-*R*, right pro-*S*. Surface omitted for clarity.*

The final pair of structures (figure 8.8) are different in nature to those described above. In this case, both ethyl and amide oxygen are involved in a bifurcated hydrogen bond to the proton, in a similar fashion to that seen for *s-cis*-MP. The pro-*R* isomer is 15 kJ mol^{-1} above the most stable structure, whilst the pro-*S* is 5 kJ mol^{-1} higher. The pro-*R* isomer is destabilized by the unfavourable interaction with the phenyl group. In general, the bifurcated bond forces a less favourable geometry as there is a reduced ability to avoid steric interactions with the quinidine group.

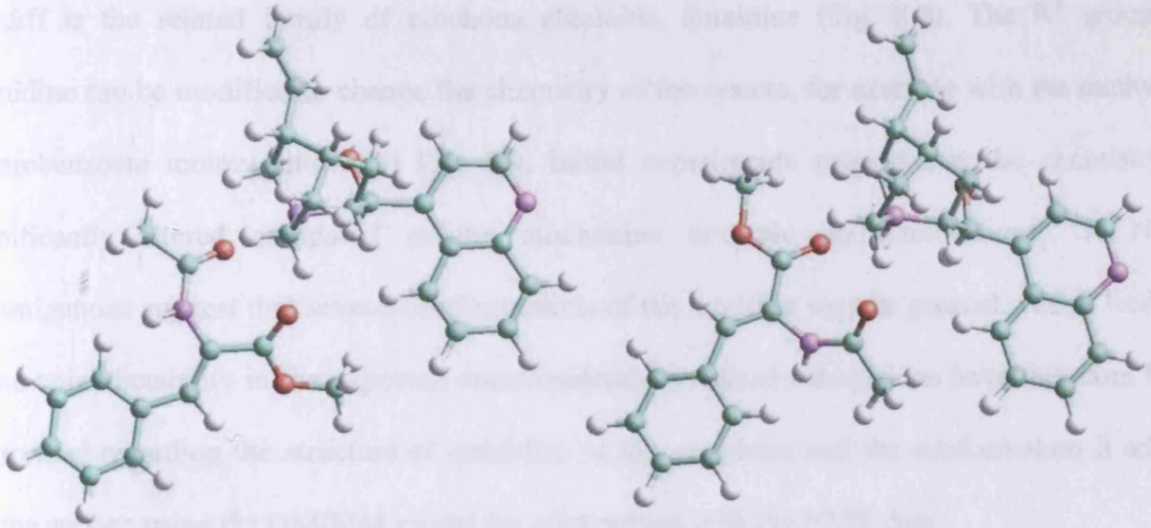

*Fig. 8.8: Optimised structures of isomer set C of NADPME interacting with the modifier. Left pro-*R*, right pro-*S*. Surface omitted for clarity.*

It is now necessary to calculate the predicted ee by applying the two kinetic models discussed previously. Applying the pre-equilibrium model, the predicted equilibrium surface population will be to be 47% pro-*S*-A, 46% pro-*R*-A, 5% pro-*S*-C and 2% pro-*S*-B (i.e. 54% pro-*S* and 46% pro-*R*). Calculating the ee, a value of 9% pro-*S* is obtained. Applying the reactant-control model is slightly more complex in this case because of the similar starting structures, but after weighting the predicted ee is around 12%. The experimental ee for this system under these conditions is 9-10% [15]. Thus, within the accuracy of these calculations, either model provides a result in approximate agreement with the experimentally calculated ee.

8.4.5 Quinidine-based systems

After investigation of the modifier-reactant interaction, one of the next logical stages is to investigate the effect of structural modification of the alkaloid modifier itself. As shown previously, cinchonidine is unlikely to give good ee for the hydrogenation of NADPME, so different modifiers are needed. One alternative which is being considered experimentally in

Cardiff is the related family of cinchona alkaloids, quinidine (Fig. 8.9). The R^1 group of quinidine can be modified to change the chemistry of the system, for example with the methyl 4-chlorobenzoate moiety shown in Fig. 8.9. Initial experiments suggest that the chemistry is significantly altered compared to the cinchonine example discussed above. ^1H NMR investigations suggest that several conformations of the modifier may be present, which leads to some unpredictability in the expected enantioselectivity. Initial calculations have therefore been performed regarding the structure of quinidine in the gas-phase and the conformation it adopts on the surface using the QM/MM model for comparison with the NMR data.

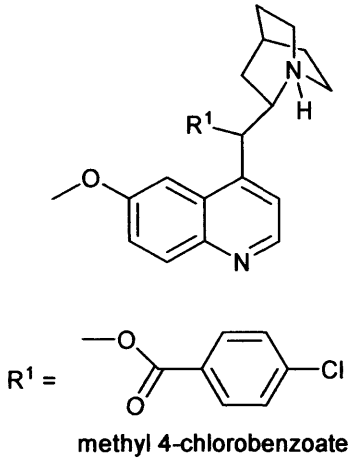

Fig. 8.9: The structure of the quinidine-based molecule (R^1 = OH) and the methyl 4-chlorobenzoate variation used for this study

The structure of quinidine was optimised in the gas phase at the B3LYP/6-31G(d,p) level. A scan was then performed at the HF level of theory, using 18 steps of 20 degrees to rotate around the C_4-C_9-C_8-N dihedral (using the labelling system defined in Fig. 8.2) for both unprotonated and protonated quinidine (to account for possible solvent effects). This rotates the quinuclidine group relative to the aromatic system. The candidate structures from the minima of this scan were then docked onto the surface and optimised using the same QM/MM methodology as described earlier.

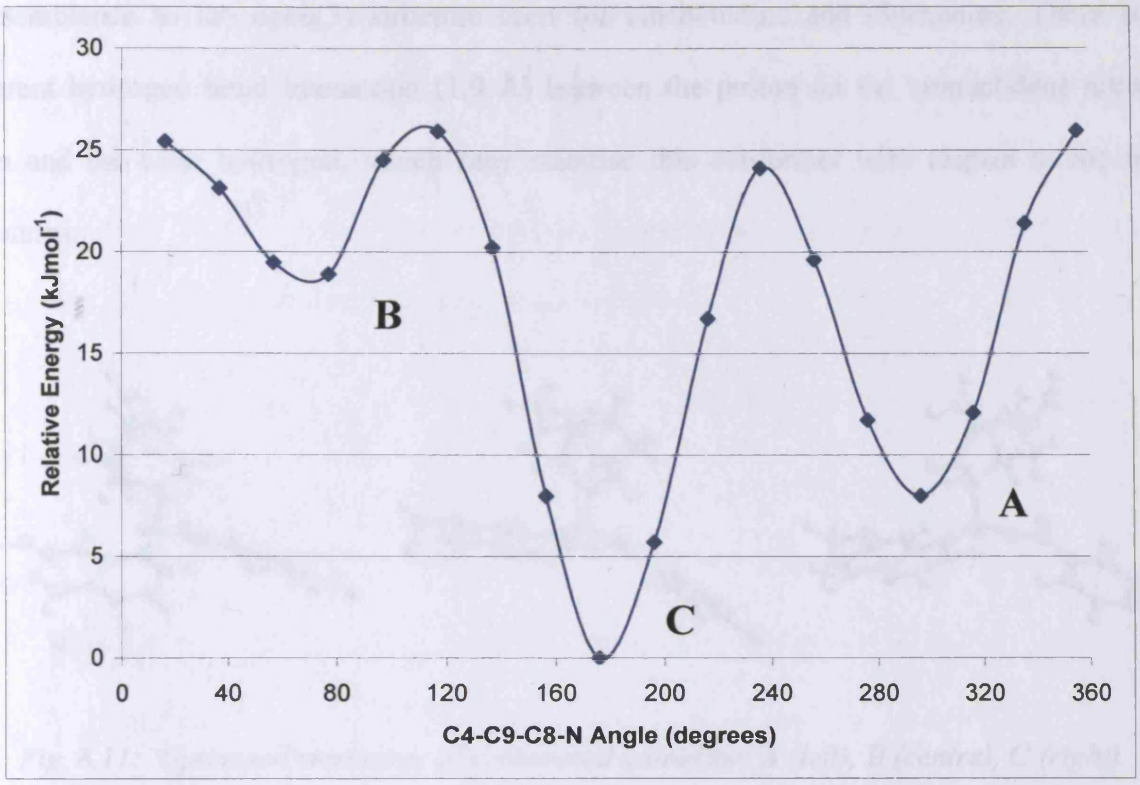

Fig. 8.10: The scan of the C_4-C_9-C_8-N dihedral angle for protonated quinidine in the gas phase

The results of the dihedral scan for protonated quinidine are presented in Fig. 8.10. Three minima are easily identifiable, and these were re-optimised at a higher theory level as described above. The optimised geometries and energies are shown in Table 8.4 and the structures in Fig. 8.11.

Structure	Relative energy (kJ mol^{-1})	Type	C3-C4-C8-C9 (°)	C4-C9-C8-N (°)	H-C-C-H (°)
A	11.3	Closed	-85.6	-70.1	167.4
B	18.1	Open	-95.4	76.7	-49.2
C	0.0	Open	-99.4	175.5	47.4

Table 8.4: Optimised energies and geometries for protonated quinidine.

Considering the data and the structures shown here, there is a clear preference for structure C. This is an open structure and both visually, and in terms of the dihedral angles, bears

a resemblance to the open(3) structure seen for cinchonidine and cinchonine. There is an apparent hydrogen bond interaction (1.9 Å) between the proton on the quinuclidene nitrogen atom and the ester hydrogen, which may stabilise this conformer with respect to the other structures.

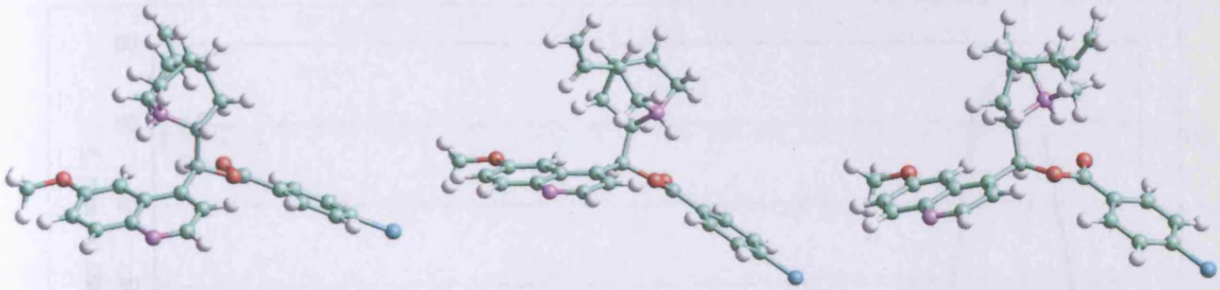

Fig. 8.11: Optimised structures of protonated quinidine; A (left), B (centre), C (right).

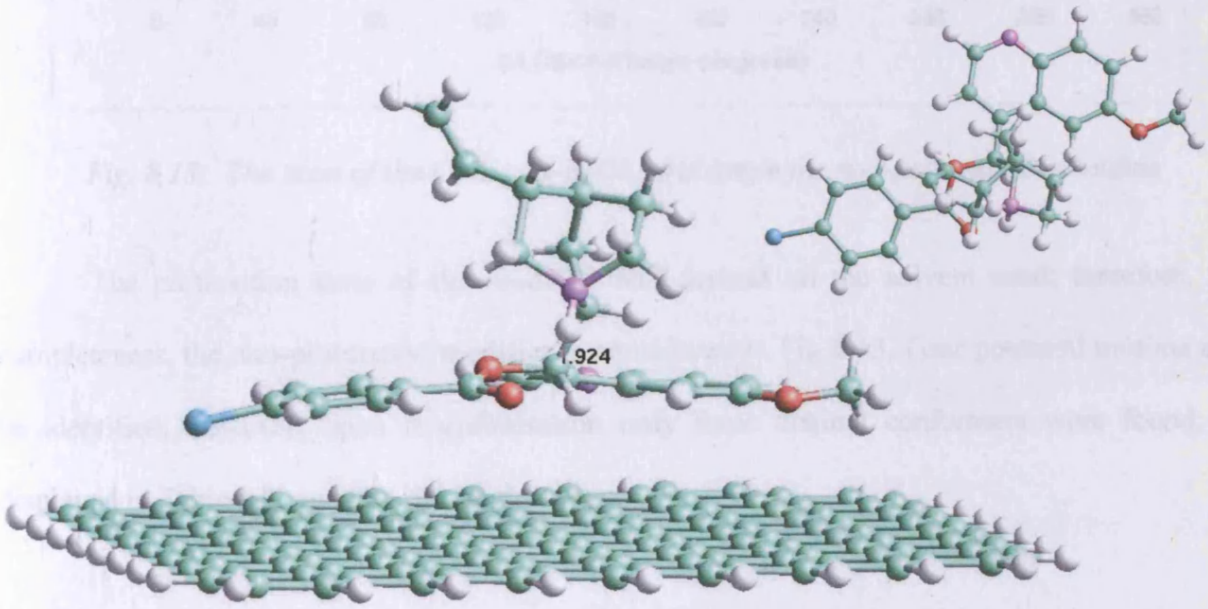

Fig. 8.12: The most stable conformer of protonated quinidine after optimisation with the surface present (inset: plan view with surface omitted for clarity).

Fig. 8.12 shows the structure of the most stable (conformer C) protonated quinidine structure after optimisation using the QM/MM methodology with the surface present. There is

little distortion from the gas-phase geometry, and the two aromatic ring systems of the quinidine have adsorbed parallel to the surface. Looking at the plan view of the system, it is possible to speculate that interaction with this modifier could be more difficult than with either cinchonine or cinchonidine. The location of the methyl 4-chlorobenzoate moiety may result in increased steric interaction with another molecule such as NADPME.

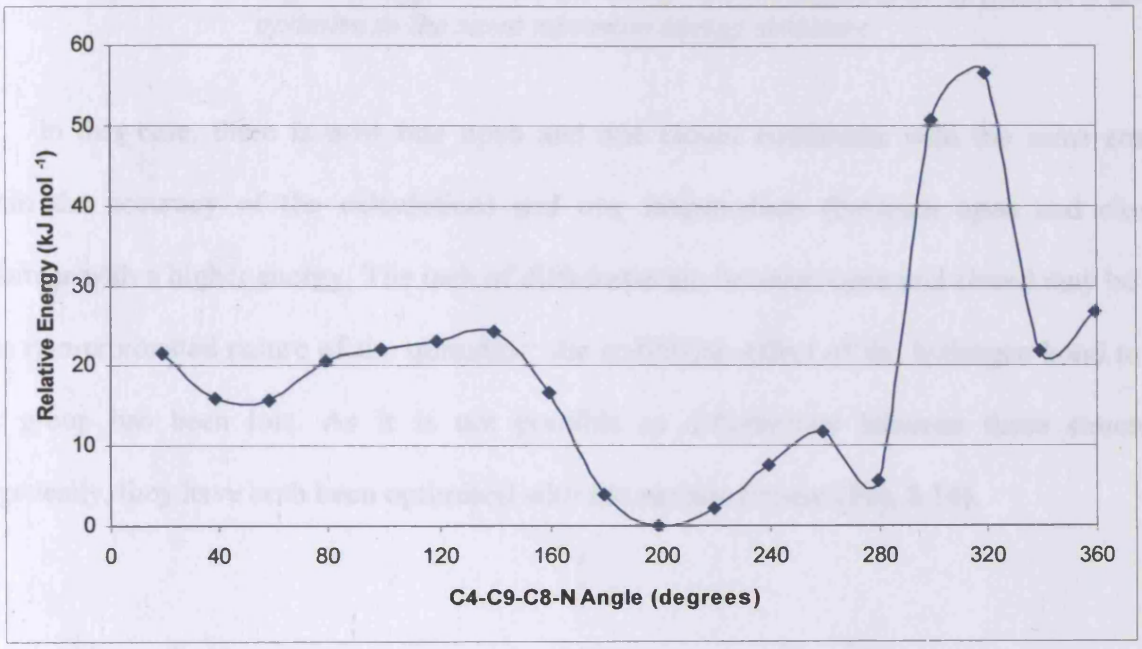

Fig. 8.13: The scan of the C_4-C_9-C_8-N dihedral angle for non-protonated quinidine

The protonation state of the modifier will depend on the solvent used; therefore, for completeness, the non-protonated modifier is considered in Fig 8.13. Four potential minima can be identified; however, upon re-optimisation only three distinct conformers were found, as displayed in Table 8.5. and Fig. 8.14 below.

Structure	Relative energy (kJ mol^{-1})	Type	C3-C4-C8-C9 (°)	C4-C9-C8-N (°)	H-C-C-H (°)
A / D	11.5	Closed/open	-83.3	53.0	-68.0
B	0.0	Open	-99.9	-158.8	74.8
C	1.2	Closed	-65.7	-59.7	-179.3

Table 8.5: Optimised energies and geometries for non-protonated quinidine. Structures A and D optimise to the same minimum energy structure.

In this case, there is now one open and one closed conformer with the same energy (within the accuracy of the calculation) and one intermediate (between open and closed) conformer with a higher energy. The lack of differentiation between open and closed may be due to the non-protonated nature of the quinidine; the stabilising effect of the hydrogen bond to the ester group has been lost. As it is not possible to differentiate between these structures energetically, they have both been optimised with the surface present (Fig. 8.14).

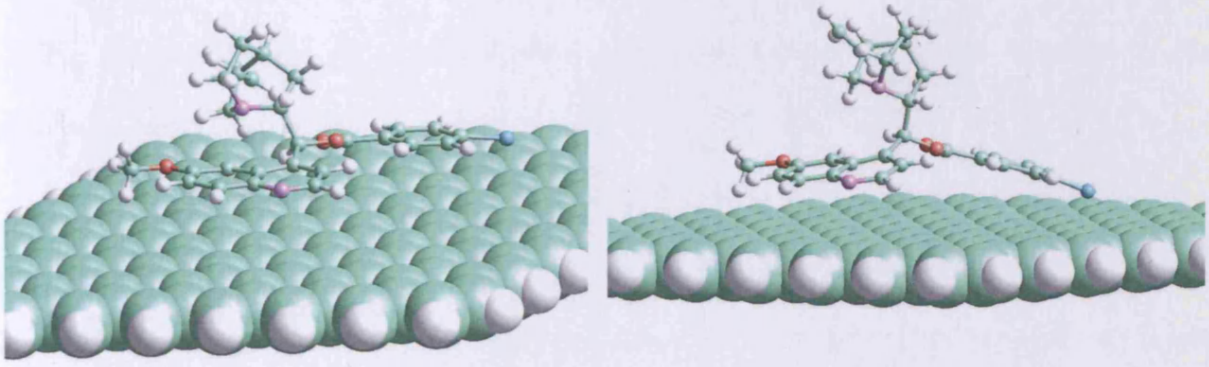

Fig 8.14.: The two most stable structures of non-protonated quinidine; conformer B (left) and conformer C (right)

Neither of the structures dock as neatly with the surface as the protonated structure shown above. However, structure C distorts less upon interaction with the surface; structure A shows considerable distortion towards a more closed structure. This is reflected in the relative energy; the closed structure (C) is approximately 30 kJ mol^{-1} more stable than the optimised

open structure (B). This may suggest that the closed form might be more prevalent on the surface for the non-protonated species.

This apparent reversal of stable conformer (open for protonated and closed for non-protonated) may well predict some of the solvent effects which are observed experimentally for these type of systems. Further investigation is now needed to find valid adsorbate/modifier surface species in order to perform the kinetic analysis to predict an ee as seen previously for the cinchonine/MP system.

8.5 Conclusions

A QM/MM scheme has been applied to several α-ketoester enantioselective hydrogenation schemes. Initial calculations have been performed using a graphite surface in place of the metal surface in order to use currently available potentials. A test case involving the enantioselective hydrogenation of methyl pyruvate yielded a predicted ee in good agreement with experiment and previous theoretical calculations. This was then extended to the hydrogenation of NADPME which has been studied experimentally at Cardiff. The predicated ee was again in good agreement with the experimental value. The low ee in this system can possibly be explained in terms of the planarity of the NADPME upon adsorption. In the dimer formed with the modifier the opposite enantio-sense can be obtained by rotation about a pseudo C_2-rotation axis to give an iso-energetic low energy structure. It can be hypothesised that the introduction of a bulky group to one side of the NADPME side chain will disrupt this symmetry and could possibly alter the ee seen for this system. Finally, calculations have been performed altering the structure of the modifier; this may affect the ability of the substrate to dock effectively with the modifier.

All of the work performed in this chapter assumes the use of the dimer model, as described in Chapter 2. This assumes interaction of the ketone form of the substrate with the modifier. However, as suggested in Chapters 5 and 6, the enol and enolate form of the substrate are possibly thermodynamically more favourable on the surface. It is therefore necessary to consider the role that the substrate enol and enolate forms may play. However, to date this is not yet known as the kinetic barriers to interconversion between the ketone and enol and enolate forms have yet to be calculated. Additionally, the presence of the modifier may affect the relative stabilities of the surface-bound substrate.

The QM/MM model implemented here provides acceptable results for the two modifier/substrate systems tested. Further refinement is now needed to improve the quality of the potentials describing the interaction between the adsorbates and the surface. Periodic-DFT calculations could be used to provide data to fit potentials to in order to obtain a useable forcefield.

8.6 References

(1) Knowles, W. S.; Sabacky, M. J.; Vineyard, B. D.; Weinkauff, D. J. *J. Am. Chem. Soc.* **1975**, *97*, 2567.
(2) Nagel, U.; Albrecht, J. *Top. Catal.* **1998**, *5*, 3.
(3) Orito, Y.; Imai, S.; Nguyen, G. *Synth. Org. Chem. Jpn.* **1979**, *37*, 173.
(4) Blaser, H. U.; Jalett, H. P.; Müller, M.; Studer, M. *Catal. Today* **1997**, *37*, 441.
(5) Schwalm, O.; Minder, B.; Weber, J.; Baiker, A. *Catal. Lett.* **1994**, *23*, 271.
(6) Baiker, A. *J. Mol. Catal. A: Chem.* **1997**, *115*, 473.
(7) Haug, K. L.; Bürgi, T.; Trautman, T. R.; Ceyer, S. T. *J. Am. Chem. Soc.* **1998**, *120*, 8885.
(8) Minder, B.; Mallat, T.; Skrabal, P.; Baiker, A. *Catal. Lett.* **1994**, *29*, 115.
(9) Evans, T.; Woodhead, A. P.; Gutierrez-Soza, A.; Thornton, G.; Hall, T. J.; Davis, A. A.; Young, N. A.; Wells, P. B.; Oldman, R. J.; Plashkevych, O.; Vahtras, O.; Agren, H.; Carravetta, V. *Surf. Sci.* **1999**, *436*, L691.
(10) Bürgi, T.; Baiker, A. *J. Am. Chem. Soc.* **1998**, *120*, 12920.
(11) Bartok, M.; Felföldi, K.; Szöllösi, G.; Bartok, T. *Catal. Lett.* **1999**, *61*, 1.
(12) Bürgi, T.; Baiker, A. *J. Catal.* **2000**, *194*, 445.
(13) Coulston, N. J.; Wells, R. P. K.; Wells, P. B.; Hutchings, G. J. *Catal. Today* **2006**, *114*, 353.
(14) Coulston, N. J.; Wells, R. P. K.; Wells, P. B.; Hutchings, G. J. *Catal. Lett.* **2005**, *103*, 117.
(15) Coulston, N. J.; Jeffery, E. L.; Wells, R. P. K.; McMorn, P.; Wells, P. B.; Willock, D. J.; Hutchings, G. J. *J. Catal.* **2006**, *243*, 360.
(16) Hutchings, G. J.; Willock, D. J. *Top. Catal.* **1998**, *5*.
(17) Frisch, M. J.; Trucks, G. W.; Schlegel, H. B.; Scuseria, G. E.; Robb, M. A.; Cheeseman, J. R.; Montgomery, J., J. A.; Vreven, T.; Kudin, K. N.; Burant, J. C.; Millam, J. M.; Iyengar, S. S.; Tomasi, J.; Barone, V.; Mennucci, B.; Cossi, M.; Scalmani, G.; Rega, N.; Petersson, G. A.; Nakatsuji, H.; Hada, M.; Ehara, M.; Toyota, K.; Fukuda, R.; Hasegawa, J.; Ishida, M.; Nakajima, T.; Honda, Y.; Kitao, O.; Nakai, H.; Klene, M.; Li, X.; Knox, J. E.; Hratchian, H. P.; Cross, J. B.; Bakken, V.; Adamo, C.; Jaramillo, J.; Gomperts, R.; Stratmann, R. E.; Yazyev, O.; Austin, A. J.; Cammi, R.; Pomelli, C.; Ochterski, J. W.; Ayala, P. Y.; Morokuma, K.; Voth, G. A.; Salvador, P.; Dannenberg, J. J.; Zakrzewski, V. G.; Dapprich, S.; Daniels, A. D.; Strain, M. C.; Farkas, O.; Malick, D. K.; Rabuck, A. D.; Raghavachari, K.; Foresman, J. B.; Ortiz, J. V.; Cui, Q.; Baboul, A. G.; Clifford, S.; Cioslowski, J.; Stefanov, B. B.; Liu, G.; Liashenko, A.; Piskorz, P.; Komaromi, I.; Martin, R. L.; Fox, D. J.; Keith, T.; Al-Laham, M. A.; Peng, C. Y.; Nanayakkara, A.; Challacombe, M.; Gill, P. M. W.; Johnson, B.; Chen, W.; Wong, M. W.; Gonzalez, C.; Pople, J. A.: Gaussian, Inc., Wallingford CT, 2004.
(18) Maseras, F.; Morokuma, K. *J. Comput. Chem.* **1995**, *16*, 1170.
(19) Matsubara, T.; Sieber, S.; Morokuma, K. *Int. J. Quantum Chem.* **1996**, *60*, 1101.
(20) Svensson, M.; Humbel, S.; Froese, R. D. J.; Matsubara, T.; Sieber, S.; Morokuma, K. *J. Phys. Chem.* **1996**, *100*, 19357.
(21) Svensson, M.; Humbel, S.; Froese, R. D. J.; Matsubara, T.; Sieber, S.; Morokuma, K. *J. Phys. Chem.* **1996**, *100*, 19357.
(22) Sun, H. *J. Phys. Chem. B* **1998**, *102*, 7338.
(23) Cornell, W. D.; Cieplak, P.; Bayly, I.; Gould, I. R.; Merz, K. M.; Ferguson, D. M.; Spellmeyer, D. C.; Fox, T.; Caldwell, J. W.; Kollman, P. A. *J. Am. Chem. Soc.* **1996**, *118*, 2309.
(24) Saeys, M.; Reyniers, M.-F.; Marin, G. B.; Neurock, M. *J. Phys. Chem. B* **2002**, *106*, 7489.

(25) Morin, C.; Simon, D.; Sautet, P. *J. Phys. Chem. B* **2003**, *107*, 2995.
(26) Blaser, H. U.; Jalett, H. P.; Wiehl, J. *J. Mol. Cat.* **1991**, *68*, 215.

9. General Conclusions

The stability and adsorption geometries of a variety of small molecules were calculated using periodic DFT. The implications of these calculations for the enantioselective hydrogenation of ketones over a Pt surface is discussed here.

Hydrogen will adsorb on a Pt (111)-type surface with a slight preference for an atop adsorption site; however the preference is small and within computational error. This is in contrast to Ni and Pd surfaces where a clear preference for the hollow adsorption sites is shown. Again in contrast to Ni and Pd, subsurface adsorption is significantly disfavoured for a Pt surface. This suggests that for hydrogenation catalysis over Pt, the adsorption site of the hydrogen is not an important factor on the surface. Subsurface adsorption is not an important consideration, and the small energy differences in surface adsorption are likely to be overcome by other factors, such as interaction with the modifier or substrate in the reaction.

On a Pt (111) surface ethene is preferentially adsorbed in a di-σ configuration, with the C-C bond bridging two metal atoms, in effect creating a M-C-C-M link. Adsorption of ethene at step edges can show enhanced adsorption energy compared to a flat surface (20 kJ mol^{-1} compared to a (111) surface, for example); several proposed hydrogenation schemes involve step edges, so this enhanced stability may be a factor. The adsorption of formaldehyde onto Pt (111) (the simplest ketone-type system) adopts an adsorption geometry similar to that described above for ethene. Therefore, for more complicated systems such as acetone and methyl pyruvate which can undergo keto-enol-enolate isomerisation, it is favourable for both C=O and C=C bonds to interact with the surface, and they will preferentially adopt a di-σ type geometry if geometric constraints allow. This will be helpful for hydrogenation reactions as, if the hydrogenation proceeds via a modified Horiuti-Polyanyi scheme, this geometry is ideally set up for hydrogenation to occur. Density of states calculations for ethene and formaldehyde show that a

C=C bond interacts more strongly than a C=O bond with the metal surface, suggesting a preference for C=C rather than C=O adsorption if possible. The question at hand is hydrogenation of C=O rather than C=C; C=C hydrogenation may occur as a side reaction when isomeric forms of methyl pyruvate are present.

Calculations involving acetone show that keto-enol-enolate isomerisation will play an important role in the nature of the surface species present. The enol and enolate forms are not only stable, but are often more stable than the keto equivalent. The most stable form of acetone is calculated to be an enol form involving interaction *via* a C=C di-σ bridge. However, several stable adsorption geometries are not as favourably set-up for potential hydrogenation: the most favourable enolate structure, for example, involves two end-on type C=C and C=O interactions. As an aside, vibrational analysis of all of the structures compared with experimental data suggests that one of the experimentally observed surface structures may in fact be an enolate-type structure rather than a keto-geometry as usually suggested [1].

These calculations indicate that keto-enol-enolate isomerisation is important in the surface chemistry of acetone; however, one important question is unanswered. It is known that acetone in the gas-phase exists almost entirely in the keto-form; given this, the acetone adsorbing on the surface is likely to also be in the keto-form. Although the enol and enolate structures are energetically most favourable, the barriers to conversion between them and the keto form are as yet undetermined. If they are high, the role of enol and enolate geometries on the surface may not be as crucial as it may appear from these thermodynamic arguments at first. Development was started on a methodology to calculate reaction barriers and transition states for this type of system, involving an eigenvector following procedure. Test calculations were successfully carried out on hydrogen and formaldehyde; however it was not possible to follow up on initial calculations on acetone due to time constraints.

It was then possible to consider the adsorption of methyl pyruvate to a platinum surface. This is more complicated than the acetone case, as *cis-trans* isomerisation must now be considered as well as the keto, enol and enolate forms. It was found that the enol and enolate forms were again stable, and showed slightly more stability than the keto forms. Generally, the *cis* isomers were more stable on the surface than the *trans* isomers. This is because the *cis* isomers offer the opportunity for an extra point of contact with the surface, often adding an extra stabilising M...O interaction. The most stable structures involved anchoring the terminal C-O-C-O ester moiety to the surface, and allowing the remainder of the molecule to move away from the surface, sometimes involving a secondary M...O interaction with the other ketone group. This holds the area of interest, the C=O and C=C bonds close to the surface, where they need to be in order for hydrogenation to occur. It is possible to hypothesise that the second ketone group is available for interaction with the modifier, in the Wells-type reaction mechanism [2]. It is also possible that interaction could occur with the surface-bound atoms.

The most stable structure was a *cis*-enol involving a principle interaction of the C=C with the surface. For most structures a mixture of interactions involving C=C or C=O bonds were involved; interaction using both C=C and C=O was also possible in certain cases. The presence of C=C or C=O bonds on the surface was mostly a feature of the local adsorption geometry. For example, C=O bonds are disfavoured for enol isomers due to the protonation of the ketone group, but more favourable for enolate structures. There is currently a lack of experimental spectroscopic evidence to compare these data with; however, in the same fashion as acetone, a vibrational analysis has been performed. This will allow easy comparison between experimental and theoretical work. The same question remains unanswered as in the acetone case; although enol and enolate are more stable on the surface, what is the barrier to interconversion between isomers? It is hoped that eventually the methodology for finding transition states could be extended and applied to this system.

In a concurrent investigation, a QM/MM methodology was applied to the whole reaction system (surface, cinchona modifier and methyl pyruvate) to determine the preferred modifier/pyruvate dimer conformation. At the moment, this technique is still under development. For example, due to lack of a suitable force field for the surface, a simple sheet of graphite was used: in effect this is simply acting as a downward attraction, mimicking the pull of the surface on the adsorbates. However, this methodology was successfully applied to several cases. The interaction of methyl pyruvate with the surface and modifier was used as a test case. The results were compared with experimental data and existing theoretical calculations and a model for the interaction applied. In the best case scenario, the calculated ee was in agreement with experimental data, and an improvement on previous calculations [3].

This methodology was then applied to an unknown system; the interaction of NADPME with surface and chiral modifier (which is a system studied experimentally at Cardiff [4]) and compared with the experimental data obtained. The model was able to explain the low enantioselectivity obtained in this case in terms of the structure of the substrate. This substrate possesses a quasi-symmetry axis in the adsorbed conformation, which leads to lack of enantiodifferentiation. It is therefore possible to suggest how the ee may be improved by breaking this symmetry (for example, addition of bulky modifier groups on the substrate). Finally, the methodology was also applied to different, substituted, cinchona alkaloids to see what effect the modifier structure may have on the reaction scheme.

In addition to the extension of the QM/MM scheme, further work is currently being carried out regarding the improvement of the methodology for finding transition states. Possibilities include the use of Z-matrix descriptions of adsorbate geometry which may prove superior to the Cartesian vector-based approach here. In order to fully model the reaction system, it is necessary to include explicit hydrogen atoms adsorbed on the surface both in terms of the adsorbate geometry of the ketoester and the QM/MM scheme. Eventually, the DFT adsorption

calculations can be used to produce an accurate forcefield for the QM/MM scheme. The preferred surface geometry from the QM/MM calculations can then be used for the transition state calculations in order to determine the reaction barriers to hydrogenation.

To summarise, work has been carried out investigating the substrate-surface interaction of the enantioselective hydrogenation of ketoesters. Building up from a series of prototypical molecules, a series of calculations were performed which suggest the preferred geometry for methyl pyruvate interacting with the metal surface. Vibrational frequency analysis has provided a set of data which may be compared with future experimental work. At the same time, methodology has been under development which may help determine transition states and energy barriers for larger adsorbate-metal systems such as those considered here. A QM/MM technique is also in the early stages of development which may allow the study of the reaction system as a whole.

(1) Vannice, M. A.; Erley, W.; Ibach, H. *Surf. Sci.* **1991**, *254*, 1.
(2) Webb, G.; Wells, P. B. *Catal. Today* **1992**, *12*, 319.
(3) Bürgi, T.; Baiker, A. *J. Catal.* **2000**, *194*, 445.
(4) Coulston, N. J.; Wells, R. P. K.; Wells, P. B.; Hutchings, G. J. *Catal. Lett.* **2005**, *103*, 117.